Technological development of high-performance MALDI mass spectrometry imaging for the study of metabolic biology

by

Adam D. Feenstra

A dissertation submitted to the graduate faculty

in partial fulfillment of the requirements for the degree of

DOCTOR OF PHILOSOPHY

Major: Analytical Chemistry

Program of Study Committee:
Young Jin Lee, Major Professor
R. Sam Houk
Emily Smith
Basil Nikolau
Marna Nelson

Iowa State University

Ames, Iowa

2016

TABLE OF CONTENTS

ACKNOWLEDGMENTS. iv
ABSTRACT. vi

CHAPTER 1: INTRODUCTION. 1
  Mass Spectrometry Imaging Versus Traditional Metabolomics. 1
  MALDI-MSI Procedural Overview. 3
  Dissertation Organization. 5
  References. 6

CHAPTER 2: SPATIAL MAPPING AND PROFILING OF METABOLITE DISTRIBUTIONS DURING GERMINATION OF MAIZE SEEDS. 8
  Abstract. 8
  Introduction. 9
  Results. 12
  Discussion. 27
  Materials and Methods. 35
  Acknowledgments. 41
  References. 42
  Figures. 47
  Supplemental Figures and Tables. 56

CHAPTER 3: MULTI-MATRIX, DUAL POLARITY, TANDEM MASS SPECTROMETRY IMAGING STRATEGY APPLIED TO A GERMINATED MAIZE SEED: TOWARD MASS SPECTROMETRY IMAGING OF AN UNTARGETED METABOLOME. 74
  Abstract. 74
  Introduction. 75
  Experimental. 77
  Results and Discussion. 84
  Conclusions. 96
  Acknowledgments. 97
  References. 98
  Figures. 100
  Supplemental Figures and Tables. 108

CHAPTER 4: ORGANIC-INORGANIC BINARY MIXTURE MATRIX FOR COMPREHENSIVE LASER-DESORPTION IONIZATION MASS SPECTROMETRIC ANALYSIS AND IMAGING OF MEDIUM-SIZE MOLECULES INCLUDING PHOSPHOLIPIDS, GLYCEROLIPIDS, AND OLIGOSACCHARIDES. 118
  Abstract. 118
  Introduction. 119
  Experimental. 122
  Results and Discussion. 127
  Conclusions. 135

Acknowledgments. 137
References. 137
Figures. 139
Supplemental Figures and Tables. 146

CHAPTER 5: FIVE MICRON HIGH RESOLUTION MALDI MASS SPECTROMETRY IMAGING WITH SIMPLE INTERCHANGEABLE, MULTI-RESOLUTION OPTICAL SYSTEM. 156
Abstract. 156
Introduction. 157
Experimental. 159
Results and Discussion. 162
Conclusions. 172
Acknowledgments. 173
References. 174
Figures. 177
Supplemental Figures. 182

CHAPTER 6: SUMMARY AND FUTURE DIRECTIONS. 184
Summary. 184
Future Directions. 184
References. 187

ACKNOWLEDGMENTS

First and foremost, I would like to thank Dr. Young Jin Lee for providing me with the chance to work in his group. He not only gave me opportunities to work on challenging and interesting projects, but also motivated, taught, and sometimes forced me to become a better scientist as a whole. He gave me every opportunity and resource I needed to succeed during my time here, and for that, I am incredibly thankful. I also owe a debt of gratitude to my committee members, Drs. Sam Houk, Basil Nikolau, Emily Smith, and Marna Yandeau-Nelson for their support and input throughout my time at Iowa State.

I am also grateful for the financial support I received during my graduate studies. The work in this thesis was supported by the U.S. Department of Energy (DOE), Office of Basic Energy Sciences, Division of Chemical Sciences, Geosciences, and Biosciences at the Ames Laboratory under contract number DE-AC02-07CH11358. The Ames Laboratory is operated for the DOE by Iowa State University. The document number assigned to this thesis is IS-T 3191. I also gratefully acknowledge the support provided to me by Iowa State University.

Personally, I owe a tremendous debt of gratitude to my wife, Lindsey, for supporting me throughout my time here at Iowa State. She married me and moved to a new state just so she could put up with my long hours, frustrations, and stresses that are a part of graduate school. Throughout it all she was nothing but supportive and loving, and I will be forever thankful to her for that. Also, a special thank you to my parents Craig and Bonnie for their support and providing me with countless opportunities throughout my life, including ones that led me here.

A special thanks as well to Dr. Catherine Haustein at Central College for encouraging me to continue my education in graduate school, as well as for providing me with my first opportunity to perform analytical chemistry research.

I also owe a big thank you to my coworkers and collaborators who made everything in this thesis possible. Thanks to all Lee group members I worked with, but especially Dr. Andrew Korte, Dr. Adam Klein, Dr. Gargey Yagnik, Rebecca Hansen, Kelly O'Neill, and Maria Dueñas for their questions, answers, ideas, and feedback. Thanks as well to my collaborators Liza Alexander and Dr. Zhihong Song for their assistance in my work on maize seed germination.

Finally, thanks to all other friends and family members who supported me throughout my time here, and who I know will continue to support me from here on out.

ABSTRACT

This thesis represents efforts made in technological developments for the study of metabolic biology in plants, specifically maize, using matrix-assisted laser desorption/ionization-mass spectrometry imaging (MALDI-MSI). The first chapter gives a brief introduction on what MALDI-MSI is and how it works. The final chapter provides a summary of all works in this thesis as well as providing future directions that may be pursued based on this research.

The second chapter encompasses research performed tracking metabolite distributions between two different inbreds of maize seeds throughout the course of germination utilizing GC-MS, LC-Fluorescence, and MSI analysis. GC and LC data provide quantitative information regarding a wide range of metabolites at crude localization levels, while MSI is able to track localizations of limited metabolites in fine spatial detail. Results demonstrate that metabolites are differentially localized throughout the seed depending on inbred, metabolite class, and germination time point.

The third chapter demonstrates how MALDI-MSI can be used to acquire large, metabolomic scale datasets. Serial sections of a maize seed are coated with various matrices and analyzed in positive and negative ion mode using a multiplex imaging strategy. This strategy allows for visualization of metabolites through MSI as well as metabolite identification through the collection and analysis of high-quality MS/MS spectra.

The fourth chapter outlines the development of a binary matrix comprised of 2,5-dihydroxybenzoic acid and iron oxide (Fe_3O_4) nanoparticles. The matrix is shown to alleviate the suppression of triacylglycerol species by phosphatidylcholine, both through

standard analysis and on tissue analysis of maize seeds. The binary matrix also allows for the detection of more phospholipid classes in positive ion mode than either matrix on its own, while also demonstrating an apparent synergistic affect for large oligosaccharide type molecules.

The fifth chapter represents efforts to reduce the laser spot size for our MALDI-MSI experiments through the modification of laser optics. This work demonstrates that the swapping of the beam expander component of the optical system allows for simplistic modification of the laser spot size resulting in an easily applicable multi-resolution setup with the ability to perform imaging at a resolution of 5 μm. However, the high-resolution spot size is severely limited by depth of focus issues. This multi-resolution setup is then applied on a single maize root section at resolutions of 5, 10, and 50 μm. The images and spectral characteristics of these analyses are then compared and analyzed.

CHAPTER 1

INTRODUCTION

Mass Spectrometry Imaging Versus Traditional Metabolomics

Traditional metabolomics studies are typically performed in order to identify and quantify a wide range of chemical compounds from a given sample. In many of these types of experiments, a separation technique such as gas chromatography, liquid chromatography, or capillary electrophoresis is coupled to a mass spectrometer for detection. Mass spectrometry (MS) is an analysis technique well suited for these types of studies due to its versatility, sensitivity, label-free approach, and relative chemical non-specificity. These types of metabolomics studies have been applied to a variety of biological studies, and various approaches to these studies weighing their benefits and limitations are discussed in reviews.[1-3]

While these traditional metabolomics approaches are effective for the identification and quantification of compounds in samples, the biggest limitation of these "traditional" metabolomic studies is that they typically require either metabolite extraction from a sample or sample homogenization for introduction to the instrument for analysis.[4, 5] As a result of these tissue homogenization or metabolite extraction steps, almost all spatial localization information for metabolites analyzed in these experiments is lost. This is a significant limitation when trying to understand metabolite localization and metabolic processes in complex systems made up of highly specialized cell types that perform specific functions.

Recently, mass spectrometry imaging (MSI) has become an increasingly popular alternative tool for the analysis of tissue samples due to the fact that it combines the inherent advantages and characteristics of MS analysis with the ability to determine the spatial localization of metabolites in a sample. There are several commonly utilized approaches for MSI experiments (many reviews comparing various MSI techniques exist),[6-8] but the most commonly used method is matrix-assisted laser desorption/ionization (MALDI)-MSI.

In a typical MALDI-MSI experiment, the biological tissue of interest is first prepared and harvested at the area of interest. This tissue is then coated with a laser-absorbing medium, known as the matrix. After insertion into the instrument, a laser beam is fired on the sample at a specific location, heating and ablating the matrix molecules and tissue underneath. The desorbed ions are then focused and shuttled into the mass spectrometer for analysis. The sample is then moved a predetermined distance and the entire process is repeated. This procedure is performed across the sample with the laser being fired at a set of predefined pixels with the spectra at each location saved and correlated with specific x-y coordinates. These coordinates and spectra can then be analyzed through the use of computer software to generate heatmap images displaying spatial localizations for mass to charge values of interest. These images can then be compared or overlaid and combined with previously obtained optical images,[9] allowing for the elucidation of metabolite distributions within tissues.

While most previous applications of MSI have been for the study of metabolite distributions such as lipids in tumor analysis, drugs, and peptides,[10-12] the analysis of plant tissues by MSI is a fairly recent development.[13-15] Although the demonstrations of MSI on plant samples are somewhat limited, MSI is well suited for analysis of plant tissues due to the fact that they are made up of a variety of cell types with highly specialized functions and metabolite constituents, as demonstrated in the Kranz anatomy of maize leaves for example[16], as well as the fact that they are estimated to utilize hundreds of thousands of metabolites, many of which are unknown.[17, 18] As such, the chemical versatility and relative non-specificity of MALDI-MSI, combined with the fact that MALDI-MSI has been utilized at resolutions down to 5 μm levels for the analysis of plants,[19, 20] means that plant metabolic distributions and processes can be studied all the way down to subcellular levels.

The objective of this thesis is to demonstrate attempts made at developing technologies and approaches for the studies of metabolic biology in plants, specifically maize, using MALDI-MSI. For this work, new approaches were developed to overcome many traditional limitations of MALDI-MSI in biological analysis such as matrix-dependent analyte ionization[6], difficulties in identifying metabolites directly from tissue during an imaging run, and achievable spatial resolution. These projects include utilizing MSI to study broad aspects of maize kernel germination, expanding on previously developed methodologies[21] to gather structural information from compounds during a single imaging run, development of a new binary matrix to alleviate ion suppression and allow for the visualization of more compounds simultaneously, and instrument modifications to allow for high-spatial resolution study of plants.

MALDI-MSI: Procedural Overview

In order to further clarify the steps involved in a typical MALDI-MSI experiment for a plant tissue, a more detailed explanation is provided below. More specific procedural details for MALDI-MSI sample preparation not addressed here can be found in a previously published protocol paper.[22]

The first step in an MSI experiment for a plant is growing the tissue of interest to the desired developmental stage. Once the tissue has matured, the tissue is harvested by flash freezing in liquid nitrogen. Flash freezing quenches all active metabolism in the tissue creating a metabolite “snapshot”, which is an important step to ensure that the chemical composition and distribution of the tissue are maintained and not altered over storage time or during sample preparation. Once the tissue is frozen, it is then placed into a mold and surrounded with an embedding medium (we employ 10% w/v gelatin in water). The tissue and medium are then again flash frozen on liquid nitrogen, creating a solid, frozen block containing the tissue.

Next, the block of tissue and embedding medium is removed from the mold and sectioned to the region of interest. Tissue sections are then collected either on glass slides via thaw-mounting or on adhesive tape for storage. To prevent thawing and water soluble metabolite delocalization, sections are stored in a deep freezer until ready for use.

For sample preparation, tissue sections are first brought to room temperature under vacuum in order to prevent condensation during the warming process. Then, tissues are coated in matrix, typically either through spraying using an oscillating capillary nebulizer[23] or vapor-phase sublimation deposition.[24] Once the tissue is coated in matrix, it is inserted into the mass spectrometer and computer software is used to define the parameters of the imaging run including mass range, ion polarity, raster step size, and area to be imaged. After data collection, computer software is used to generate images displaying intensities of ions of interest within the imaged region.

Dissertation Organization

This dissertation is organized into six chapters. The first, above, provides background on mass spectrometry imaging and how it compares to traditional metabolomics experiments, as well as the steps involved in a typical MALDI-MSI experiment. Chapter 2 is a submitted manuscript that demonstrates work performed studying the metabolite dynamics and distributions of two inbreds of maize kernels during the course of germination. Chapter 3 presents a published manuscript for acquiring metabolomic level datasets using MSI through the use of serial tissue sections and multiple matrixes along with MS/MS analysis. The published manuscript in Chapter 4 details the development of a binary MALDI matrix to help with the simultaneous detection of phosphatidylcholine and triacylglycerol species in a single analysis, while also detecting more compounds and obtaining more high-quality MS/MS than either matrix individually. Chapter 5 represents work for a submitted manuscript involving improvement of laser optics for high-resolution MALDI-MSI down to the order of 5 μm as part of a multi-resolution system, and its application to the study of maize root. Finally, Chapter 6 summarizes the work in this thesis and provides future directions that could be explored based upon this research.

References

1. K. Dettmer, P. A. Aronov and B. D. Hammock, *Mass spectrometry reviews*, 2007, **26**, 51-78.
2. G. A. Theodoridis, H. G. Gika, E. J. Want and I. D. Wilson, *Analytica chimica acta*, 2012, **711**, 7-16.
3. A. Scalbert, L. Brennan, O. Fiehn, T. Hankemeier, B. S. Kristal, B. van Ommen, E. Pujos-Guillot, E. Verheij, D. Wishart and S. Wopereis, *Metabolomics*, 2009, **5**, 435-458.
4. A. Kamthan, M. Kamthan, N. Chakraborty, S. Chakraborty and A. Datta, *Protocol Exchange*, 2012.
5. R. C. De Vos, B. Schipper and R. D. Hall, *Plant Metabolomics: Methods and Protocols*, 2012, 111-128.
6. E. M. Weaver and A. B. Hummon, *Advanced drug delivery reviews*, 2013, **65**, 1039-1055.
7. L. A. McDonnell and R. Heeren, *Mass spectrometry reviews*, 2007, **26**, 606-643.
8. E. R. A. van Hove, D. F. Smith and R. M. Heeren, *Journal of chromatography A*, 2010, **1217**, 3946-3954.
9. R. Van de Plas, J. Yang, J. Spraggins and R. M. Caprioli, *Nature methods*, 2015, **12**, 366-372.
10. J. M. Wiseman, D. R. Ifa, Y. Zhu, C. B. Kissinger, N. E. Manicke, P. T. Kissinger and R. G. Cooks, *Proceedings of the National Academy of Sciences*, 2008, **105**, 18120-18125.
11. I. M. Taban, A. M. Altelaar, Y. E. van der Burgt, L. A. McDonnell, R. M. Heeren, J. Fuchser and G. Baykut, *Journal of the American Society for Mass Spectrometry*, 2007, **18**, 145-151.
12. L. S. Eberlin, I. Norton, A. L. Dill, A. J. Golby, K. L. Ligon, S. Santagata, R. G. Cooks and N. Y. Agar, *Cancer research*, 2012, **72**, 645-654.
13. Y. J. Lee, D. C. Perdian, Z. Song, E. S. Yeung and B. J. Nikolau, *The Plant Journal*, 2012, **70**, 81-95.
14. S. Kaspar, M. Peukert, A. Svatos, A. Matros and H. P. Mock, *Proteomics*, 2011, **11**, 1840-1850.
15. D. Sturtevant, Y.-J. Lee and K. D. Chapman, *Current opinion in biotechnology*, 2016, **37**, 53-60.
16. T. L. Slewinski, A. A. Anderson, C. Zhang and R. Turgeon, *Plant and Cell Physiology*, 2012, **53**, 2030-2037.
17. R. A. Dixon and D. Strack, *Phytochemistry*, 2003, **62**, 815-816.
18. R. Goodacre, S. Vaidyanathan, W. B. Dunn, G. G. Harrigan and D. B. Kell, *Trends in biotechnology*, 2004, **22**, 245-252.
19. A. R. Korte, M. D. Yandeau-Nelson, B. J. Nikolau and Y. J. Lee, *Analytical and bioanalytical chemistry*, 2015, **407**, 2301-2309.
20. D. R. Bhandari, Q. Wang, W. Friedt, B. Spengler, S. Gottwald and A. Römpp, *Analyst*, 2015, **140**, 7696-7709.
21. D. Perdian and Y. J. Lee, *Analytical chemistry*, 2010, **82**, 9393-9400.
22. A. R. Korte, G. B. Yagnik, A. D. Feenstra and Y. J. Lee, *Mass spectrometry imaging of small molecules*, 2015, 49-62.

23. Y. Chen, J. Allegood, Y. Liu, E. Wang, B. Cachón-González, T. M. Cox, A. H. Merrill and M. C. Sullards, *Analytical chemistry*, 2008, **80**, 2780-2788.
24. J. A. Hankin, R. M. Barkley and R. C. Murphy, *Journal of the American Society for Mass Spectrometry*, 2007, **18**, 1646-1652.

CHAPTER 2

SPATIAL MAPPING AND PROFILING OF METABOLITE DISTRIBUTIONS DURING GERMINATION OF MAIZE SEEDS

A paper submitted to *Plant Physiology*

Adam D. Feenstra, Liza E. Alexander, Zhihong Song, Andrew R. Korte, Marna D. Yandeau-Nelson, Basil J. Nikolau, and Young Jin Lee

Abstract

Germination is a highly complex process by which seeds begin to develop and establish themselves as viable organisms. In this paper, we utilize a combination of gas chromatography (GC)- mass spectrometry(MS), liquid chromatography (LC)-fluorescence, and mass spectrometry imaging (MSI) approaches to profile and visualize the metabolic distributions of germinating seeds from two different inbreds of maize seeds, B73 and Mo17. GC and LC analyses demonstrate that the two inbreds are highly differentiated in their metabolite profiles throughout the course of germination, especially with regard to amino acids, sugar alcohols, and small organic acids. Crude dissection of the seed followed by GC-MS analysis of polar metabolites also revealed that many compounds were highly sequestered among the various seed tissue types. To further localize compounds, matrix-assisted laser desorption/ionization MSI is utilized to visualize compounds in fine detail in their native environments over the course of germination. Most notably, the fatty acyl chain-dependent differential localization of phospholipids and TAGs was observed within the embryo and radicle, showing correlation with the heterogeneous distribution of fatty acids. Other interesting observations include unusual localization of ceramides on the endosperm/scutellum boundary, and subcellular localization of ferulate in the aleurone.

Introduction

Plants use seeds as the propagule to ensure reproduction to the next generation, and over the past 10,000 years human civilizations have established agricultural practices to ensure a seed-based food supply (Larson et al., 2014). Therefore, deciphering the processes that enable seeds to perform their biological functions is of importance in understanding how plants are propagated, and is also of practical importance to improve agriculture. Seeds are designed to survive long periods of dormancy in a relatively dry state, and the process of germination is initiated by the imbibition of water. During this germination process, many metabolic changes occur, most of which are associated with the catabolism of seed storage products (proteins, polysaccharides and lipids) into metabolically useable, simpler chemical forms that are either used as precursors to assemble the growing seedling or are oxidized via energy-producing biochemical pathways to thermodynamically support growth (Bewley, 1997, 2001).

The specific metabolic processes that support seed germination are somewhat dependent on the taxonomic clade of the plant, which determines seed tissue/organ organization and the nature of the seed storage compounds. Specifically, the seeds of the Poaceae family of monocots are characterized by a starch- and protein-filled endosperm, and their catabolism by digestive enzymes produced in the outermost layer of the endosperm (i.e. the aleurone) provides the carbon-based and nitrogenous precursors for the growth of the embryo, which is comprised of the embryonic axis and the scutellum (Dante et al., 2015). Thus, during seed germination the glycolytic and oxidative pentose phosphate pathways are induced to metabolize the hydrolyzed starch. The smaller quantities of seed storage proteins are also catabolized to provide the amino acid precursors for new protein synthesis in the embryo, or carbon-skeletons for re-assimilation into anabolic processes or further catabolized for energy generation. Finally, lipid in the form of triacylglycerol is stored in a specialized tissue (in maize, the scutellum), and its catabolism via the beta-oxidation of fatty acids can provide the elongating embryo axis an energy source. Alternatively, coupling with the glyoxylate pathway, which is induced during germination, carbon from fatty acids can be used to assemble new metabolic intermediates to support embryo-growth (Firenzuoli et al., 1968; He et al., 2015).

Thus, seed germination requires the coordinated induction of a number of processes that are non-uniformly distributed among the tissues and organs of the seed. Many of the metabolic pathways that are induced during the seed germination processes that involve starch, oil, and protein turnover have been studied via molecular, genetic, and biochemical studies (Ingle et al., 1964; Limami et al., 2002; Shu et al., 2008; Zhang et al., 2009). Therefore, techniques that allow for the determination of spatial localization of metabolites in fine detail, specifically mass spectrometry imaging (MSI), should allow for further insight into the mechanisms and actions of the pathways that are integral to seed germination.

MSI has become an increasingly powerful technique to provide spatial distribution of biological molecules within tissues (McDonnell and Heeren, 2007). In a typical MSI experiment, a sampling probe is rastered across a tissue sample with mass spectra collected at each raster point. Following data acquisition, the spatial distribution of ions of interest can be visualized based on the x-y coordinates of the collected spectra. Various sampling probes have been adopted for MSI along with accompanying ionization methods (McDonnell and Heeren, 2007; van Hove et al., 2010). Owing to its ease of use, high sensitivity, and ability to ionize a wide variety of molecules, matrix-assisted laser desorption/ionization (MALDI) has been the most widely used MSI technique. MALDI-MSI can obtain high-spatial resolution images of ions, allowing for visualization of fine structures. Spatial resolution of ~20 μm size has become routine in MALDI-MSI, and 2-5 μm spatial resolution has been demonstrated by several groups, with the latter providing a means for locating metabolites within subcellular compartments (Zavalin et al., 2013; Korte et al., 2015).

Recently, MALDI-MSI has begun to see increased application in the study of plant biology (see recent comprehensive reviews, (Kaspar et al., 2011; Lee et al., 2012)). Here, we applied MALDI-MSI in combination with GC-MS and HPLC-based analyses of extracts to study the distributions and profiles of metabolites in germinating maize seeds at four different time points after imbibition. Two contrasting maize genotypes (inbreds B73 and Mo17) were compared during germination to explore the metabolic differences arising from the genetic differences between these two inbreds. GC-MS and HPLC-based metabolite profiling of extracts prepared from the physically dissected seeds was used to distinguish between the metabolomes of the two inbreds during early germination, and provide a quantitative validation of the MSI localization data. Three different MALDI matrices were used in either positive or negative ion mode to image the spatial distribution of a wide range of metabolites. This integrated approach provides unprecedented insights into the spatially resolved coordination of metabolic processes that are sequestered among the germinating embryo axis, the lipid rich scutellum, the nutritive endosperm, the digestive aleurone, and outer pericarp cell layers during the early stages of seed germination.

Results

Overview of Experimental Workflow

A schematic of the experimental workflow is provided in Fig. 1. Maize seeds were collected from the B73 and Mo17 inbreds at four time points during the early phases of germination (0.2-h, 12-h, 24-h and 36-h post imbibition). At each time point, 9 seeds comprising three biological replicates (3 seeds each) were immediately flash frozen and extracted for whole-seed metabolite profiling. These extracts were analyzed via a GC-MS non-targeted global metabolite analysis platform, and via an LC-fluorescence based targeted analysis platform for amino acids. In addition, at the 12-h and 36-h time points, 9 seeds comprising three biological replicates (3 seeds each) were collected for GC-MS analysis of seeds dissected into component endosperm, embryo, tip-cap and pericarp. In parallel, 3 additional seeds from each of the four time points were flash frozen in liquid nitrogen and were subjected to MSI analysis. These seeds were sectioned with 10 µm thickness (25 sections per seed) and four sections (#s 5, 11, 17, 22) were inspected via optical microscopy. The three sections nearest to the most intact section as determined via optical microscopic inspection were used for MSI analysis. Microscopic analysis revealed detailed morphological features of the seed that include: the pericarp, which is the outermost layer of the seed, the aleurone layer of the endosperm, the endosperm itself, the embryonic axis, the scutellum and the tip-cap. As germination progressed, the radicle also became visible as it protruded from the embryonic axis of the embryo. It is important to note that it can be difficult to distinguish between the multicellular pericarp and the single cell aleurone layer at lower magnification. In the cases where these cell layers cannot be distinguished, we will refer to these as the aleurone and/or pericarp.

The analytes that can be characterized through MSI are often significantly limited by the choice of matrix and ion polarity. In this work, MSI analysis was performed on the three tissue sections with one of three different matrices, 1,5-diaminonaphthalene (DAN), 9-aminoacridine (9AA), and 2,5-dihyroxybenzoic acid (DHB), to cover a relatively wide range of analytes. DAN and 9AA were used in negative ion mode (*m/z* range 50-1000), while DHB was used in positive ion mode (*m/z* range 50-800, and *m/z* range 600-1600). In total, 72 seed sections were analyzed by MSI (2 inbred lines x 3 seeds per time point x 4 time points x 3 sections per seed for each of the three matrices). A spatial resolution of 100 µm was used to minimize the total data acquisition time in this large-scale experiment, while still providing sufficient spatial resolution to match the morphological features observed in the optical images.

Over the course of the analyses, hundreds of analytes were observed by both MSI and the GC- and LC-based metabolite profiling platforms. However, due to biological and analytical variation, many low abundance analytes were not reproducibly detected across all data sets. We therefore limit our discussion to the more abundant analytes that were consistently observed across three biological replicates. For simplicity of presentation of the MSI data, all the *m/z* values and mass tolerances used in producing images are summarized in Table S1, as well as color scales used to produce false color images.

Analysis of the metabolomes of germinating seeds

The non-targeted GC-MS metabolomics analyses of the whole seeds at four germination time points detected 162 analytes, of which 63 were chemically identified. These metabolites include sugars (monosaccharides and disaccharides), sugar acids, organic acids, phenolics, nitrogenous metabolites, polyols, esters, lipids, fatty acids and sterols (Table S2). There are clear differences in the metabolome between the two inbreds, and the metabolite profile is also affected by the germination process. Using the log-ratio plots, we evaluated the degree to which these differential metabolites between the inbreds are differentially affected by the germination process (Fig. 2A). In these comparisons we used the 12-hour time point as the "anchor" for all comparisons among genotypes and the seed germination time line. At this anchor time point, there are 63 metabolites that accumulate at significantly different levels between the inbreds. By comparing such log-ratio data at each of the four time points, one can gain insights of how the germination process affects the metabolome. One readily recognizable class of metabolites that are clearly distinct between the two inbreds is the amino acids, and this platform detected 10 of the proteinogenic amino acids. We therefore confirmed these differences with a second analytical platform, which specifically targeted amine-containing metabolites with LC-fluorescence, and this detected 18 of the proteinogenic amino acids (Table S3), the exceptions being proline and cysteine. In both the targeted LC-amino acid platform (log-ratio plot in Fig. S1) and the non-targeted GC-MS metabolomics platform (Fig. 2A), most amino acids are at significantly higher levels in Mo17 seeds than B73. These data are consistent with previous studies of these inbreds that identified Mo17 mature seeds having a higher amino acid content than B73 (Römisch-Margl et al., 2010). As the germination process proceeds, these differences in amino acid content between the two inbreds is reduced, so that by 36-h post-imbibition the profiles are almost identical except for Lys, Thr, and Arg that are still slightly higher in Mo17 and Trp that is now slightly higher in B73 (Fig. S1).

More broadly, 64% of the detected metabolome (i.e., 104 metabolites) accumulates to different levels between the two inbreds at least at one time-point during the germination process ($p<0.05$ in Table S2). Among the 104 metabolites that accumulate differentially among any of the time-points, 21 are differential at all time-points evaluated (Fig. 2B), and 15 are differential among any of three consecutive time-points. Seven of the first group are chemically identified and appear to be intermediates of metabolic processes that would be expected to be hyperactive during seed germination. These are specifically associated with carbohydrate metabolism (i.e., sorbitol, cellobiose, rhamnose and talose), which may be associated with starch mobilization that is occurring during the breakdown of the endosperm tissue, or possibly cell wall deposition as the new seedling tissues begin to be assembled. Eight of the chemically identified metabolites that are differential among the 3 consecutive time-points are amino acids (i.e., Asp, Glu, Thr) in the 3-early time points, and lipids (i.e., stigmasterol, sitosterol and linoleic acid) that are differential among the 3 latter time points. These profiles are consistent with seed storage protein mobilization, which occurs at the earlier stages of seed germination, and membrane deposition occurring later in the process as the seed radicle begins to grow and emerge. Finally, among these chemically identified differentially expressed metabolites are succinic acid and fumaric acid, which as intermediates of the TCA cycle and these would be associated with high rates of respiration that is needed to support the germination process (Bewley *et al.*, 2012).

Collectively these data indicate that these metabolic processes are differential between the two inbreds, which correlates with the phenotypic observation that these two inbreds germinate at different rates.

Bearing in mind that a germinating maize seed consists of different tissues, each of which express diverse metabolic processes, we evaluated the distribution of the metabolome among four distinct seed organs that are readily separable by microdissection (i.e., the pericarp and aleurone layers, the embryo, endosperm and tip-cap). The metabolomes of these microdissected organs were evaluated at 12-h and 36-h post-imbibition. Because of the wider range of metabolites that were detected, the GC-MS analysis of the metabolomes of the microdissected seed organs focused on the polar class of metabolites. These analyses revealed the relative abundances of 218 analytes, of which 75 were chemically defined (Table S4). Fig. S2 shows the log-ratio plot for the relative abundances of all analytes between Mo17 and B73, comparing the metabolomes of each dissected organ and the metabolomes of the whole seed.

An obvious advantage in the micro-dissected dataset is that it reaches lower abundance metabolites, revealing the relative abundances of an extra 56 analytes (Table S4) that were not detected when whole seeds were analyzed. More significantly, the metabolites that are the most differential between the metabolomes of the whole seed are different when one considers the metabolomes of the separated organs, which is indicative of the different metabolic processes that are being expressed in these individual organs. At both time-points, the endosperm and embryo tissues account for the majority of the differentially expressed metabolites. About half of these are shared among multiple evaluated organs, but about 20% of the metabolome is uniquely differential in either the embryo or endosperm tissues (Fig. 2C and 2D). The endosperm specific differential metabolites are primarily amino acids at 12-h post-imbibition, but by 36-h these are a mixture of amino acids, sugars and organic acids. This is consistent with the degradation of the starch and seed storage proteins that are concentrated in the endosperm of maize seeds, and indicate different rates of their catabolism between the two inbreds.

Therefore, these data indicate that as the seed germination process proceeds, the expressed metabolome changes between inbred lines with larger changes occurring in the embryo, followed by the endosperm and tip-cap. Fewer differentially expressed metabolites occur in the metabolome of the pericarp and aleurone tissues. More refined analyses of the non-uniform distribution of the metabolites in the different tissues of the germinating maize seed was obtained by MS-imaging.

Heterogeneous distribution of the mobilization of seed storage reserves

In the grasses, energy in dormant seeds is predominantly stored as polysaccharide starch granules within the endosperm, which can be mobilized by hydrolytic enzymes (e.g. a- and b-amylases) released by the aleurone and scutellum of germinating seeds (Zeeman et al., 2007). The images in Figure 3A show large hexose polysaccharides (Hex_{5-9}), presumably degraded from starch, observed at low abundance levels and localized in the endosperm. Disaccharides, predominantly sucrose, are also observed and are present at much higher levels and primarily constrained to the germinating embryo. At the later stages of germination, the disaccharide signal appears to be concentrated more extensively in the emerging radicle of the embryonic axis. Disaccharide is also detected within other tissues such as the endosperm and pericarp and/or aleurone, but at lower abundance.

These non-homogeneous distributions of the polysaccharides are conserved in both B73 and Mo17 inbreds, and are consistent with the mobilization of sucrose within the scutellum and transport to the embryonic axis, specifically the radicle (Sánchez-Linares et al., 2012).

Seed oil energy reserves in maize are localized to the embryo, which is in contrast to other cereal grains (e.g. wheat and oat) that store oil in the endosperm (Leonova et al., 2010). Embryonic localization of four TAG species differing in fatty acyl chain composition is shown in Fig. 3B. At the initial stages of germination (i.e. 0.2 and 12-h), TAGs are homogeneously distributed throughout the embryo, including the embryonic axis and the scutellum. As germination progresses and the radicle of the embryonic axis begins to elongate, TAGs begin to display non-uniform localization patterns, similar to fatty acid and phospholipid molecular species, as will be discussed later.

During the germination process, amino acids become available from the breakdown of storage proteins initiated by the hydrolytic activity of protease enzymes synthesized in the protein storage vacuoles (PSV). The reduced nitrogen associated with these amino acids can be used for additional *de novo* synthesis of amino acids (Bewley et al., 2012). Because of their low ionization efficiency and amphiprotic nature, amino acids are difficult to analyze by MALDI-MS (Toue et al., 2014). Despite this known difficulty, three amino acids were reliably detected in the MSI experiments, these being lysine, arginine, and proline (Fig. 3C). Lysine and arginine are barely detectable in B73 seeds, but are clearly visible in Mo17 seeds. This striking difference in the abundance of lysine and arginine between the two inbreds is consistent with the parallel profiling data of these amino acids generated by LC-fluorescence analysis of o-phthaldialdehyde (OPA)-derivatives conducted on extracts of seeds (Fig. S1); the concentrations of these amino acids are significantly lower in extracts of B73 seeds than Mo17 seeds throughout the germination process. The LC method could not analyze proline levels in these extracts because the OPA-derivatization requires a primary amine group. Rather, proline concentrations were compared from parallel GC-MS analyses of the polar extracts of seeds (Fig. 2A and S2). These data are in agreement with the MALDI-MSI data, with proline levels being similar or slightly higher in B73 seeds than Mo17 seeds. The MSI-data establish that the accumulation of these amino acids (lysine, arginine and proline) is concentrated in the embryonic axis and the scutellum of the seed embryo. Moreover, in later time-points, proline is more prominent in the radicle of the seed, but lysine and arginine appear to be less abundant in the radicle. These MSI-based visualizations of the *in situ* localization of these amino acids are consistent with the direct quantitative measurement of the levels of these amino acids in extracts of micro-dissected embryo tissues of the maize seeds (Fig. S3).

Metabolites enriched in pericarp/aleurone layers

The pericarp and aleurone layers of the seed are responsible for the protection of the mature seed, as well as the initial uptake of water that begins germination. As germination begins in maize, many of the enzymes needed to break down storage molecules in the seed are released from the aleurone layer of the endosperm (Chrispeels and Varner, 1967; Fincher, 1989; Bernier and Ballance, 1993). In this work, three metabolites are found to be uniquely located at the perimeter of the cross-section and therefore can be surmised to be located either in the pericarp (outermost layer of the kernel) or the aleurone layer, which is the outermost single-cell layer of the endosperm. The three metabolites remained localized to this region of the seed throughout the germination process, and were not detected in the embryo or the endosperm (Fig. 4A). This is in contrast to most other metabolites, such as sucrose (Fig. 3A) or citrate (Fig. 5), that are found in the aleurone and/or pericarp, but also in other tissues. One of these metabolites (*m/z* 193.051) was identified as ferulate by accurate mass (< 5ppm) and MS/MS (Fig. S4). However, useful MS/MS spectra could not be obtained for the other two ions (*m/z* 135.046 and *m/z* 161.025) because of their low abundance. The chemical compositions calculated from the accurate masses, $C_8H_8O_2$ and $C_9H_6O_3$, respectively, suggest they may have one aromatic ring.

The spatial resolution used in this experiment, 100 μm, was not sufficient to determine whether these metabolites are specifically localized to the multiple cell layers of the pericarp or the single-cell layer of the aleurone. To further explore the exact location of these compounds, a high-resolution MSI experiment was performed with 10 μm spatial resolution on a small region of the outer perimeter of B73 maize seeds at 24-h post-imbibition (Fig. 4B, 4C). Because of the limited sensitivity inherent with a much smaller sampling area, only ferulate provided sufficient ion signal to produce a clear image. The ferulate image was compared with that of the phospholipid phosphatidylinositol (PI) 34:2 and malate to better understand the relative localization of these compounds. Comparing these molecular images with the corresponding optical image (Fig. 4B) and overlaying MS images with the optical image (Fig. 4C), ferulate (red) appears to be present exclusively in the aleurone layer, particularly at the boundary between the aluerone and the pericarp, while the phospholipid PI 34:2 (green) is present throughout the aleurone layer, and malate (blue) is localized in the endosperm and the pericarp layer of the seeds.

Localizations of Respiratory Intermediates - Phosphorylated Metabolites and Organic Acids

During the process of seed germination, respiration of seed reserves enables energy generation in the absence of photosynthesis, supporting the development of the seedling until it protrudes from the soil and is able to harness solar energy via photosynthesis. Respiration initiates within minutes of imbibition by the activation of cytosolic enzymes for glycolysis, the oxidative pentose phosphate pathway, and enzymes for the TCA cycle in mitochondria (Bewley et al., 2012). The distributions of two phosphorylated intermediates of respiration, hexose phosphate and glycerol phosphate, and one or possibly two organic acids of the TCA cycle, citrate and/or isocitrate, are shown in Fig. 5. The phosphorylated metabolites are most likely glucose-6-phosphate and glycerol-3-phosphate, respectively, but we cannot distinguish among the possible regio- or stereoisomers by MALDI-MS or MS/MS experiments. Similarly, we are also unable to distinguish between citrate and isocitrate, and the resulting image is likely an integration of the distribution of these two metabolites.

In both inbreds, hexose phosphate and glycerol phosphate are localized in the germinating embryo and the aleurone and/or pericarp of the seeds, and this location is unaltered throughout the germination process. Hexose phosphate appears to be slightly less abundant in the radicle, whereas glycerol phosphate is more homogeneously distributed throughout the embyro. The organic acids, citrate/isocitrate, are observed first at 0.2-h post-imbibition, and they are predominantly concentrated in the perimeter (i.e. the aluerone and/or pericarp) of the seed. As germination progresses, citrate/isocitrate also occurs within the radicles and scutella of both inbreds, similar to the hexose phosphate and glycerol phosphate compounds; the former is probably associated with the induction of the glyoxylate pathway or TCA cycle, which is induced during germination to convert lipid-derived carbon to sugars via acetyl-CoA intermediate, while the latter two are an intermediate and side product of glycolysis, respectively (Bewley et al., 2012).

Malate is another molecule involved in the TCA cycle and is detected in all replicates at all time points. Unlike citrate, its localization is found only in the endosperm of the seed and radicle of some more fully developed seeds (Fig. S5A). This is not compatible with GC-MS analysis of the micro-dissected seed samples that indicated most of the malic acid is present in the embryo of the seed rather than the endosperm (Fig. S5C). In contrast, citrate is much more abundant in embryos (Fig. 5) matching well with the dissected GC-MS data (Fig. S5D). According to our previous experience on MSI of leaf tissues, malate signals and images are often irreproducible unless the tissues are prepared fresh and analyzed as soon as possible. Hence, we suspect this observation may be an artifact coming from the degradation of malate during tissue storage. To confirm this hypothesis, a separate MSI experiment was conducted on a seed that was analyzed on the same day it was collected. In this experiment, we found the majority of the malic acid in the embryo as expected (Fig. S5B).

Differential distributions of lipid classes accentuated in the emerging radicle

In monocotyledons (i.e. monocots) such as maize, the embryonic axis develops into two main parts: the radicle, which is the primary root and is protected by the coleorhiza, and the plumule, or collection of leaf primordial, which is protected by the coleoptile. The germination process transitions into seedling growth with the protrusion of the radicle from the embryo. These anatomical structures develop with significant cell extension with or without cell division. Radicle growth through cell extension is a turgor-driven process that will involve the assembly of new membranes, requiring lipid biosynthesis (Bewley, 1997, 2001). We therefore applied MALDI-MSI to localize lipids during the germination process. MALDI-MS efficiencies are dramatically different for each lipid class, depending on their chemical functionalities. Three matrices were used in positive and negative ion modes to visualize different classes of lipids. DHB was used in positive ion mode for phosphatidylcholine (PC) and ceramides; 9AA was used in negative ion mode for fatty acids; and DAN was used in negative ion mode for phosphatidylethanolamine (PE), phosphatidic acid (PA) and phosphatidylinositol (PI).

Fig. 6 compares the spatial distribution of four fatty acids, palmitate (16:0), stearate (18:0), oleate (18:1), and linoleate (18:2) between the two inbreds at four germination stages. Over the course of the germination process, palmitate and linoleate occur homogeneously throughout the embryo in both inbreds. In contrast, stearate is partially and oleate is almost completely absent from the radicles of both inbreds. This unprecedented finding is similar to the localization of TAGs (Fig. 3), and phospholipid classes (Fig. 7). However, it is in contrast to the GC-MS metabolomics data, which do not provide any spatial localization information for these fatty acids between the genotypes or changes associated with germination time points (Fig. S6), and do not offer any indication of this unique, non-uniform localization of oleate.

The spatial localization of four different classes of phospholipids (PE, PA, PI and PC) was compared in germinating seeds at 36-h post-imbibition (Fig. 7A). These analyses also evaluated the distribution of different phospholipid molecular species arising from different combinations of fatty acyl chains. As may be expected from the fact that new cells are being generated as the embryo is undergoing expansion (in contrast to the endosperm, which is being consumed), all four phospholipids are most highly abundant in the embryo. There are contrasting localization patterns depending on the phospholipid class and on the molecular species of the phospholipids. With all four phospholipids and in both inbreds, the phospholipids with the most unsaturated acyl chains (36:4) show an even distribution between the radicle and the other embryonic tissues. For PI, PC, and PA, the more saturated phospholipids (i.e., in the order of 36:3, 36:2, and 36:1) are less concentrated in the radicle as compared to other embryonic tissues. In contrast, PE shows a unique localization pattern, with molecules of an even number of double bonds (36:4, 36:2) being homogeneously distributed over the entire embryo, including the radicle, but PEs with an odd-number of double bonds (36:3, 36:1) being less abundant in the developing radicle. These differential localization patterns were also observed at all time points during the germination process (Fig. S7).

To further investigate the non-uniform distribution of phospholipids, quantitative comparison was made from two mass spectra averaged over selected pixels from the radicle and scutellum of seeds developed with a radicle. Fig. 7B shows the ratio of each lipid molecular species, comparing signal strength for pixels in the radicle to the signal strength for pixels in the scutellum. This analysis confirms the visual patterns observed from the MS images; namely, the signal strength for the more saturated PA, PI, and PC is lower in the radicle region, whereas the signal strength of PE is lower only for those species with an odd number of double-bonds. The unique localization of PE compared to the other phospholipid molecular species may be related to the unusually high abundance of PE 36:2.

Fig. 7C illustrates these abundance differences among the phospholipids in the radicle region. Whereas the most abundant molecular species are 36:4 for PC, PA and PI and the more saturated forms of these phospholipids occur at lower levels, 36:2 is the most abundant PE, followed by PE 36:4. With the exception of PE 36:2, which is slightly, but statistically higher in Mo17 than in B73 (p~0.01) and accordingly lower abundance of PE 36:4 (p~0.03), there are no other significant differences between the genotypes.

The differential localization of phospholipids between the radicle and scutellum of the embryo is consistent with the relatively lower abundance of oleate (18:1) in the radicle (Fig. 6). To investigate this possible correlation, we took advantage of the MS/MS capabilities of the MALDI-MS instrument used in this study and performed MS/MS imaging experiments. In MS/MS, a specific precursor ion can be selected and fragmented, and the mass spectra of fragment ions can be interpreted to extract structural information of the precursor ions. In the current MS/MS imaging experiment, a four-step data acquisition pattern (Fig. S8) was used to selectively acquire the MS/MS data for four PA and PE molecular species (PE 36:3, PE 36:2, PA 36:3 and PA 36:2). Fig. 8A shows MS/MS spectra obtained from the MS/MS imaging experiment for PA 36:2 and PE 36:2 in the radicle region of a 24-hr Mo17 seed (similar results were seen for B73). For these 36:2 lipid species, there are two fatty acyl chain combinations possible: 18:2/18:0 and 18:1/18:1. The MS/MS spectrum of PA 36:2 has each of the three fatty acyl fragments (18:2, 18:1, and 18:0), indicating the presence of both the 18:2/18:0 and 18:1/18:1 combinations. In contrast, MS/MS of PE 36:2 shows only the 18:2 acyl fragment in the radicle of Mo17, indicating it is primarily comprised of the 18:2/18:0 combination. Because MS/MS preferentially induces fragmentation at the sn-2 position for PE and PA species (Hou et al., 2011), the inability to observe the 18:0 acyl fragment could indicate that PE 36:2 has the 18:2 fatty acyl chain predominantly located at the sn-2 position. Parallel MS/MS experiments of PA 36:3 and PE 36:3 reveals the occurrence of both 18:2 and 18:1 acyl fragments, confirming the occurrence of these two fatty acyl chains in these lipids (Fig. S9).

Relative quantification between 18:2/18:0 and 18:1/18:1 was performed from this dataset for PA and PE species in the radicle and scutellum, as shown in Fig. 8B. Similar to Fig. 7B and 7C, in this calculation MS/MS spectra were averaged from pixels in the radicle and the scutellum, and fatty acyl fragments were summed to calculate the proportion of each molecular species. It should be noted, however, that because of the difference in the fragmentation efficiency between sn-2 and sn-1 positions this is not an exact quantification of the four lipids. Regardless, these calculations indicate that PE 36:2 (18:2/18:0) is the predominant PE species both in the radicle and scutellum, matching the homogeneous images of the distribution of PE 36:2 (Fig. 7A), and of linoleate (Fig. 6) throughout the embryo. In contrast, PA 36:2 (18:1/18:1) occurs at significantly higher levels in the scutellum than in the radicle, consistent with the heterogeneous distribution of oleate among these two tissue types (Fig. 6).

Several ceramide (Cer) molecular species were also observed in both inbreds, and their accumulation is persistent throughout the course of germination. Fig. 9A shows the distribution of Cer d42:1 and Cer t42:0, and the distributions of other Cer species (Cer d42:2, d40:1, t40:0) are shown in Fig. S10. We have previously performed MS/MS of Cer d42:1 in germinated B73 maize seed confirming its structure (Feenstra et al., 2015), and we are also confident of the assignment of other ceramides based on the accurate mass determinations of the ions, all within 5 ppm mass error; however, MS/MS was not successful for other ceramides due to their low abundances. All ceramides have unique localization patterns that are different from the other lipid classes that were imaged. In both inbreds, and throughout the course of germination, all the detected ceramides are located on the endosperm side of the endosperm-scutellum boundary. Fig. 9B shows this contrasting localization, comparing the distribution of Cer d42:1 with the embryo-specific PC 34:2, relative to the endosperm-scutellum boundary.

Discussion

The process of seed germination is a particularly interesting biological process driven by cellular and metabolic coordination among several spatially distinct compartments to successfully establish the seedling. Because of the agricultural importance of cereal grains, previous metabolomics-based work has focused on these processes during the germination of rice (Shu et al., 2008) and the malting process for barley (Frank et al., 2011). However, traditional metabolomics analyses often prove laborious and challenging, with limited spatial information. Conversely, MSI presents a straightforward analytical capability that provides high-resolution spatial distribution data for small metabolites (< 1.5 kDa) but at the cost of limited quantitative information and total number of metabolites detected. In this work, a combination of GC- and LC-based metabolomics analyses were combined with an MALDI-MSI approach to study the quantitative metabolite profile data and spatial distribution of metabolites during the germination of seeds of two maize inbreds, Mo17 and B73. These complementary strategies provided a path to investigate both genotypic and developmental differences that occur during germination, as well as provide quantitative and finely-detailed spatial localization of metabolites.

The genetic diversity within maize is vast, as recently evidenced by rampant structural variation in genic content and copy number variation across maize inbreds (Springer et al., 2009; Lai et al., 2010; Swanson-Wagner et al., 2010; Hirsch et al., 2014). Inbreds B73 and Mo17 were selected in state-sponsored public breeding programs led by Land Grant institutions Iowa State University and University of Missouri, respectively in the early 1900s continuing to today. B73 is derived from the Stiff Stalk Synthetic population generated and maintained at Iowa State University and Mo17 was selected from Lancaster Sure Crop material first developed in Lancaster, PA (Troyer, 2004). The B73 and Mo17 inbreds share a rich history in the public sector as key founders of U.S. germplasm (Lu and Bernardo, 2001) and development of agronomically important hybrids, both in the public and private sectors (Troyer, 2009). These important inbreds differ significantly in their genomic structures, both in terms of presence-absence variation in gene content as well as in the prevalence of single nucleotide polymorphisms, occurring on average every ~80 bp (Fu et al., 2006; Vroh Bi et al., 2006) based on comparison of published genome sequence (Schnable et al., 2009). The genetic diversity between B73 and Mo17 translates into metabolic, physiological and phenotypic differences, including differences in germination rates and germination efficiency for inbreds B73 and Mo17 that have been observed under different environmental conditions (Munamava et al., 2004). This genetic diversity between the two inbreds has also led to differences in the metabolome, as was observed in our metabolic assessment of early germination of maize seedlings. The most significant metabolic difference between germinating B73 and Mo17 seeds was in the enhanced accumulation of free amino acids in Mo17.

The fact that four of the amino acids (i.e. Arg, Asn, Gln, Lys) showing higher abundance in Mo17 vs. B73 are the carriers of reduced nitrogen may indicate that these metabolic processes are of significance in the interaction between carbon and nitrogen metabolism, as the germinating seeds adjust the physiological needs of the emerging seedling from different starting points in the amino acid profiles available in each inbred. Consistent with this hypothesis is the fact that these amino acid profiles are differentially affected by the germination processes, with threonine, lysine, arginine and asparagine occurring at higher levels in Mo17 than B73 at the earlier stages of germination (12-h and 24-h post-imbibition), and glutamine levels also increasing in abundance in Mo17 at early stages and in B73 by 36-h post-imbibition. Germination efficiency has been shown to be correlated to differential expression of enzymes involved in aspartate-derived metabolism and, in turn, differential metabolism of specific amino acids (Anzala et al., 2006) as well as nitrogen-derived amino acid metabolism, specifically related to an amino acid-anabolism enzyme, glutamine synthetase (Limami et al., 2002). Moreover, quantitative genetic approaches utilizing B73xMo17 derived germplasm to dissect the genetic basis for germination phenotypes have identified candidate genes involved in amino acid metabolism (Kollipara et al., 2002).

A second clear metabolome difference between the two inbreds is in the preferential accumulation of small organic acids in B73 (i.e. malate, pyruvate, fumarate) as compared to Mo17. Interestingly, quantitative genetic analyses of recombinant inbred populations derived from B73 and Mo17 parental inbreds have identified quantitative trait loci associated with germination under both optimal and low temperature conditions. Although numerous candidate genes were identified (> 3000), one encodes a malate dehydrogenase (Hu et al., 2016). Collectively, the observed differences in metabolite accumulation between Mo17 and B73 across early germination provide testable hypotheses regarding their impacts on differential germination efficiency and other germination-related traits that have been shown to differ across maize inbreds.

Chromatography-based metabolite profiling generated quantitative data of small molecules, such as sugar monomers, organic acids, amines and amino acids, fatty acids, and sterols, which establish that germinating seeds of the two maize inbreds are readily distinguishable at the level of the expressed metabolome (Fig. 2). While these analyses provided global profiles of the seed metabolomes from which one can generate statistical quantitative correlations among individual metabolite abundances as affected by development and genotype, detailed information on the localization of the metabolites at the cellular level was lost. Further such analyses of seeds micro-dissected to separate different seed organs provided compartmentalization information of the metabolites, and demonstrated that the metabolome of these different organs vary with respect to the developmental program of germination, and is further differentially affected by different genotypes (Fig. 2C and 2D). In general, however, even with the micro-dissected organs, the localization of the metabolites is limited to large, physically separable structures, each of which are made up of a combination of different tissue types with differing metabolic capabilities. Cell-type specific analysis can be done by sorting cells or using laser capture microdissection, but such analysis is not typically applicable for metabolomic profiling because of the potential metabolite turnover during the laborious sample preparation process. Furthermore, the unknown degree to which these physically separated organs may be cross-contaminated complicates the interpretation of these data. MSI, therefore, offers a convenient means of overcoming the limitations of the chromatography-based metabolite profiling techniques in generating spatially resolved data, with fine-scale localization information in maize seeds at the cellular level.

Combining MALDI-MSI data with chromatography-based analyses allows for more comprehensive coverage of the metabolome beyond that obtainable by either one individually. For example, GC-MS revealed the relative abundance of small sugar molecules (tetroses, pentoses, hexoses and disaccharide), and analysis of micro-dissected seed organs indicated that these small sugars are primarily localized to the embryo as compared to the endosperm, and they also occur in the pericarp and/or aleurone tissues. MSI was only able to visualize the disaccharide species, and that data is in agreement with the distribution determined from the chromatographic analysis of micro-dissected organs. However, MSI provided additional information by successfully visualizing the location of large polysaccharides (Hex_5 to Hex_9), all of which are localized to the starchy endosperm of the seed (Fig. 3A). These results are consistent with the expectation that starch breakdown during germination occurs initially by the action of α- and β-amylase secreted from the scutellum and aleurone. These oligosaccharides are broken down to their constituent glucose units and are transported to and taken up by the scutellum, where they are reassembled into sucrose, the disaccharide likely visualized by MSI (Bewley, 2001; Nonogaki, 2008). The localization of the presumable sucrose disaccharide in the emerging radicle is consistent with the previously reported mobilization of sucrose within the scutellum and subsequent transport to the embryonic axis, specifically to fuel cell elongation in the radicle (Sánchez-Linares et al., 2012).

A similar benefit of combining metabolomic and MSI data is observed when one considers the patterns observed for the different fatty acids and lipid molecular species. GC-MS analysis was limited to being able to detect fatty acids primarily of 16 and 18-carbon chain lengths after derivatization to volatile methyl-esters. In contrast, MALDI-MSI can not only detect these fatty acids without derivatization, but also detect larger non-volatile lipid molecules such as phospholipids, ceramides, and triacylglycerols. Both MSI and GC-MS showed similar fatty acid profiles with minor differences in their relative abundances between the two inbreds. However, MSI revealed differential localization of the fatty acids dependent on the degrees of unsaturation. Homogeneous distributions were observed within the embryo for palmitate and linoleate, but absences were seen in radicles for oleate and partially for stearate (Fig. 6).

Similar differential patterns of spatial distribution were observed for phospholipids and TAGs depending on their fatty acyl species, in that oleate contributes to the absence in radicles and linoleate contributes to the homogeneous embryonic distributions. For example, fully unsaturated TAG 54:6 (18:2/18:2/18:2) is highly homogeneous throughout the embryo, but becomes absent in the radicle as the degree of saturation increases (Fig. 3B). Phospholipids of PI, PA, and PC show the same trend as TAGs for their absence in the radicle being correlated with the degree of saturation (Fig. 7). PE shows apparently different localization from other phospholipids by having PE molecular species with even-number of unsaturation (36:4, 36:2) evenly distributed throughout the radicle and embryo. However, MS/MS experiments revealed that this is due to the high radicle content of

18:1/18:1 in other 36:2 phospholipids, while PE 36:2 is mostly composed of 18:2/18:0 (Fig. 8B). These results suggest that the heterogeneous distribution of fatty acids dictates the fatty acyl chain dependent differential localization of lipids. Such non-uniform distribution has previously been observed in cotton (Horn et al., 2012) and *Camelina* seeds (Horn et al., 2013); thus, this is not unique to maize, but apparently a more general phenomenon. However, the specifics of the distribution are unique for each species, likely owing to the different anatomy and biological properties of these seeds.

Because plant systems use PC as the substrate for fatty acid desaturation, specifically the FAD2 enzyme that generates 18:2 (Bates et al., 2013; Samuels et al., 2013), it is tempting to speculate that this non-uniform distribution of the unsaturated phospholipids may reflect the distribution of this biosynthetic enzyme. Consistent with this hypothesis, differential distribution of FAD2 enzyme occurs in germinating safflower seedlings. Four *fad2* genes within the product-diverse 11-member safflower FAD2 family were found to express specifically in the hypocotyl and cotyledons of germinating seedlings (Cao et al., 2013). Alternatively, the non-uniform distribution of these phospholipids may reflect the chemo-physical properties of the phospholipids, which guides their distribution. Therefore, these data lead to testable hypotheses for future experiments. For example, comparing the cellular distribution of the FAD2 enzyme with respect to the 18:2-containing phospholipids would directly test the first hypothesis, and could eliminate the more complex second hypothesis.

Ceramide molecular species detected by MSI showed incredibly unique localizations that were significantly different from any other lipid species detected in this work. By directly comparing to PC molecular species, we found that the ceramides are localized to the endosperm side of the endosperm/scutellum boundary. Previous work has reported the presence of ceramides in maize (Dietrich et al., 2005), as well as in the bran and endosperm of rice grains (Fujino et al., 1985), supporting our observed localization of ceramides in the endosperm of the maize seeds. Although detailed biochemical understanding of the biological functions that ceramides play in plants is relatively poor in comparison to mammalian and fungal organisms (Kolesnick, 2002; Levy and Futerman, 2010), they are thought to be important for plant growth and defense. Inhibition of their biosynthesis by a mycotoxin (Williams et al., 2007) or mutations in the biosynthesis pathway leads to programmed cell death and disease states in plants (Lynch and Dunn, 2004; Markham et al., 2013), whereas induction of their biosynthesis via overexpression of ceramide synthases leads to impacts in biomass accumulation, growth and mycotoxin resistance (Luttgeharm et al., 2015).

In conclusion, this study successfully demonstrated the combined use of chromatography-based metabolite profiling and MALDI-MS based chemical imaging to elucidate the metabolite profile and spatial distribution of metabolites in the complex processes of seed germination in maize. The traditional metabolomics approaches offered comprehensive metabolite coverage of small molecules, which demonstrated that there are significant differences in the metabolite profiles between inbreds during germination, as well as between different seed organ/tissue types of the same inbred. Conversely, MALDI-MSI offers more detailed spatial information on the distribution of the metabolites, especially in terms of unusual localizations of lipids. This study demonstrates the synergy that can be gained by combining these strategies to reveal new insights into complex biological processes that integrate capabilities of different cellular compartments.

Materials and Methods

Seed germination and harvest

Seeds of maize (*Zea mays* L.) inbreds B73 and Mo17 were imbibed and germinated similar to previously described (Liu et al., 2013). Briefly, seeds were placed in deionized water and imbibed while shaking at 300 rpm for 10 minutes. These seeds were then placed embryo side down on moist filter paper in Petri dishes. Plates were incubated in a greenhouse under a diurnal cycle of 15 h light and 9 h dark at 27° C and 24° C, respectively.

Germinating seeds were collected at four time points, 0.2-h, 12-h, 24-h, and 36-h, with the 0.2-h time point corresponding to those taken immediately after 10 minutes of imbibition. At each time point, seeds were collected that appeared similar in terms of their developmental stage. Three seeds chosen for MSI were sectioned longitudinally, and immediately flash frozen in liquid nitrogen and stored at -80° C. From another batch of seeds grown in identical conditions, nine seeds were chosen at each time point for total metabolite and amino acid analysis. Whole seeds were frozen in liquid nitrogen and dried using a vacuum lyophilizer (Labconco Corp., Kansas City, MO); then, three seeds were combined as one biological replicate and pulverized using a Mixer Mill 301(Retsch GmbH, Germany) in 2 ml Eppendorf tubes for total metabolites analysis. A companion set of germinating seeds of similar shapes were collected at the 12-h and 36-h time points, micro-dissected to separate the pericarp and/or aleurone (these two layers could not be separated), tip-cap, embryo and endosperm, and then followed the same lyophilization/pulverization process above for each dissected tissue.

Cryosectioning

Each seed was removed from -80° C storage and quickly placed cut-side down into a plastic cryo-mold (Electron Microscopy Sciences, Hatfield, PA, USA). A warm, 10% w/v gelatin solution was poured into the cryo-mold such that the solution completely covered the seed. The mold was then held over liquid nitrogen until the gelatin became mostly opaque (~1/2 of the gelatin) and then transferred to a -20° C freezer to complete the freezing process.

The frozen gelatin block was then removed from the cryo-mold and mounted on a cryostat chuck. The seed was then cut down to the tissue region of interest (for example, the embryo axis containing the radicle, if the radicle was present in the seed) using a Leica CM1520 cryostat (Leica Biosystems, Buffalo Grove, IL, USA) until the embryonic tissue was visible, following which consecutive 10 μm tissue sections were collected on adhesive tape windows (Leica Biosystems) to preserve structural integrity of the tissue sections. The adhesive windows were then taped face-up onto chilled glass slides and stored at -80° C. A total of 25 sections were taken from each seed and a subset were subjected to either microscopic imaging or MSI analysis.

Microscopy and MALDI imaging preparation

Microscope images of four sections (numbers 5, 11, 17, and 22 of the 25 collected) were obtained using an Olympus SAH-10 stereo-microscope (Olympus Scientific Solutions, Waltham, MA) with an AxioCam HRC and Axio Vision software (Carl Zeiss Inc., Thornwood, NY) to provide finely detailed images. From these images, the highest-quality section was selected based on the clear visualization of developmental stage and section integrity. The sections nearest to this section were chosen for mass spectrometry imaging. The sections selected for MSI were placed on a chilled aluminum plate and then allowed to slowly equilibrate to room temperature under vacuum, preventing condensation and water-soluble metabolite delocalization.

Matrix application was performed via sublimation-vapor deposition as previously described (Hankin et al., 2007). Briefly, the sample was attached to the bottom of the sublimation flask condenser, 300 mg of matrix was added to the bottom of the flask, and the flask was sealed and evacuated to ~20 mtorr. The condenser was cooled with a dry ice/acetone slurry. After cooling the condenser, the flask was placed into a pre-heated heating mantle and maintained at a constant temperature (140° C for DAN and DHB, 170° C for 9-AA) for 3-6 minutes until matrix deposition was visible on the tissue surface. After matrix application, tape windows were transferred to a MALDI plate and inserted into the mass spectrometer for MS imaging.

MALDI-MS Imaging

MS imaging data was acquired using a MALDI-linear ion trap (LIT)-Orbitrap mass spectrometer (MALDI-LTQ-Orbitrap Discovery; Thermo Finnigan, San Jose, CA) modified to use an external diode-laser pumped frequency-tripled Nd:YAG laser (355 nm, Elforlight, UVFQ series). For DAN and 9AA in negative ion mode, Orbitrap MS data were acquired using a 100 μm raster size for the *m/z* range of 50-1000. For DHB in positive ion mode, each raster step (100 μm) is broken down into two spiral steps (50 μm each), and Orbitrap MS scans were performed for *m/z* 50-800 and *m/z* 600-1600, respectively. For all imaging runs, the laser spot size was ~40 μm estimated from the burn mark on thin DHB film, except the high-spatial resolution experiment in Figure 5 where the laser spot size was ~10 μm adjusted using a beam expander in the optical beam path. Laser pulse energy and number of shots were optimized for each matrix.

Data analysis and image generation were performed using ImageQuest and Xcalibur software (Thermo). Image normalization was performed for some images and is noted in the figure caption. Mass values and tolerances used to generate images are summarized in Supplementary Table 1. For some metabolites, MS images were generated after normalization to the total ion count (TIC) at each pixel (defined by the raster step) to minimize spot-to-spot variation, and the same color scale is used regardless of genotype or germination time point. For most of the metabolites, however, MS images are produced in absolute ion scales without normalization due to the fact that normalization can distort the images for low abundance ions, and the color scheme was arbitrarily adjusted for each image to obtain an image with the highest contrast to display where the metabolite is localized without accentuating background noise.

Separate MS/MS experiments were performed using collision-induced dissociation of the linear ion trap. For m/z 193.051, a collision energy of 100.0 was used with an activation time of 30 ms and an isolation mass window of 0.8 Da. For phospholipid MS/MS, a collision energy of 45.0 was used with an activation time of 30 ms and isolation mass window of 1.0 Da.

Total Metabolites Analysis

Total metabolite extractions were carried out as described previously (Schmidt et al., 2011). Extracts were prepared from ~20 mg of lyophilized and pulverized whole seeds and dissected seed fractions. Each sample was spiked with two internal standards (25 μg of ribitol and 25 μg nonadecanoic acid for polar and non-polar fractions, respectively) and 0.35 ml of hot methanol (60° C) was added and incubated at the same temperature for 10 min, followed by sonication for 10 min at full power. To this slurry, 0.35 ml of chloroform and 0.3 ml of water were added and the mixture was vortexed for 1-3 min. After centrifugation for 5 min at 13,000xg, 200 μl of the upper phase (polar fraction) and 200 μl of the lower phase (non-polar fraction) were separately removed into 2 ml GC-MS vials, and dried in a Speed-Vac concentrator (model SVC 100H, Savant, NY). Both polar and non-polar extracts were analyzed for whole seed samples, and only the polar fractions were analyzed for micro-dissected samples.

Double derivatization via methoximation and silyation was performed to protect ketone functional groups and to increase the volatility of the compounds, respectively. For methoximation, 50 μl of 20 mg/mL methoxyamine hydrochloride dissolved in dry pyridine was added, and the reaction was conducted at 30° C for 1.5 hours with continuous shaking. Silylation was performed by the addition of 70 μL of *N,O*-Bis(trimethylsilyl)trifluoroacetamide (BSTFA) with 1% trimethylchlorosilane (TMCS) and incubated at 65° C for 30 min. One microliter of the derivatized samples was injected to GC-MS in splitless mode. GC-MS analysis was performed using an Agilent 6890 GC interfaced to an Agilent 5973 quadrupole MS with a HP-5ms column (30 m x 0.25 mm x 0.25 μm, Agilent). The temperature gradient was programmed from 70 to 320° C at 5° C/min with helium flow rate at 1.0 mL/min and inlet temperature at 280^{o} C. EI-MS ionization energy was set to 70 eV and the interface temperature was 280° C.

Amino acid analysis

Amino acids analysis was carried out following a method similar to that previously described by Guan et al. (Guan et al., 2015). About 10 mg of lyophilized maize seed powders were extracted with 1 mL of hot water at 85° C for 30 min, and spiked with 10 µM butylamine internal standard. The samples were briefly centrifuged for 5 min, passed through a syringe filter with 0.2 µm pore size, and subjected to LC-fluorescence amino acid analysis with pre-column derivatization of primary amino acids with o-phthaldialdehyde (OPA).

LC-fluorescence analysis was performed using an Agilent 1110 HPLC with a fluorescence detector (FLD) with a Hypersil ODS C18 reverse phase column (250mm x 4mm, 5µm; Thermo). Excitation and emission wavelengths for FLD were set at 337 nm and 454 nm, respectively. Solvent system used were buffer A (10% methanol (MeOH) in 10 mM NaH_2PO_4, pH 7.3), buffer B (80% MeOH in 10 mM NaH_2PO_4, pH 7.3), and OPA solution (12.25 mg OPA in 312.5 µL MeOH, 6 mL 0.4 M borate buffer and 19.22 µL mercaptoethanol). The pre-column OPA derivatization reaction was achieved using an in-loop-reaction program. Solvent program was a linear gradient from 100% buffer A to 100% buffer B in 46 min at flow rate of 1 ml/min. Amino acid standard mixture included butylamine and 18 of the 20 proteogenic amino acids, at the concentration of 10mM each. Cys and Pro cannot be analyzed by this method and were not included as standards. The amino acid standard mixture was used to calculate the response factors for the detector, and butylamine was used to generate a standard curve.

Data Analysis

Three biological replicates were used for GC or LC analysis of the extracts. Those compounds that were observed in two or three datasets were subjected to statistical analysis and reported here. For those compounds observed only in two data sets, the missing values were replaced by 1/3 of the estimated minimum value. Log2 ratio plots were calculated for each metabolite as previously described (Quanbeck et al., 2012). The raw data and averages and standard error calculations were determined from three biological replicates and are available in the PMR database and Supplemental Tables (i.e, Table S2, S3 and S4) respectively. Student t-test were used to calculate p-values.

The GC/MS data files were deconvoluted and searched against an in-house MS-library and NIST 14 Mass Spectral Library using NIST AMDIS software (Stein, 1999). Total metabolite analysis results obtained with GC-MS and amino acid analysis from LC-fluorescence are publicly available in the PMR database (http://metnetdb.org/PMR/)(Hur et al., 2013). They are available from the site in the name of ‘Seed Germination’ under the species of ‘Zea mays’.

Acknowledgments

Metabolomics analyses were conducted at the Iowa State University WM Keck Metabolomics Research Laboratory, and we acknowledge Ann M. Perera for her expert advice.

References

Anzala F, Morère-Le Paven M-C, Fournier S, Rondeau D, Limami AM (2006) Physiological and molecular aspects of aspartate-derived amino acid metabolism during germination and post-germination growth in two maize genotypes differing in germination efficiency. Journal of experimental botany **57:** 645-653

Bates PD, Stymne S, Ohlrogge J (2013) Biochemical pathways in seed oil synthesis. Current opinion in plant biology **16:** 358-364

Bernier AM, Ballance GM (1993) INDUCTION AND SECRETION OF ALPHA-AMYLASE, (1-3),(1- 4)-BETA-GLUCANASE, AND (1- 3)-BETA-GLUCANASE ACTIVITIES IN GIBBERELLIC-ACID AND CACL2-TREATED HALF SEEDS AND ALEURONES OF WHEAT. Cereal Chemistry **70:** 127-132

Bewley JD (1997) Seed germination and dormancy. The plant cell **9:** 1055

Bewley JD (2001) Seed Germination and Reserve Mobilization. eLS

Bewley JD, Bradford K, Hilhorst H (2012) Seeds: physiology of development, germination and dormancy. Springer Science & Business Media

Cao S, Zhou X-R, Wood CC, Green AG, Singh SP, Liu L, Liu Q (2013) A large and functionally diverse family of Fad2 genes in safflower (Carthamus tinctorius L.). BMC plant biology **13:** 1

Chrispeels MJ, Varner J (1967) Hormonal control of enzyme synthesis: on the mode of action of gibberellic acid and abscisin in aleurone layers of barley. Plant physiology **42:** 1008-1016

Dante RA, Larkins BA, Sabelli PA (2015) Cell cycle control and seed development. Advances in Seed Biology**:** 21

Dietrich CR, Perera M, D Yandeau‐Nelson M, Meeley RB, Nikolau BJ, Schnable PS (2005) Characterization of two GL8 paralogs reveals that the 3‐ketoacyl reductase component of fatty acid elongase is essential for maize (Zea mays L.) development. The Plant Journal **42:** 844-861

Feenstra AD, Hansen RL, Lee YJ (2015) Multi-matrix, dual polarity, tandem mass spectrometry imaging strategy applied to a germinated maize seed: toward mass spectrometry imaging of an untargeted metabolome. Analyst **140:** 7293-7304

Fincher GB (1989) Molecular and cellular biology associated with endosperm mobilization in germinating cereal grains. Annual review of plant biology **40:** 305-346

Firenzuoli A, Vanni P, Ramponi G, Baccari V (1968) Changes in enzyme levels during germination of seeds of Triticum durum. Plant physiology **43:** 260-264

Frank T, Scholz B, Peter S, Engel K-H (2011) Metabolite profiling of barley: Influence of the malting process. Food chemistry **124:** 948-957

Fu Y, Wen T-J, Ronin YI, Chen HD, Guo L, Mester DI, Yang Y, Lee M, Korol AB, Ashlock DA (2006) Genetic dissection of intermated recombinant inbred lines using a new genetic map of maize. Genetics **174:** 1671-1683

Fujino Y, Ohnishi M, Ito S (1985) Molecular species of ceramide and mono-, di-, tri-, and tetraglycosylceramide in bran and endosperm of rice grains. Agricultural and biological chemistry **49:** 2753-2762

Guan X, Chen H, Abramson A, Man H, Wu J, Yu O, Nikolau BJ (2015) A phosphopantetheinyl transferase that is essential for mitochondrial fatty acid biosynthesis. The Plant Journal **84:** 718-732

Hankin JA, Barkley RM, Murphy RC (2007) Sublimation as a method of matrix application for mass spectrometric imaging. Journal of the American Society for Mass Spectrometry **18:** 1646-1652

He M, Zhu C, Dong K, Zhang T, Cheng Z, Li J, Yan Y (2015) Comparative proteome analysis of embryo and endosperm reveals central differential expression proteins involved in wheat seed germination. BMC plant biology **15:** 1

Hirsch CN, Foerster JM, Johnson JM, Sekhon RS, Muttoni G, Vaillancourt B, Peñagaricano F, Lindquist E, Pedraza MA, Barry K (2014) Insights into the maize pan-genome and pan-transcriptome. The Plant Cell **26:** 121-135

Horn PJ, Korte AR, Neogi PB, Love E, Fuchs J, Strupat K, Borisjuk L, Shulaev V, Lee Y-J, Chapman KD (2012) Spatial mapping of lipids at cellular resolution in embryos of cotton. The Plant Cell **24:** 622-636

Horn PJ, Silva JE, Anderson D, Fuchs J, Borisjuk L, Nazarenus TJ, Shulaev V, Cahoon EB, Chapman KD (2013) Imaging heterogeneity of membrane and storage lipids in transgenic Camelina sativa seeds with altered fatty acid profiles. The Plant Journal **76:** 138-150

Hou W, Zhou H, Khalil MB, Seebun D, Bennett SA, Figeys D (2011) Lyso‐form fragment ions facilitate the determination of stereospecificity of diacyl glycerophospholipids. Rapid Communications in Mass Spectrometry **25:** 205-217

Hu S, Lübberstedt T, Zhao G, Lee M (2016) QTL Mapping of Low-Temperature Germination Ability in the Maize IBM Syn4 RIL Population. PloS one **11:** e0152795

Hur M, Campbell AA, Almeida-de-Macedo M, Li L, Ransom N, Jose A, Crispin M, Nikolauh BJ, Wurtele ES (2013) A global approach to analysis and interpretation of metabolic data for plant natural product discovery. Natural Product Reports **30:** 565-583

Ingle J, Beevers L, Hageman R (1964) Metabolic changes associated with the germination of corn. I. Changes in weight and metabolites and their redistribution in the embryo axis, scutellum, and endosperm. Plant physiology **39:** 735

Kaspar S, Peukert M, Svatos A, Matros A, Mock HP (2011) MALDI‐imaging mass spectrometry–An emerging technique in plant biology. Proteomics **11:** 1840-1850

Kolesnick R (2002) The therapeutic potential of modulating the ceramide/sphingomyelin pathway. The Journal of clinical investigation **110:** 3-8

Kollipara KP, Saab IN, Wych RD, Lauer MJ, Singletary GW (2002) Expression profiling of reciprocal maize hybrids divergent for cold germination and desiccation tolerance. Plant Physiology **129:** 974-992

Korte AR, Yandeau-Nelson MD, Nikolau BJ, Lee YJ (2015) Subcellular-level resolution MALDI-MS imaging of maize leaf metabolites by MALDI-linear ion trap-Orbitrap mass spectrometer. Analytical and bioanalytical chemistry **407:** 2301-2309

Lai J, Li R, Xu X, Jin W, Xu M, Zhao H, Xiang Z, Song W, Ying K, Zhang M (2010) Genome-wide patterns of genetic variation among elite maize inbred lines. Nature genetics **42:** 1027-1030

Larson G, Piperno DR, Allaby RG, Purugganan MD, Andersson L, Arroyo-Kalin M, Barton L, Vigueira CC, Denham T, Dobney K (2014) Current perspectives and the future of domestication studies. Proceedings of the National Academy of Sciences **111:** 6139-6146

Lee YJ, Perdian DC, Song Z, Yeung ES, Nikolau BJ (2012) Use of mass spectrometry for imaging metabolites in plants. The Plant Journal **70:** 81-95

Leonova S, Grimberg Å, Marttila S, Stymne S, Carlsson AS (2010) Mobilization of lipid reserves during germination of oat (Avena sativa L.), a cereal rich in endosperm oil. Journal of experimental botany **61:** 3089-3099

Levy M, Futerman AH (2010) Mammalian ceramide synthases. IUBMB life **62:** 347-356

Limami AM, Rouillon C, Glevarec G, Gallais A, Hirel B (2002) Genetic and physiological analysis of germination efficiency in maize in relation to nitrogen metabolism reveals the importance of cytosolic glutamine synthetase. Plant Physiology **130:** 1860-1870

Liu W-Y, Chang Y-M, Chen SC-C, Lu C-H, Wu Y-H, Lu M-YJ, Chen D-R, Shih AC-C, Sheue C-R, Huang H-C (2013) Anatomical and transcriptional dynamics of maize embryonic leaves during seed germination. Proceedings of the National Academy of Sciences **110:** 3979-3984

Lu H, Bernardo R (2001) Molecular marker diversity among current and historical maize inbreds. Theoretical and Applied Genetics **103:** 613-617

Luttgeharm KD, Chen M, Mehra A, Cahoon RE, Markham JE, Cahoon EB (2015) Overexpression of Arabidopsis ceramide synthases differentially affects growth, sphingolipid metabolism, programmed cell death, and mycotoxin resistance. Plant physiology **169:** 1108-1117

Lynch DV, Dunn TM (2004) An introduction to plant sphingolipids and a review of recent advances in understanding their metabolism and function. New phytologist **161:** 677-702

Markham JE, Lynch DV, Napier JA, Dunn TM, Cahoon EB (2013) Plant sphingolipids: function follows form. Current opinion in plant biology **16:** 350-357

McDonnell LA, Heeren R (2007) Imaging mass spectrometry. Mass spectrometry reviews **26:** 606-643

McDonnell LA, Heeren RMA (2007) Imaging mass spectrometry. Mass Spectrometry Reviews **26:** 606-643

Munamava MR, Goggi AS, Pollak L (2004) Seed quality of maize inbred lines with different composition and genetic backgrounds. Crop science **44:** 542-548

Nonogaki H (2008) Seed germination and reserve mobilization. eLS

Quanbeck SMM, Brachova L, Campbell AA, Guan X, Perera A, He K, Rhee SY, Bais P, Dickerson J, Dixon P (2012) Metabolomics as a hypothesis-generating functional genomics tool for the annotation of Arabidopsis thaliana genes of “unknown function”. Frontiers in plant science **3:** 15

Römisch-Margl L, Spielbauer G, Schützenmeister A, Schwab W, Piepho H-P, Genschel U, Gierl A (2010) Heterotic patterns of sugar and amino acid components in developing maize kernels. Theoretical and Applied Genetics **120:** 369-381

Samuels KMS, Wada H, Welti R, Xu C, Zallot R, Ohlrogge J (2013) Acyl-lipid metabolism. The Arabidopsis Book **1:** 70

Sánchez-Linares L, Gavilanes-Ruíz M, Díaz-Pontones D, Guzmán-Chávez F, Calzada-Alejo V, Zurita-Villegas V, Luna-Loaiza V, Moreno-Sánchez R, Bernal-Lugo I, Sánchez-Nieto S (2012) Early carbon mobilization and radicle protrusion in maize germination. Journal of experimental botany**:** ers130

Schmidt MA, Barbazuk WB, Sandford M, May G, Song Z, Zhou W, Nikolau BJ, Herman EM (2011) Silencing of soybean seed storage proteins results in a rebalanced protein composition preserving seed protein content without major collateral changes in the metabolome and transcriptome. Plant Physiology **156:** 330-345

Schnable PS, Ware D, Fulton RS, Stein JC, Wei F, Pasternak S, Liang C, Zhang J, Fulton L, Graves TA (2009) The B73 maize genome: complexity, diversity, and dynamics. science **326:** 1112-1115

Shu X-L, Frank T, Shu Q-Y, Engel K-H (2008) Metabolite profiling of germinating rice seeds. Journal of agricultural and food chemistry **56:** 11612-11620

Springer NM, Ying K, Fu Y, Ji T, Yeh C-T, Jia Y, Wu W, Richmond T, Kitzman J, Rosenbaum H (2009) Maize inbreds exhibit high levels of copy number variation (CNV) and presence/absence variation (PAV) in genome content. PLoS Genet **5:** e1000734

Stein SE (1999) An integrated method for spectrum extraction and compound identification from gas chromatography/mass spectrometry data. Journal of the American Society for Mass Spectrometry **10:** 770-781

Swanson-Wagner RA, Eichten SR, Kumari S, Tiffin P, Stein JC, Ware D, Springer NM (2010) Pervasive gene content variation and copy number variation in maize and its undomesticated progenitor. Genome research **20:** 1689-1699

Toue S, Sugiura Y, Kubo A, Ohmura M, Karakawa S, Mizukoshi T, Yoneda J, Miyano H, Noguchi Y, Kobayashi T (2014) Microscopic imaging mass spectrometry assisted by on‐tissue chemical derivatization for visualizing multiple amino acids in human colon cancer xenografts. Proteomics **14:** 810-819

Troyer AF (2004) Persistent and popular germplasm in seventy centuries of corn evolution. Corn: Origin, History, and Production. John Wiley & Sons, Hoboken, NJ**:** 133-231

Troyer AF (2009) Development of hybrid corn and the seed corn industry. *In* Handbook of maize. Springer, pp 87-114

van Hove ERA, Smith DF, Heeren RM (2010) A concise review of mass spectrometry imaging. Journal of Chromatography A **1217:** 3946-3954

Vroh Bi I, McMullen M, Sanchez-Villeda H, Schroeder S, Gardiner J, Polacco M, Soderlund C, Wing R, Fang Z, Coe E (2006) Single nucleotide polymorphisms and insertion–deletions for genetic markers and anchoring the maize fingerprint contig physical map. Crop science **46:** 12-21

Williams LD, Glenn AE, Zimeri AM, Bacon CW, Smith MA, Riley RT (2007) Fumonisin disruption of ceramide biosynthesis in maize roots and the effects on plant development and Fusarium verticillioides-induced seedling disease. Journal of agricultural and food chemistry **55:** 2937-2946

Zavalin A, Yang J, Caprioli R (2013) Laser beam filtration for high spatial resolution MALDI imaging mass spectrometry. Journal of the American Society for Mass Spectrometry **24:** 1153-1156

Zeeman SC, Delatte T, Messerli G, Umhang M, Stettler M, Mettler T, Streb S, Reinhold H, Kötting O (2007) Starch breakdown: recent discoveries suggest distinct pathways and novel mechanisms. *In*, Vol 34. CSIRO Publishing, Functional Plant Biology, pp 465-473

Zhang M, Fan J, Taylor DC, Ohlrogge JB (2009) DGAT1 and PDAT1 acyltransferases have overlapping functions in Arabidopsis triacylglycerol biosynthesis and are essential for normal pollen and seed development. The Plant Cell **21:** 3885-3901

Figures

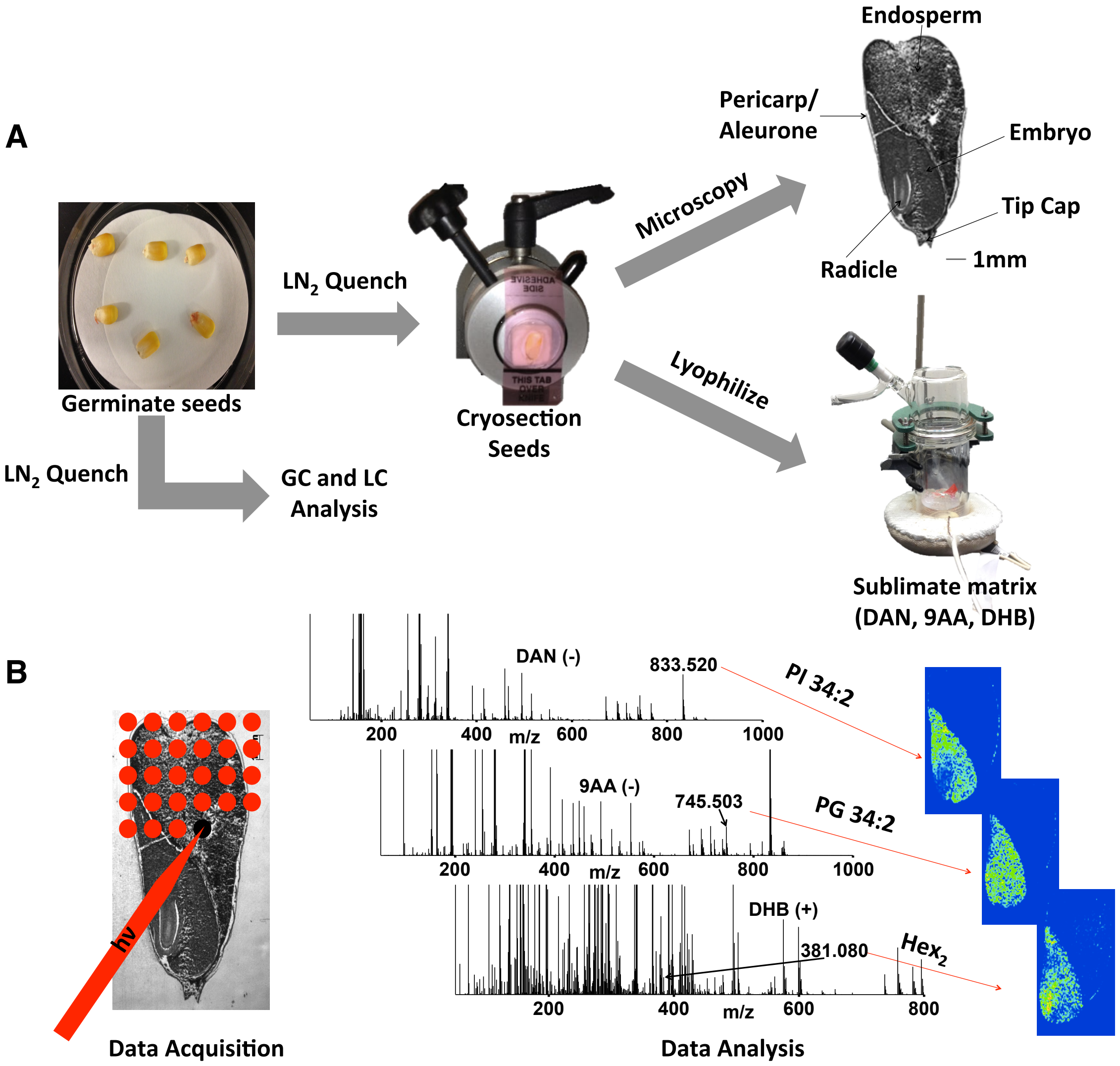

Fig. 1. Illustration of experimental workflow. **(A)** Sample preparation: Seeds were germinated in a petri dish and quenched at the desired time point with liquid nitrogen (LN_2). Some samples were selected for metabolite profiling analysis. The remaining samples were cryo-sectioned at 10 µm thickness for microscopic and MSI analysis. **(B)** MSI data acquisition and analysis: The laser was rastered across the tissue sample, collecting a spectrum at every x-y position. Resulting mass spectra were evaluated and MS images were generated for individual ions at selected *m/z* values.

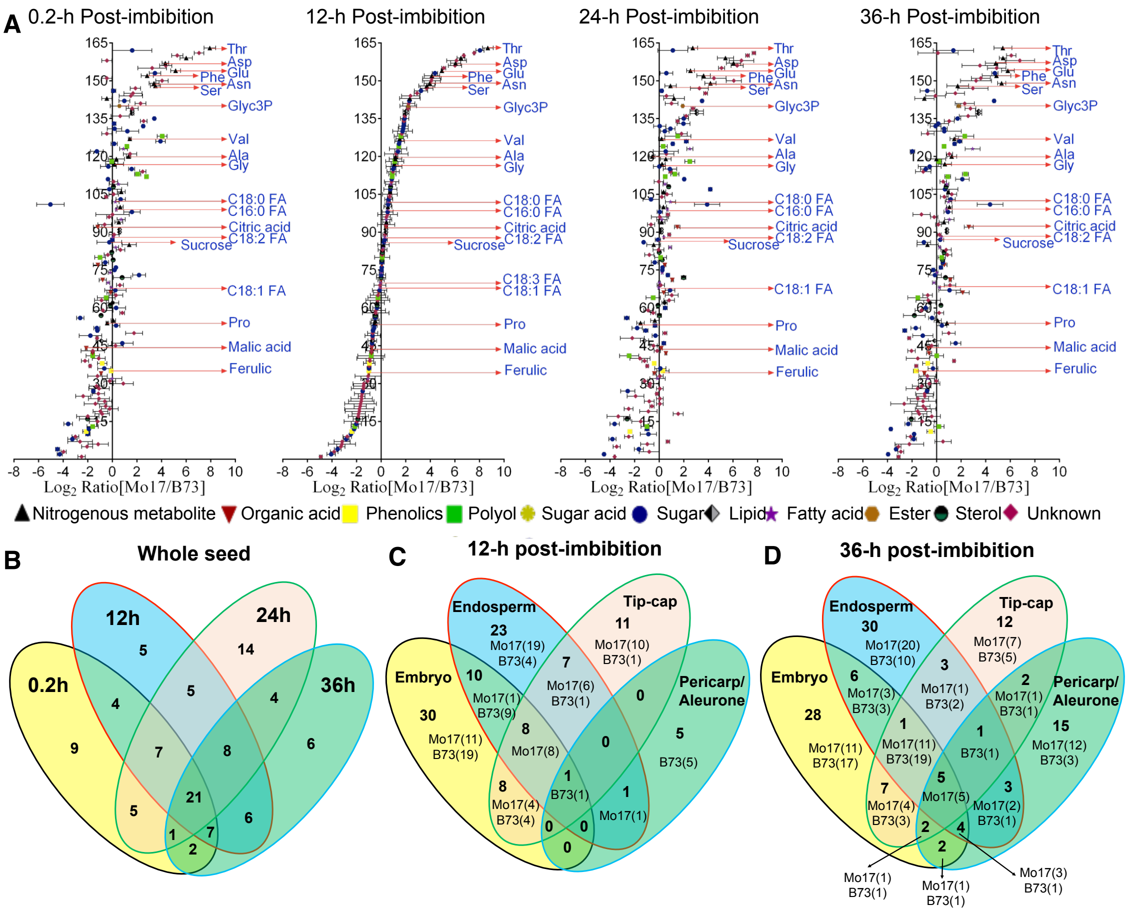

Fig. 2. Log-ratio plot comparison **(A)** and Venn-diagram representations of the differential metabolomes between Mo17 and B73 maize inbred of whole seeds **(B)** and micro-dissected organs from seeds at 12-h **(C)** and 36-h **(D)** post-imbibition. In the log-ratio plots the x-axis plots log-transformed relative abundance ratio of each metabolite in Mo17 vs B73. The y-axis plots the individual metabolites (162 analytes, 63 chemically defined), and the order of the metabolites on the y-axis is identical and ordered from the lowest to the highest value on the x-axis as determined for the 12-h post-imbibition time point. The arrows identify amino acids or those metabolites also analyzed by MSI. Glyc3P = glycerol 3-phosphate; FA = Fatty acid. The Venn-diagram in panel B represents the distribution of metabolites that are differentially expressed between Mo17 and B73 seeds ($p<0.05$) among the four post-imbibition time points. The Venn diagrams in panels C and D show metabolites that are differentially expressed between Mo17 and B73 seeds ($p<0.05$) in micro-dissected organs from germinating seeds at 12-h and 36-h post-imbibition. The identity of the inbred and the number of the metabolites that occur at higher levels is represented by the labels “inbred(x)”.

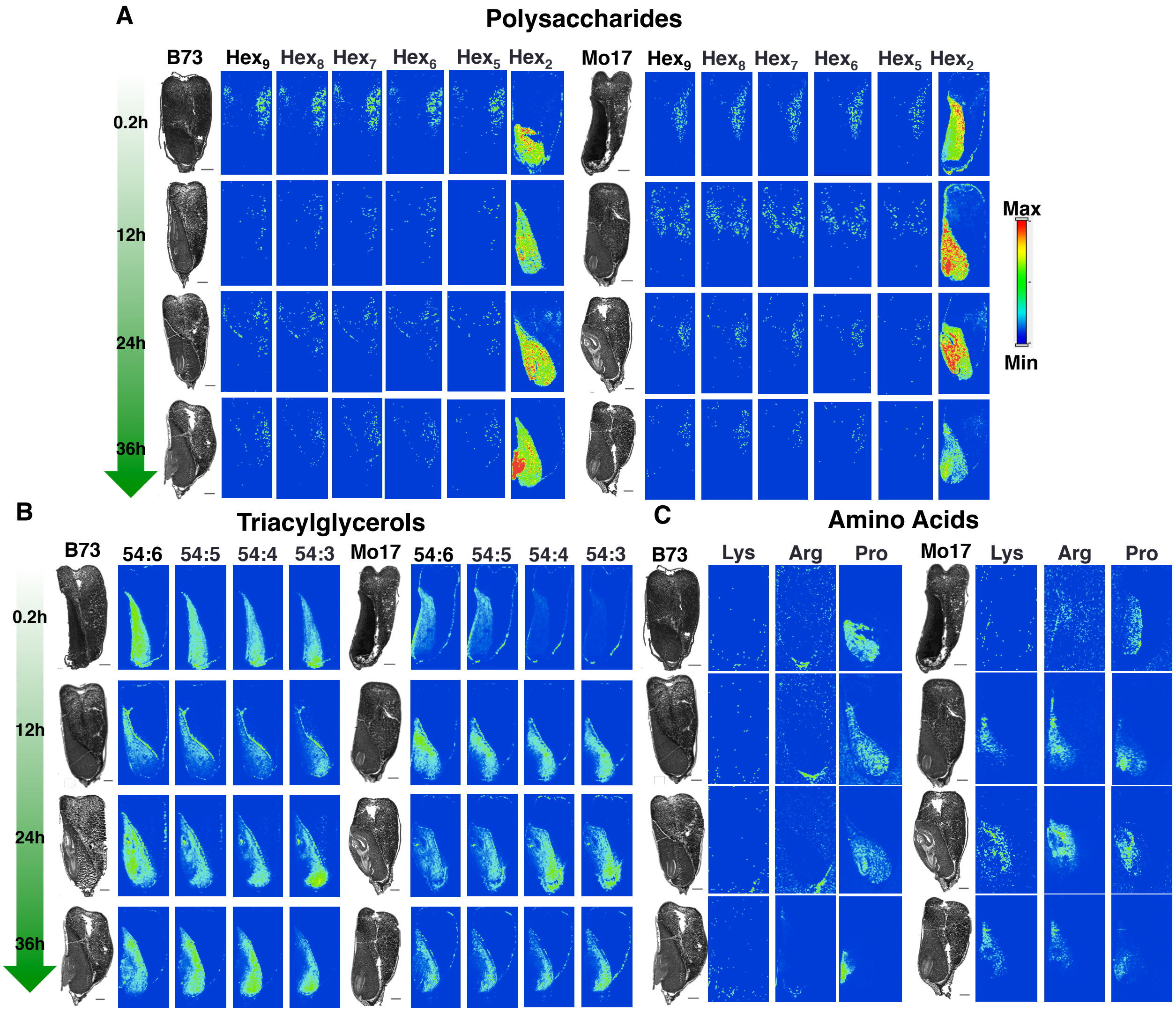

Fig. 3. MSI images of **(A)** hexose polysaccharides, **(B)** triacylglycerols, and **(C)** amino acids in germinating seeds. All ions were detected in positive ion mode with DHB as the matrix. Large polysaccharides were detected as potassium adducts of water loss, $[M\text{-}H_2O+K]^+$, likely due to in-source fragmentation during MALDI-MS data acquisition. Disaccharide and triacylglycerols were detected as potassium adducts, $[M+K]^+$, and amino acids were detected as protonated ions, $[M+H]^+$. Scale bar: 1 mm.

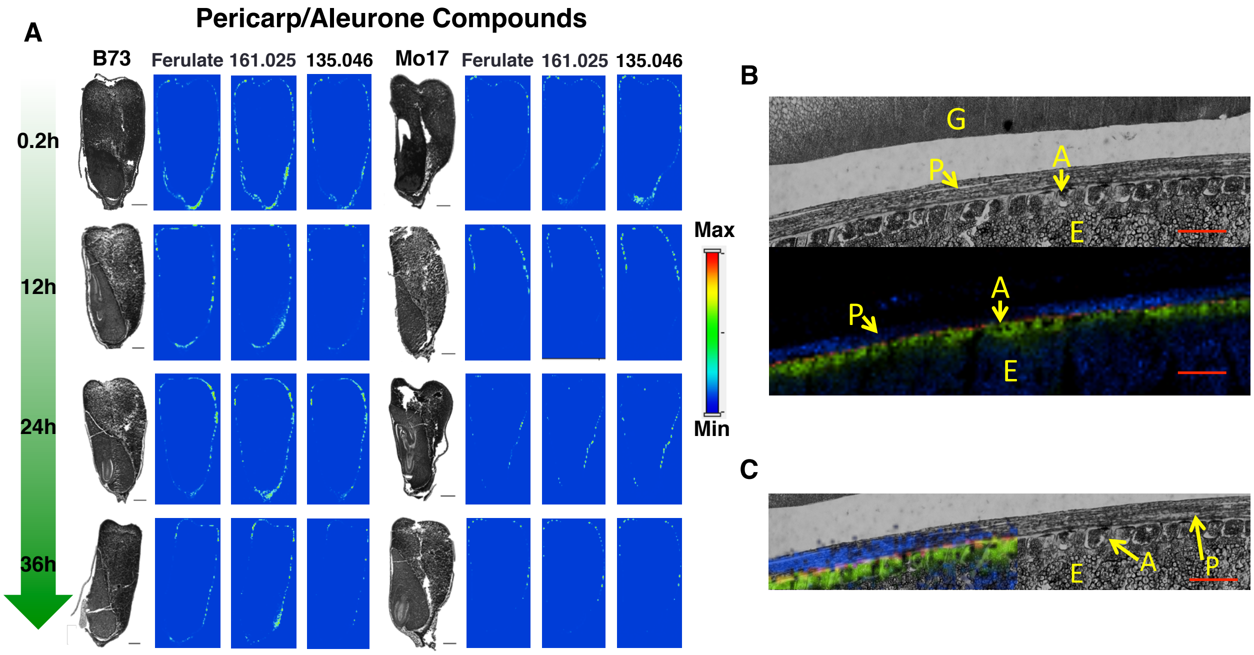

Fig. 4. **(A)** MSI of three compounds uniquely localized to the perimeter of the seed. Images were acquired in negative ion mode with DAN as matrix. No normalization was applied to these images. Scale bar: 1 mm. **(B)** Optical microscopic (Top) and MS (Bottom) images of the pericarp and aleurone layers of a B73 maize seed with 24-h post-imbibition. Morphological features are labeled on the images. G: gelatin embedding medium. P: pericarp. A: aleurone. E: endosperm. **(C)** Overlay of optical and MS images in the panel B. MS images were obtained with DAN as the matrix in negative mode. MS images in the panel B and C are ferulate (red), malate (blue), and PI 34:2 (green). All analytes were detected as deprotonated species, $[M-H]^-$. Scale bar: 100 µm.

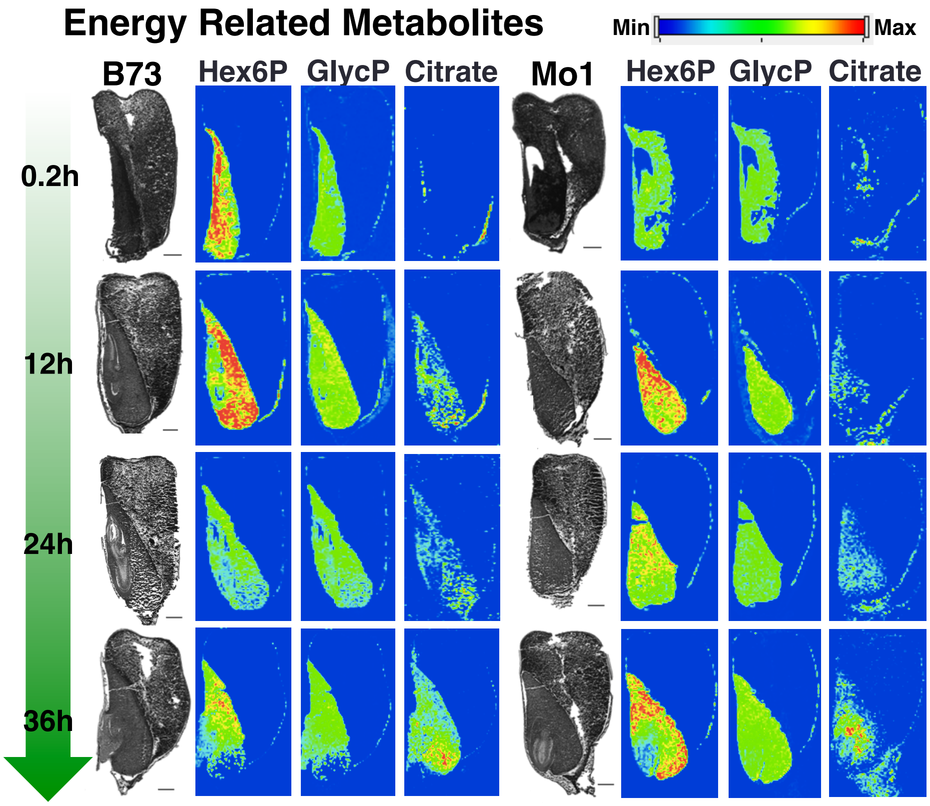

Fig. 5. Distribution of hexose phosphate (Hex6P), glycerol phosphate (GlycP), and citrate/isocitrate. Phosphorylated metabolites are detected as deprotonated water-loss species, $[M\text{-}H_2O\text{-}H]^-$, in negative ion mode with DAN as matrix. Citrate/isocitrate is detected as a deprotonated species, $[M\text{-}H]^-$, in negative ion mode with 9AA as matrix. Scale bar: 1 mm.

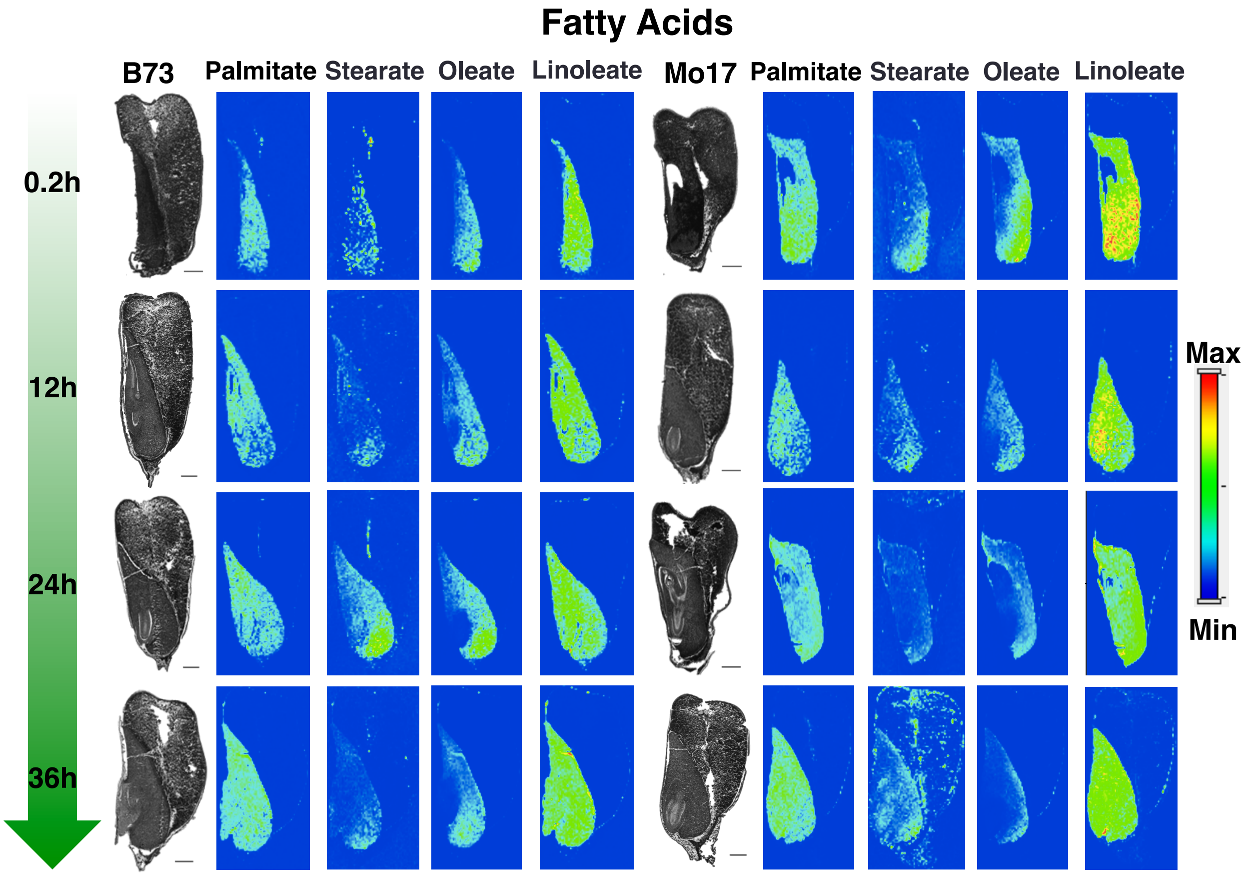

Fig. 6. Distribution of fatty acid species. All ions were detected as the deprotonated species, [M-H]$^-$, in negative ion mode with 9AA as the matrix. Scale bar: 1 mm. Stearate has some contamination from vacuum pump oil.

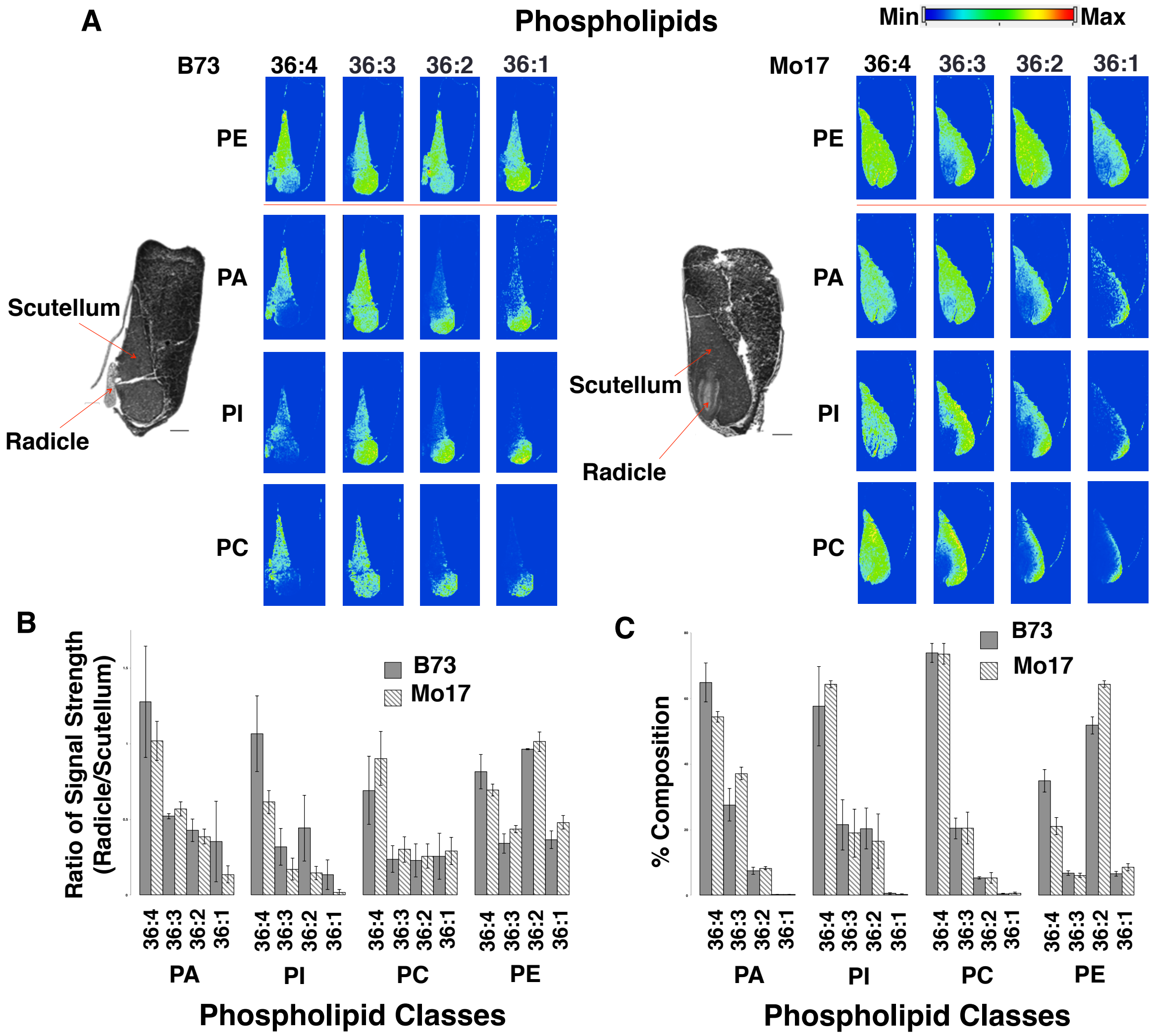

Fig. 7. Distribution and species analysis of various phospholipids. **(A)** Distribution of 16 different phospholipid molecular species in germinating seeds (36-h post imbibition). PE, PA, and PI are observed as deprotonated species, $[M-H]^-$, with DAN as the matrix in negative ion mode. PC is observed as a potassium adduct, $[M+K]^+$, with DHB matrix in positive ion mode. To allow direct comparisons, the optical images of the seeds were obtained from the adjacent cross-sections to those used to generate the MS images. Scale bar: 1 mm. Arrows in the radicle and scutellum regions of the embryo indicate the areas used to generate averaged mass spectra, from which semi-quantitative data of the phospholipids were gathered (see panels B and C). **(B)** Phospholipid ion signals in the radicle region normalized relative to the signals obtained from the scutellum. **(C)** Percentage of each molecular species within each phospholipid class in the radicle region.

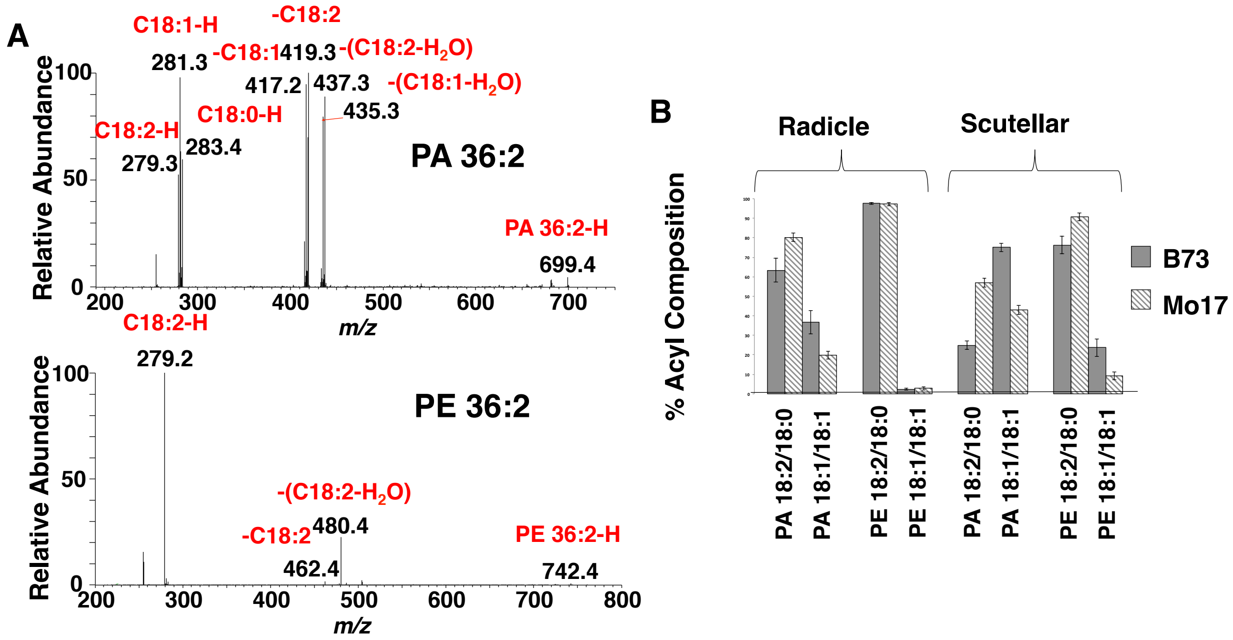

Fig. 8. MS/MS analysis of phospholipid species. **(A)** MS/MS spectra of PA 36:2 (top) and PE 36:2 (bottom) obtained from the radicle of a Mo17 inbred seed (24-hr post-imbibition). **(B)** Fatty acyl composition of different molecular species of PA 36:2 and PE 36:2, in the scutellum and radicle region of Mo17 and B73 seeds (24-hr post-imbibition).

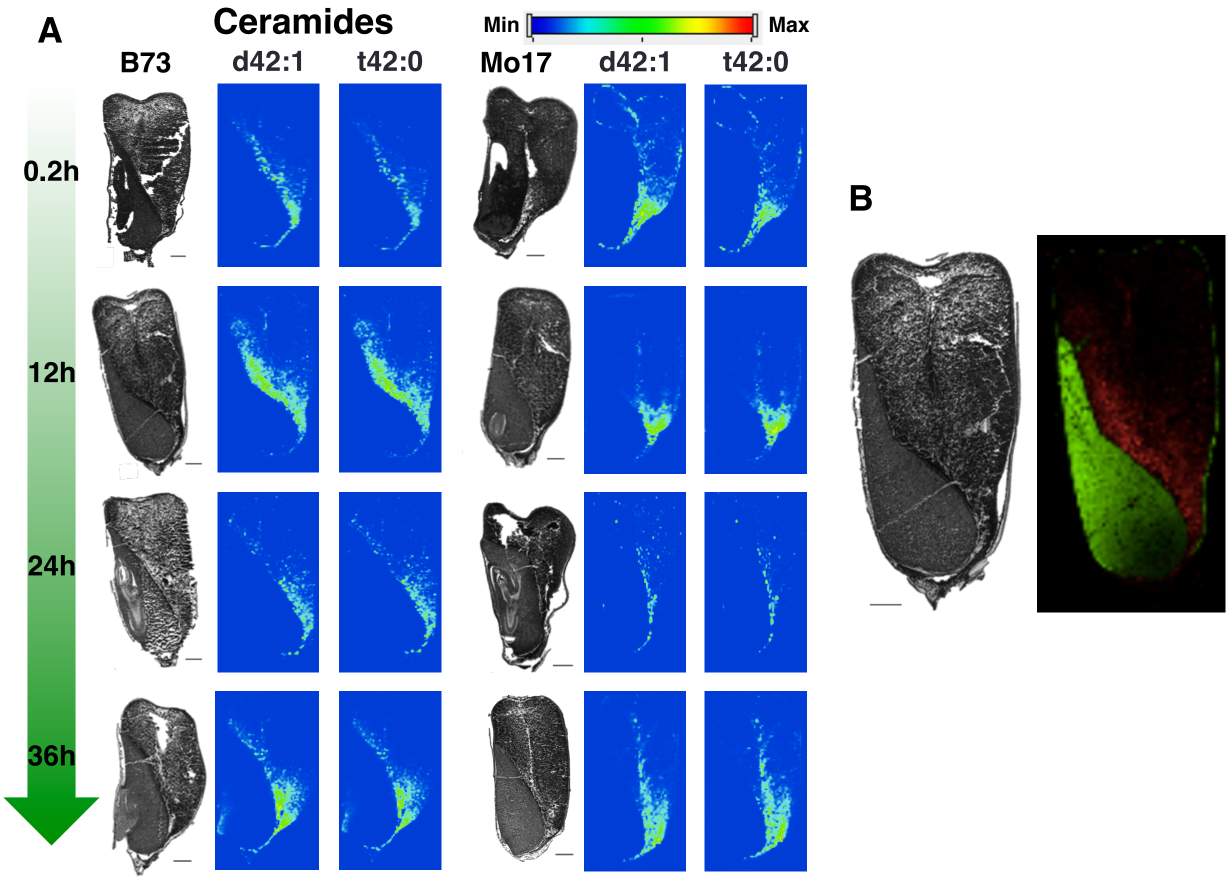

Fig. 9. Distribution of ceramide species. **(A)** Distributions of two ceramide molecular species (Cer d42:1, Cer t42:0). Both are detected as protonated species, $[M+H]^+$, in positive ion mode with DHB as the matrix. Scale bar: 1 mm. **(B)** Combined images of PC 34:2 (green) and ceramide d42:1 (red) in a B73 inbred seed at 12-h post-imbibition.

Supplemental Figures and Tables

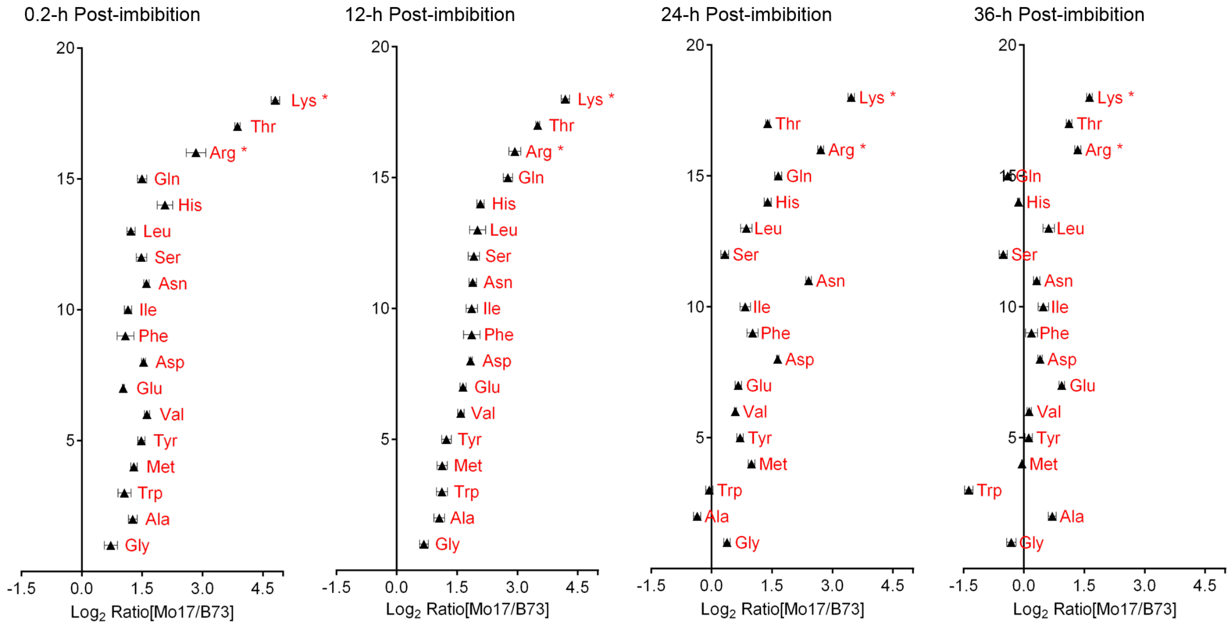

Fig. S1. Log-ratio plot comparison of the amino acid metabolome of Mo17 and B73 maize inbred seeds obtained by LC-fluorescence analysis. The x-axis plots log-transformed relative abundance ratio of each amino acid in Mo17 vs B73. The y-axis plots the 18 amino acids, with the order identical and ordered from the lowest to the highest value on the x-axis as determined for the 12-h post-imbibition time point. The asterisks denote amino acids that are reliably detected in MSI.

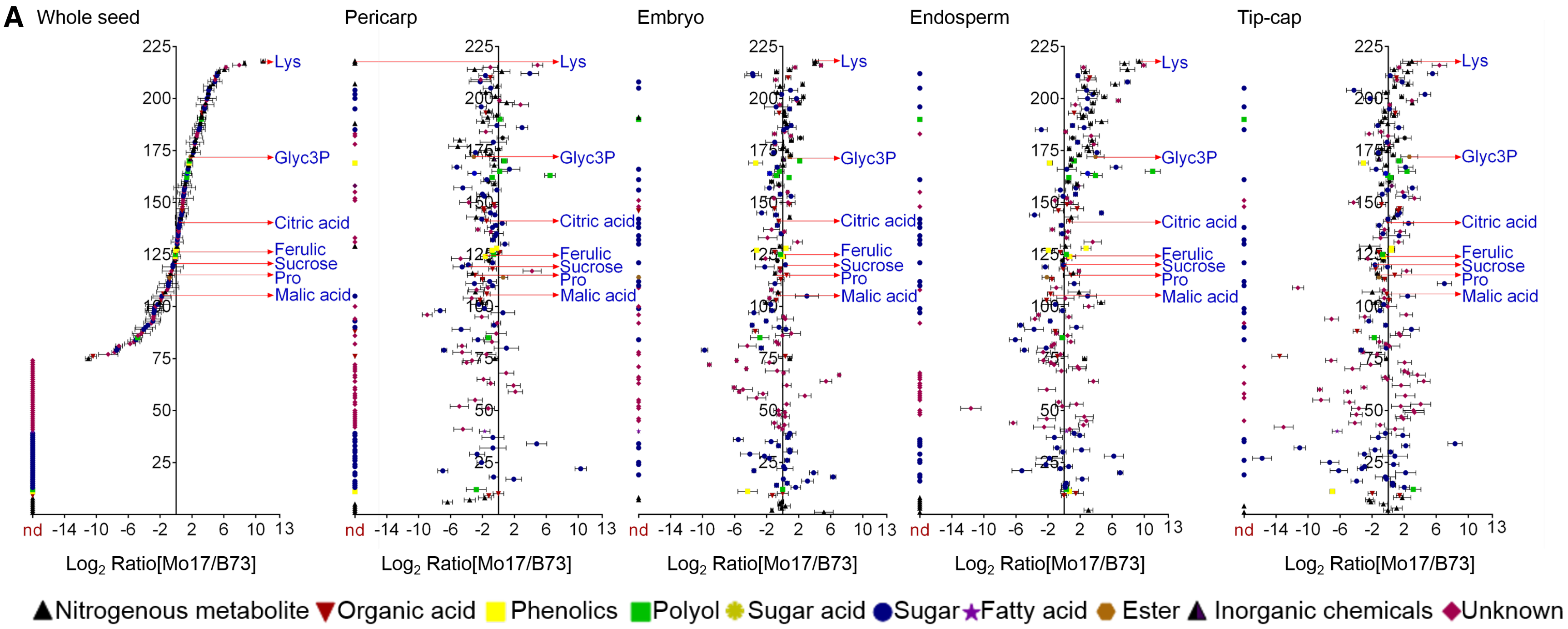
A
Whole seed
Pericarp
Embryo
Endosperm
Tip-cap
225
200
175
150
125
100
75
50
25
Lys
Glyc3P
Citric acid
Ferulic
Sucrose
Pro
Malic acid
nd -14 -10 -6 -2 2 6 10 13
Log$_2$ Ratio[Mo17/B73]
▲Nitrogenous metabolite ▼Organic acid ■Phenolics ■Polyol ✸Sugar acid ●Sugar ★Fatty acid ⬢Ester ▲Inorganic chemicals ◆Unknown

Fig. S2. (cont'd)

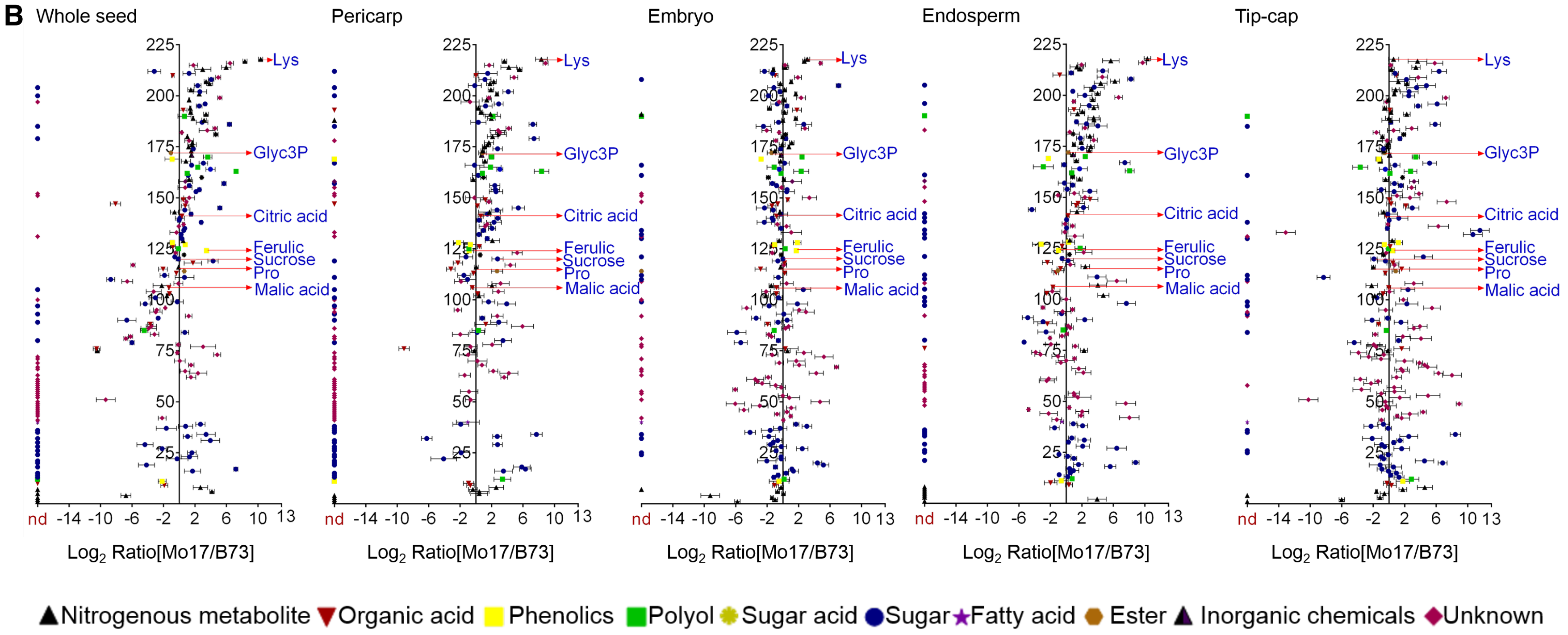

Fig. S2. Log-ratio plot comparison of the total metabolome from the whole seed and a few different organ tissues of Mo17 and B73 maize inbred seeds at 12-h (A) and 36-h (B) post-imbibition. The x-axis plots log-transformed relative abundance ratio of each metabolite in Mo17 vs B73. The y-axis plots the individual metabolites, ordered from the lowest to the highest value on the x-axis as determined for the 12-h post-imbibition time point of the whole seed. The arrows denote the metabolites that are also detected in MSI and shown in this work. Glyc3P = Glycerol 3-phosphate. “nd” on x-axis indicates metabolites that are not detected in the particular organ tissues.

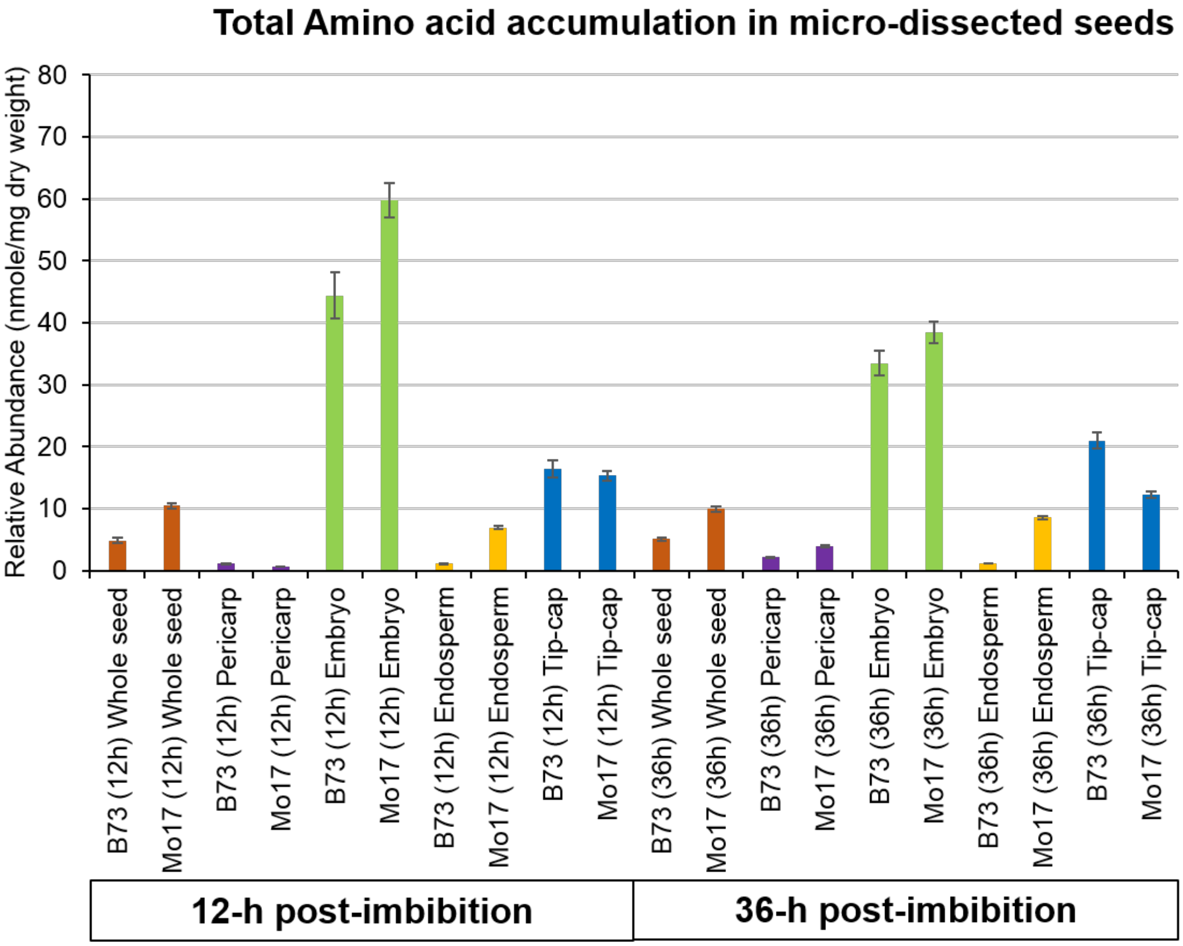

Fig. S3. Compartmentalization of total amino acids in maize seeds obtained from GC-MS data at 12-h and 36-h post-imbibition. The y-axis denotes the summed amino acid abundance calculated with ribitol as internal standard.

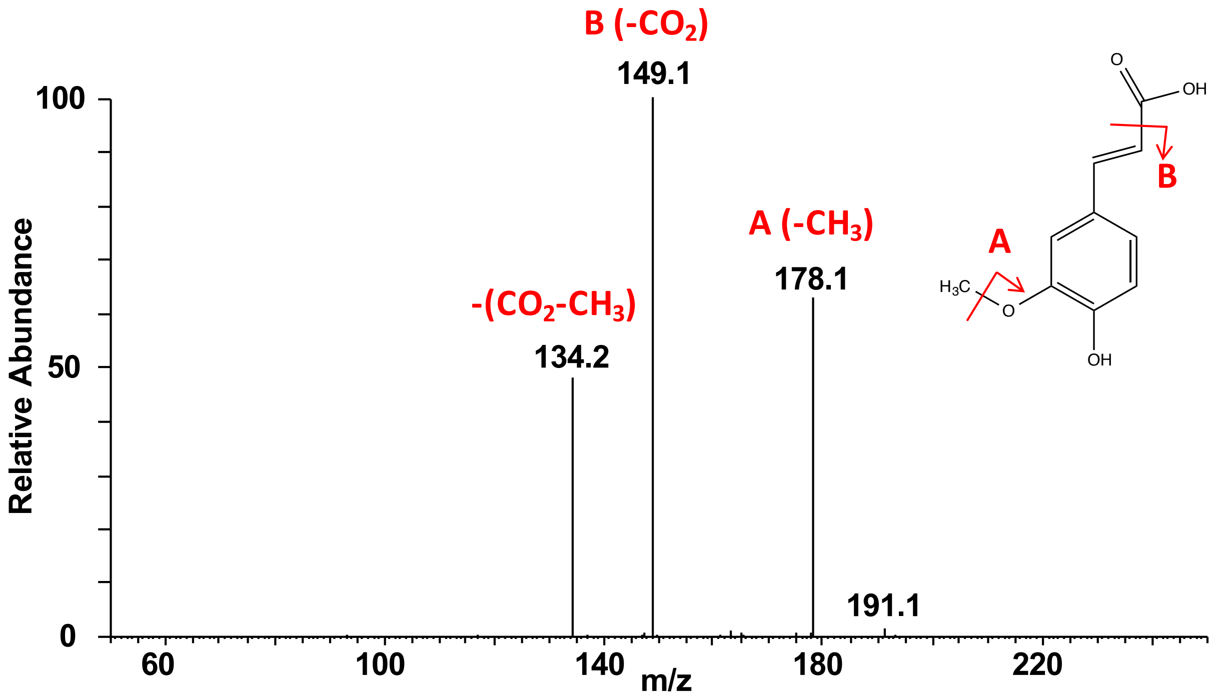

Fig. S4. MS/MS spectrum for *m/z* 193.051 from the aleurone layer of a 24 h germinated B73 seed with DAN as the matrix in negative ion mode. The same MS/MS spectrum was acquired for ferulic acid standard.

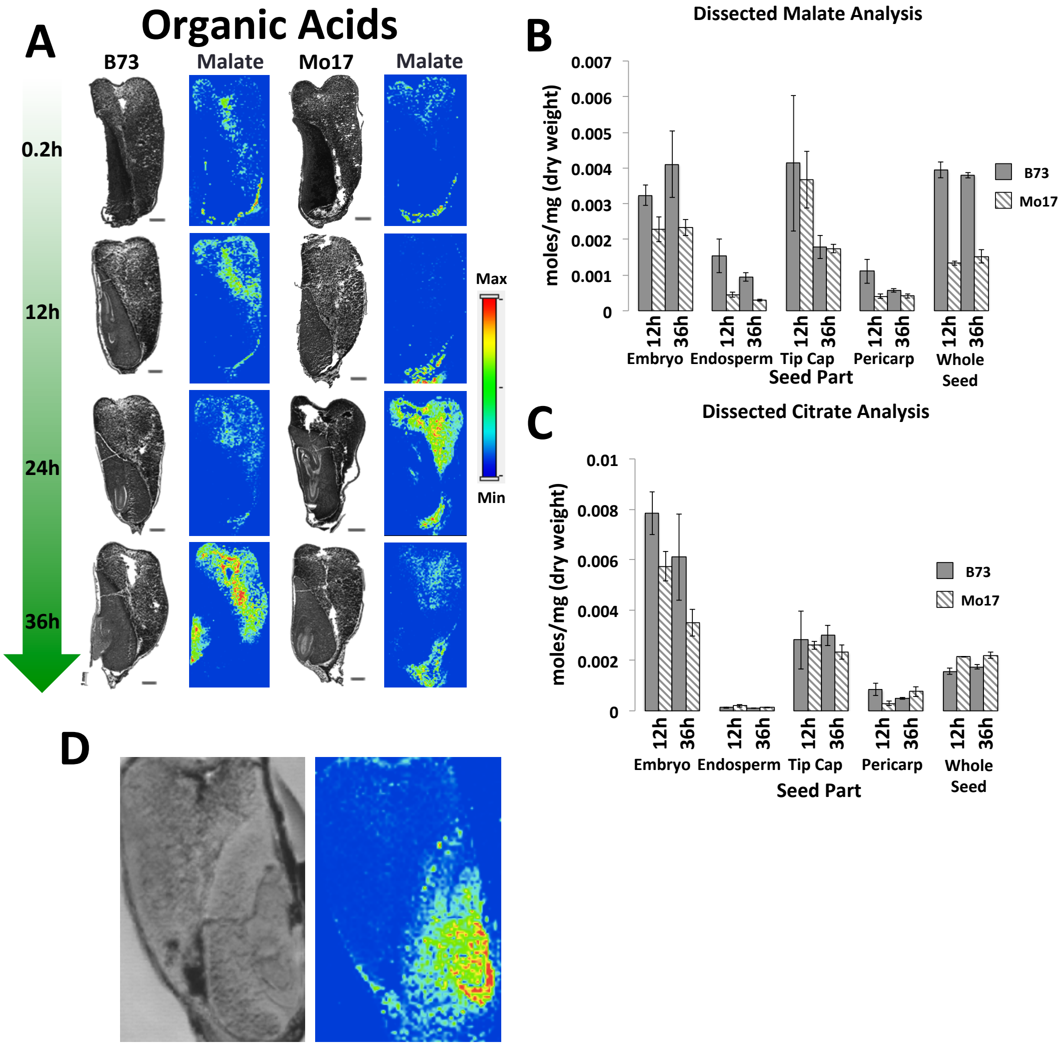

Fig. S5. Malic acid analysis. **(A)** Images of malate distribution across all four time points in seeds on B73 and Mo17 inbreds. Images were acquired with 9AA as the matrix in negative ion mode. Scale bar: 1mm. **(B)** GC-MS analysis of malate from the dissected seeds of B73 and Mo17 at 12-h and 36-h post-imbibition. These results indicate that malic acid should be more abundant in the embryo than endosperm of the seeds, which is in contrast with the images in panel A but agreement with panel D. **(C)** GC-MS analysis of citrate from the dissected seeds of B73 and Mo17 maize seeds at 12-h and 36-h post-imbibition. These results indicate that citrate is mostly localized to the embryo of the seed, in agreement with the images in Figure 5. **(D)** Image of malate on a 24-h post-imbibition Mo17 tissue sectioned and imaged the same day as it was harvested. The image displays malate localized to the embryo of the seed. The image was acquired with 9AA as the matrix in negative mode.

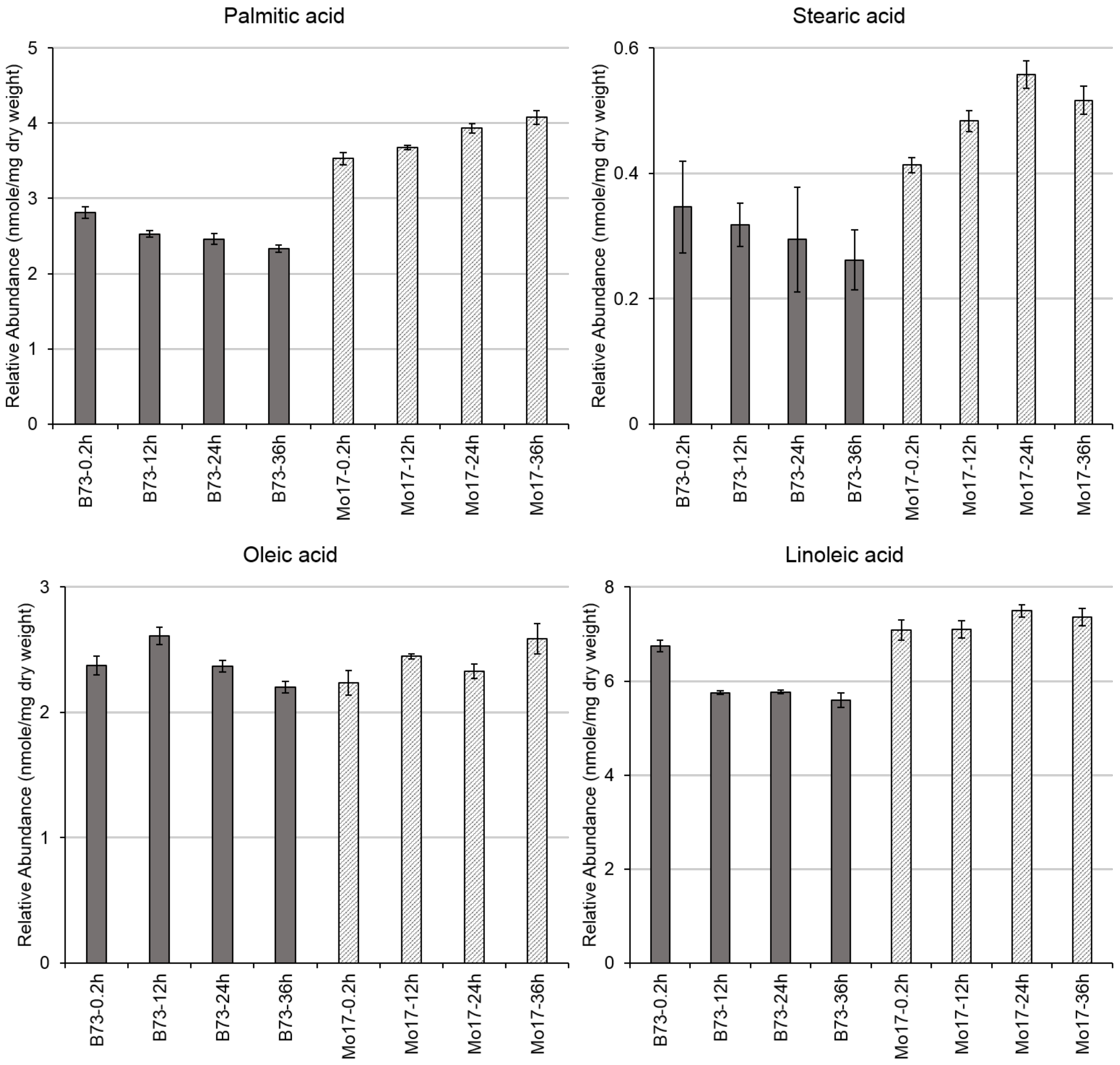

Fig. S6. GC-MS analysis of whole seeds for fatty acid species seen in MSI. From this data, only minor abundance differences between inbreds can be seen for the fatty acids. However, examination of MSI images shows significant differences in their localizations within the embryo.

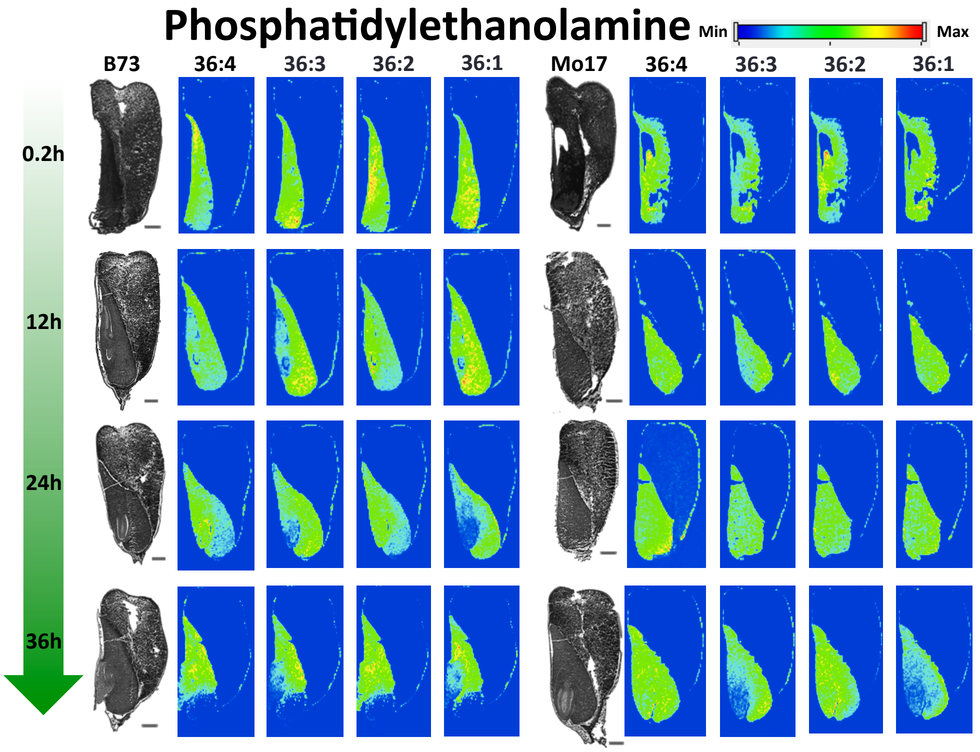
Phosphatidylethanolamine
Min
Max
B73
36:4
36:3
36:2
36:1
Mo17
36:4
36:3
36:2
36:1
0.2h
12h
24h
36h

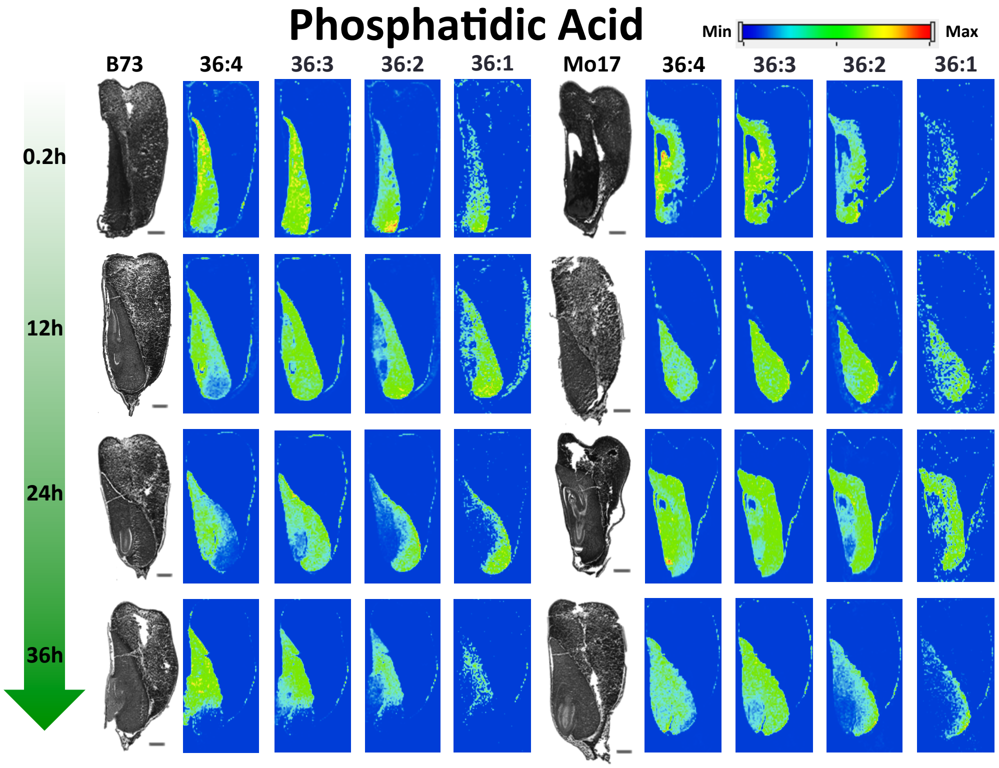
Phosphatidic Acid
Min
Max
B73
36:4
36:3
36:2
36:1
Mo17
36:4
36:3
36:2
36:1
0.2h
12h
24h
36h

Fig. S7. (cont'd)

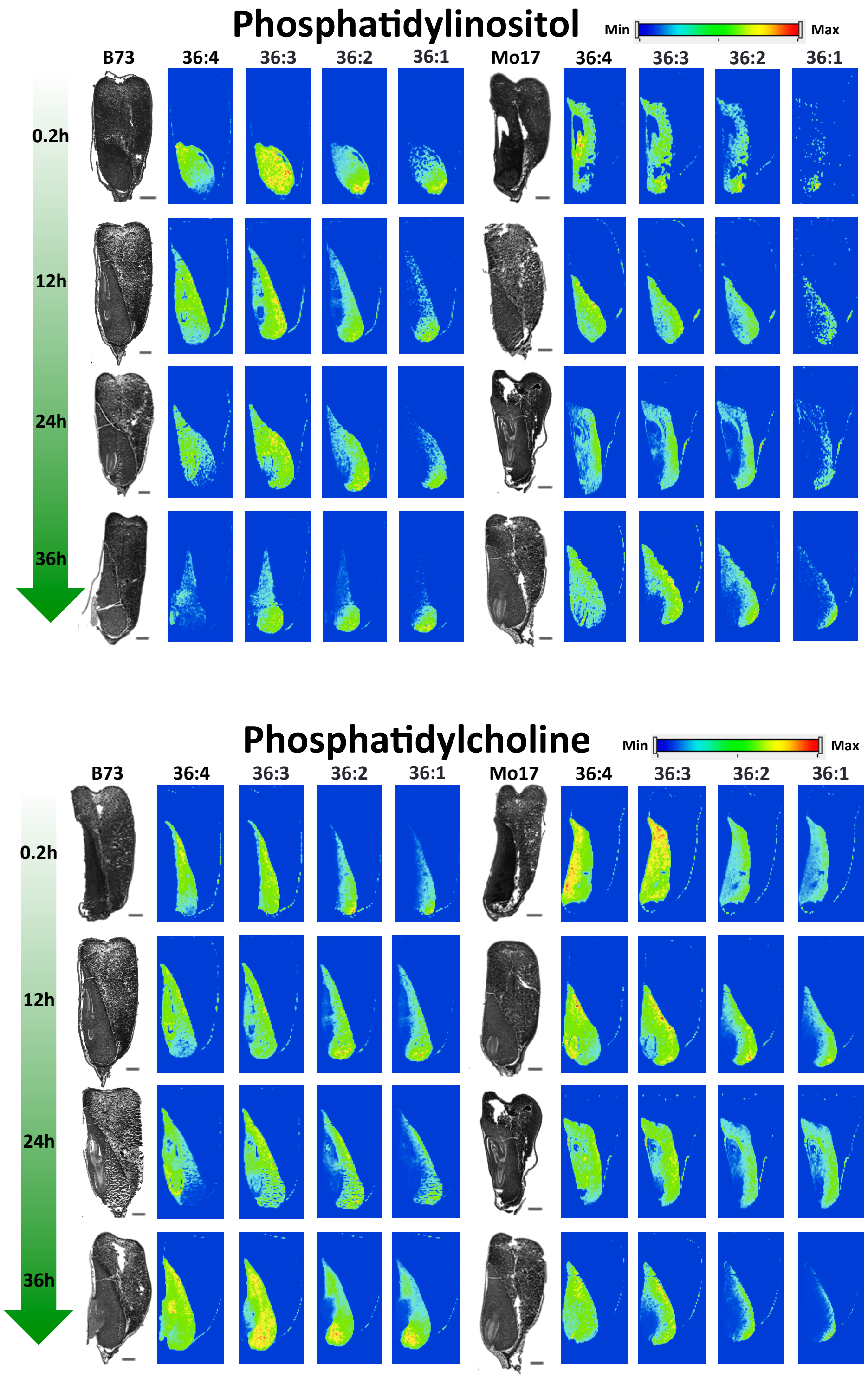

Fig. S7. Time course images for PE, PA, PI, and PC species. All imaging conditions were the same as described in Figure 7A. Scale bar: 1 mm.

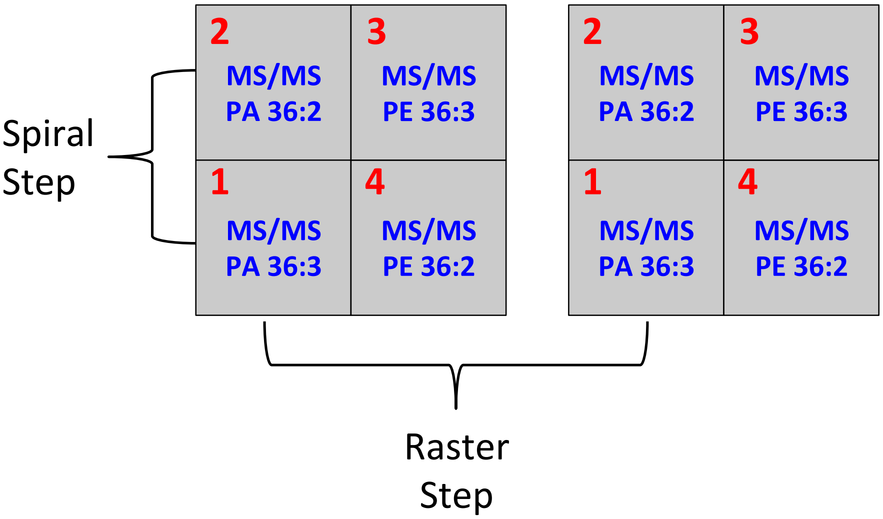

Fig. S8. Four-step imaging scheme for MS/MS of lipid species. In this setup, an individual raster step is broken up into four spiral steps, and each spiral step is assigned for MS/MS of PA 36:3, PA 36:2, PE 36:3, and PE 36:2 species, respectively.

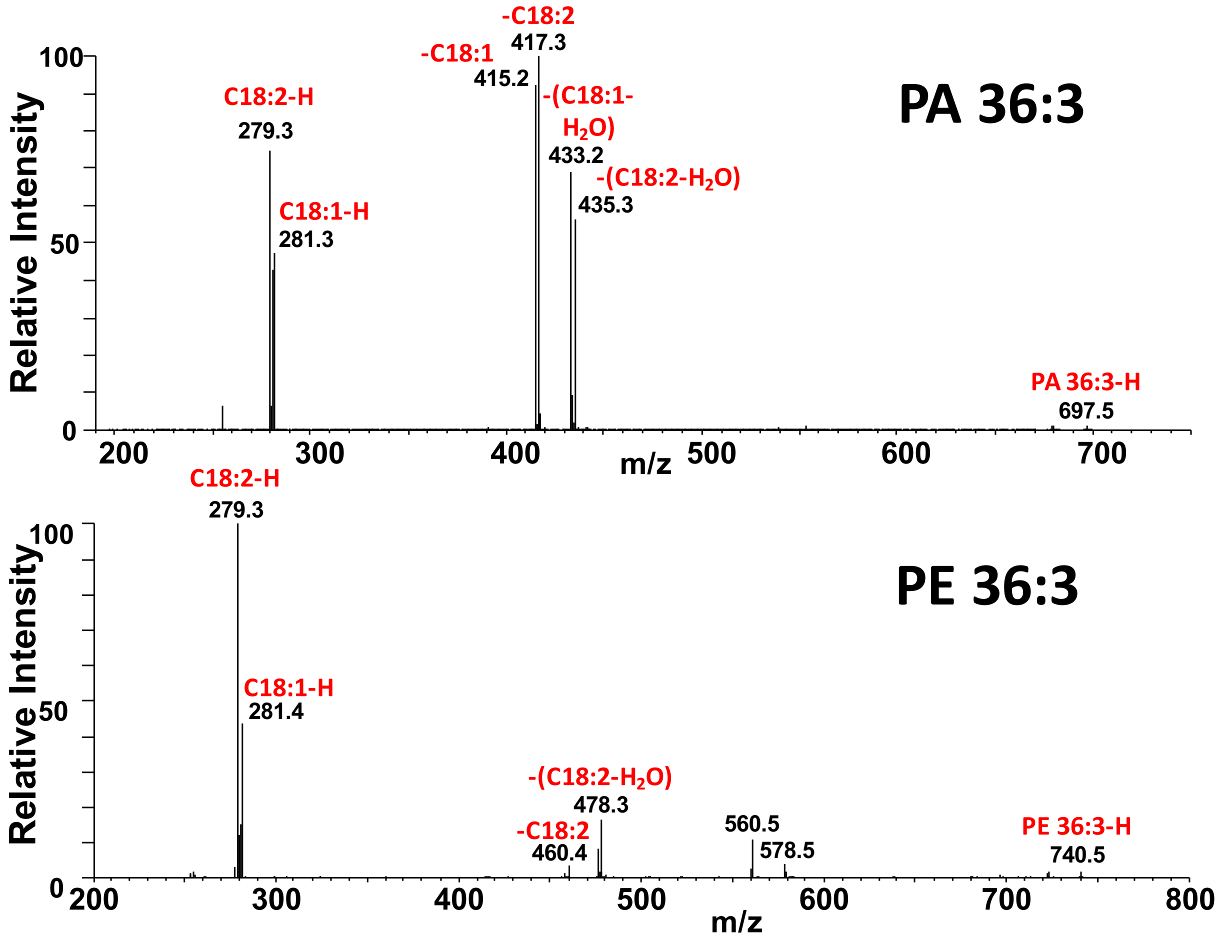

Fig. S9. MS/MS spectra of PA 36:3 and PE 36:3 obtained by averaging over the radicle area of Mo17 maize seed (24-hr post-imbibition). The spectra show that both PA 36:3 and PE 36:3 are predominantly composed of 18:1 and 18:2 fatty acid species. Spectra were acquired in negative ion mode with DAN as matrix.

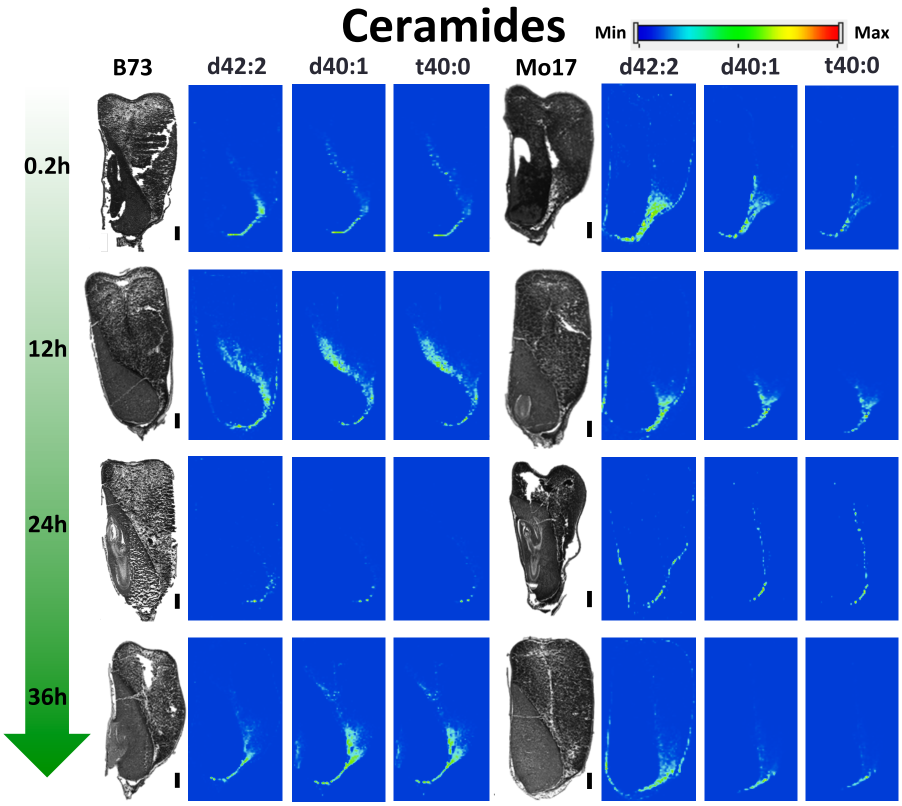

Fig. S10. MS images for the other ceramide species not shown in Figure 9. They are all detected as protonated species, $[M+H]^+$, in positive ion mode with DHB as the matrix.

Table S1. Parameters used to generate MS images, including *m/z* values, mass tolerances, and maximum and minimum scales used.

Assignment	m/z	Mass Tolerance[a]	Max (and Min) values used in image generation[b]	
			B73	Mo17
Polysaccharides				
Hex$_9$-H$_2$O+K	*m/z* 1497.438	0.088	0.2h: 1.07E5 12h: 5.03E4 24h: 5.26E4 36h: 5.19E4	0.2h: 1.14E5 12h: 5.86E4 24h: 5.99E4 36h: 4.61E4
Hex$_8$-H$_2$O+K	*m/z* 1335.38	0.079	0.2h: 1.11E5 12h: 5.86E4 24h: 5.57E4 36h: 7.92E4	0.2h: 1.21E5 12h: 7.09E4 24h: 5.88E4 36h: 4.14E4
Hex$_7$-H$_2$O+K	*m/z* 1173.333	0.062	0.2h: 9.18E4 12h: 5.40E4 24h: 6.07E4 36h: 5.18E4	0.2h: 9.91E4 12h: 5.45E4 24h: 4.53E4 36h: 4.24E4
Hex$_6$-H$_2$O+K	*m/z* 1011.280	0.048	0.2h: 1.13E5 12h: 4.23E4 24h: 5.75E4 36h: 6.43E4	0.2h: 8.14E4 12h: 6.010E4 24h: 4.36E4 36h: 3.56E4
Hex$_5$-H$_2$O+K	*m/z* 849.227	0.037	0.2h: 6.20E4 12h: 2.49E4 24h: 3.46E4 36h: 4.66E4	0.2h: 6.14E4 12h: 4.63E4 24h: 3.95E4 36h: 3.10E4
Hex$_2$+K	*m/z* 381.080	0.012	4.00E-3	
Triacylglycerols				
TAG 54:6+K	*m/z* 917.700	0.042	0.2h: 4.36E6 12h: 1.26E7 24h: 2.92E6 36h: 1.29E7	0.2h: 8.66E6 12h: 1.62E7 24h: 5.97E6 36h: 1.08E7
TAG 54:5+K	*m/z* 919.715	0.042	0.2h: 6.99E6 12h: 1.94E7 24h: 5.09E6 36h: 1.45E7	0.2h: 8.17E6 12h: 1.77E7 24h: 4.16E6 36h: 1.03E7

Table S1 (cont'd)

TAG 54:4+K	*m/z* 921.731	0.042	0.2h: 4.85E6 12h: 1.65E7 24h: 4.18E6 36h: 9.13E6	0.2h: 6.90E6 12h: 8.27E6 24h: 1.42E6 36h: 5.32E6
TAG 54:3+K	*m/z* 923.746	0.042	0.2h: 1.88E6 12h : 7.26E6 24h: 1.56E6 36h: 4.44E6	0.2h: 2.70E6 12h: 2.36E6 24h: 4.72E5 36h: 1.31E6
Amino Acids				
Lysine+H	*m/z* 147.113	0.002	0.2h: 2.698E4 12h: 2.542E4 24h: 2.941E4 36h: 4.453E4	0.2h: 2.884E4 12h: 1.452E5 24h: 6.652E4 36h: 1.907E5
Arginine+H	*m/z* 175.119	0.004	0.2h: 7.576E4 12h: 1.046E5 24h: 1.507E5 36h: 6.889E5	0.2h: 1.049E5 12h: 6.844E5 24h: 8.764E5 36h: 1.469E6
Proline+H	*m/z* 116.070	0.002	0.2h: 1.344E6 12h: 3.681E5 24h: 9.704E5 36h: 3.181E6	0.2h: 1.926E5 (3.779E4) 12h: 7.789E5 24h: 2.044E5 (3.364E4) 36h: 6.840E5
Pericarp/Aleurone Compounds				
Unknown	*m/z* 135.046	0.002	0.2h: 6.02E5 12h: 7.31E6 24h: 1.02E6 36h: 4.92E6	0.2h: 6.37E6 12h: 1.07E7 24h: 1.44E7 36h: 1.19E7
Ferulate	*m/z* 193.051	0.004	0.2h: 9.11E5 12h: 4.04E6 24h: 1.47E6 36h: 3.88E6	0.2h: 4.54E6 12h: 7.45E6 24h: 6.44E6 36h: 7.73E6
Unknown	*m/z* 161.025	0.003	0.2h: 1.78E5 12h: 2.09E6 24h: 2.94E5 36h: 8.72E5	0.2h: 2.72E6 12h: 5.88E6 24h: 7.88E6 36h: 3.43E6

Table S1 (cont'd)

Combination Image Fig. 4B & C				
Malic Acid	*m/z* 133.015	0.002	4.577E2	
PI 34:2	*m/z* 833.521	0.036	2.586E2	
Ferulic Acid	*m/z* 193.051	0.004	3.751E2	
Energy Related Metabolites				
Hexose phosphate - H_2O-H	*m/z* 241.012	0.005	9.00E-3	
Glycerol phosphate - H_2O-H	*m/z* 152.996	0.003	1.50E-2	
Citrate/Isocitrate-H	*m/z* 191.020	0.004	1.00E-3	
Fatty Acids				
Palmitate (16:0)-H	*m/z* 255.233	0.005	8.00E-2	
Linoleate (18:2)-H	*m/z* 279.233	0.005	1.00E-1	
Oleate (18:1)-H	*m/z* 281.249	0.005	8.00E-2	
Stearate (18:0)-H	*m/z* 283.264	0.005	6.00E-3	
Phospholipids				
PE 36:4-H	*m/z* 738.508	0.030	0.2h: 6.60E5 12h: 4.03E6 24h: 7.67E5 36h (Supp): 2.82E6 36h (Main): 3.99E6	0.2h: 1.95E6 12h: 2.07E6 24h: 2.16E6 36h (Supp): 2.85E6 36h (Main): 2.85E6
PE 36:3-H	*m/z* 740.524	0.030	0.2h: 4.87E5 12h: 2.410E6 24h: 4.59E5 36h (Supp): 1.52E6 36h (Main): 2.45E6	0.2h: 1.76E6 12h: 1.41E6 24h: 9.51E5 36h (Supp): 1.49E6 36h (Main): 1.49E6
PE 36:2-H	*m/z* 742.539	0.030	0.2h: 9.89E5 12h: 5.06E6 24h: 1.21E6 36h (Supp): 3.62E6 36h (Main): 4.14E6	0.2h: 3.69E6 12h: 4.45E6 24h: 2.67E6 36h (Supp): 5.71E6 36h (Main): 5.71E6

Table S1 (cont'd)

PE 36:1-H	*m/z* 744.555	0.030	0.2h: 4.75E5 12h: 1.83E6 24h: 5.83E5 36h (Supp): 1.37E6 36h (Main): 1.89E6	0.2h: 1.10E6 12h: 1.62E6 24h: 8.93E5 36h (Supp): 1.94E6 36h (Main): 1.94E6
PA 36:4-H	*m/z* 695.465	0.028	0.2h: 5.97E5 12h: 4.29E6 24h: 1.35E6 36h (Supp): 3.34E6 36h (Main): 1.25E7	0.2h: 2.62E6 12h: 4.42E6 24h: 4.85E6 36h (Supp): 6.80E6 36h (Main): 6.80E6
PA 36:3-H	*m/z* 697.481	0.028	0.2h: 8.56E5 12h: 5.70E6 24h: 1.08E6 36h (Supp): 4.18E6 36h (Main): 6.43E6	0.2h: 3.06E6 12h: 4.86E6 24h M: 5.71E6 36h (Supp): 5.15E6 36h (Main): 5.15E6
PA 36:2-H	*m/z* 699.497	0.028	0.2h: 6.51E5 12h: 3.67E6 24h: 8.34E5 36h (Supp): 2.04E6 36h (Main): 6.278E6	0.2h: 1.98E6 12h: 1.92E6 24h: 2.34E6 36h (Supp): 2.75E6 36h (Main): 2.75E6
PA 36:1-H	*m/z* 701.513	0.028	0.2h: 9.49E4 12h: 3.41E5 24h: 1.10E5 36h (Supp): 2.95E5 36h (Main): 5.46E5	0.2h: 2.85E5 12h: 2.91E5 24h: 2.79E5 36h (Supp): 4.87E5 36h (Main): 4.87E5
PI 36:4-H	*m/z* 857.519	0.039	0.2h: 2.77E5 12h: 7.75E5 24h: 1.48E5 36h (Supp): 1.18E6 36h (Main): 1.18E6	0.2h: 6.36E5 12h: 8.24E5 24h: 1.16E6 36h (Supp): 5.50E5 36h (Main): 5.50E5
PI 36:3-H	*m/z* 859.534	0.039	0.2h: 3.96E5 12h: 1.22E6 24h: 2.22E5 36h (Supp): 9.98E5 36h (Main): 9.98E5	0.2h: 7.59E5 12h: 1.06E6 24h: 1.28E6 36h (Supp): 6.30E5 36h (Main): 6.30E5

Table S1 (cont'd)

PI 36:2-H	*m/z* 861.550	0.039	0.2h: 6.09E5 12h: 1.43E6 24h: 3.39E5 36h (Supp): 1.86E6 36h (Main): 1.86E6	0.2h: 6.62E5 12h: 1.03E6 24h: 1.01E6 36h (Supp): 1.27E6 36h (Main): 1.27E6
PI 36:1-H	*m/z* 863.566	0.039	0.2h: 1.27E5 12h: 4.18E5 24h: 1.93E5 36h (Supp): 6.88E5 36h (Main): 6.88E5	0.2h: 1.74E5 12h: 2.53E5 24h: 3.75E5 36h (Supp): 6.33E5 36h (Main): 6.33E5
PC 36:4+K	*m/z* 820.525	0.036	0.2h: 2.15E7 12h: 2.29E7 24h: 2.36E7 36h (Supp): 3.77E7 36h (Main): 3.22E7	0.2h: 2.52E7 12h: 3.17E7 24h: 1.22E7 36h (Supp): 3.37E7 36h (Main): 3.37E7
PC 36:3+K	*m/z* 822.541	0.036	0.2h: 2.85E7 12h: 3.68E7 24h: 2.63E7 36h (Supp): 3.31E7 36h (Main): 2.48E7	0.2h: 2.83E7 12h: 3.60E7 24h: 1.11E7 36h (Supp): 2.47E7 36h (Main): 2.47E7
PC 36:2+K	*m/z* 824.557	0.036	0.2h: 2.43E7 12h: 2.10E7 24h: 2.47E7 36h (Supp): 1.80E7 36h (Main): 2.49E7	0.2h: 2.69E7 12h: 2.37E7 24h: 5.23E6 36h (Supp): 1.68E7 36h (Main): 1.68E7
PC 36:1+K	*m/z* 826.572	0.036	0.2h: 3.55E6 12h: 2.57E6 24h: 5.21E6 36h (Supp): 1.96E6 36h (Main): 4.25E6	0.2h: 3.94E6 12h: 3.48E6 24h: 5.78E5 36h (Supp): 4.39E6 36h (Main): 4.39E6
PC 34:2+K	*m/z* 796.527	0.035	2.267E7	
Ceramides				
Cer d40:1+H	*m/z* 622.614	0.023	0.2h: 9.29E5 12h: 6.83E5 24h: 6.23E5 36h: 5.68E5	0.2h: 6.83E5 12h: 8.12E5 24h: 1.67E5 36h: 1.39E6

Table S1 (cont’d)

Cer t40:0+H	*m/z* 640.625	0.024	0.2h: 8.46E5 12h: 5.89E5 24h: 5.71E5 36h: 5.59E5	0.2h: 6.69E5 12h: 7.17E5 24h: 1.39E5 36h: 1.37E6
Cer d42:1+H	*m/z* 650.645	0.026	0.2h: 1.21E6 12h: 1.22E6 24h: 3.78E5 36h: 1.57E6	0.2h: 6.77E5 12h: 1.03E6 24h: 2.85E5 36h: 1.24E6
Cer d42:2+H	*m/z* 664.625	0.027	0.2h: 5.53E5 12h: 3.96E5 24h: 2.51E5 36h: 8.24E5	0.2h: 3.02E5 12h: 6.08E5 24h: 1.91E5 36h: 6.25E5
Cer t42:0+H	*m/z* 668.655	0.027	0.2h: 1.34E6 12h: 9.78E5 24h: 3.39E5 36h: 1.46E6	0.2h: 4.66E5 12h: 7.19E5 24h: 2.74E5 36h: 7.61E5
Supplementary Figure 5A				
Malic Acid	*m/z* 133.015	0.002	1.00E-2	
Supplemental Figure 5C				
Malic Acid	*m/z* 133.015	0.002	1.00E-2	

a: Mass tolerance is selected considering the mass resolution at a given mass.

b: MS images are generated by normalizing to total ion count (TIC) for disaccharides, hexose phosphate, glycerol phosphate, citrate/isocitrate, and malic acid at each pixel. In such case, the same maximum scale is used for all the images regardless of genotype or germination time point. For non-normalized images, maximum color scale is arbitrarily adjusted for each image to obtain the best contrast displaying localization. Minimum value is set to zero for the compounds normalized to TIC and one for non-normalized images. When higher minimum values are used to avoid background noise, it was shown in the parenthesis.

Tables S2, S3, S4: Available online on the PMR database.

CHAPTER 3

MULTI-MATRIX, DUAL POLARITY, TANDEM MASS SPECTROMETRY IMAGING STRATEGY APPLIED TO A GERMINATED MAIZE SEED: TOWARD MASS SPECTROMETRY IMAGING OF AN UNTARGETED METABOLOME

A paper published in *Analyst*

Analyst, 2015, **140**, 7293-7304

Reproduced with permission of The Royal Society of Chemistry.

Adam D. Feenstra, Rebecca L. Hansen, and Young Jin Lee

Abstract

Mass spectrometry imaging (MSI) provides high spatial resolution information that is unprecedented in traditional metabolomics analyses; however, the molecular coverage is often limited to a handful of compounds and is insufficient to understand overall metabolomic changes of a biological system. Here, we propose an MSI methodology to increase the diversity of chemical compounds that can be imaged and identified, in order to eventually perform untargeted metabolomic analysis using MSI. In this approach, we use the desorption/ionization bias of various matrixes for different metabolite classes along with dual polarities and a tandem MSI strategy. The use of multiple matrixes and dual polarities allows us to visualize various classes of compounds, while data-dependent MS/MS spectra acquired in the same MSI scans allow us to identify the compounds directly on the tissue. In a proof of concept application to a germinated corn seed, a total of 166 unique ions were determined to have high-quality MS/MS spectra, without counting structural isomers, of which 52 were identified as unique compounds. According to an estimation based on precursor MSI datasets, we expect over five hundred metabolites could be potentially identified and visualized once all experimental conditions are

optimized and an MS/MS library is available. Lastly, metabolites involved in the glycolysis pathway and tricarboxylic acid cycle were imaged to demonstrate the potential of this technology to better understand metabolic biology.

Introduction

Since its development nearly two decades ago, molecular mass spectrometry imaging (MSI) has become a useful and increasingly common tool for tissue analysis.[1,2] Several desorption/ ionization techniques have been adopted for MSI, but by far matrix-assisted laser desorption/ionization (MALDI)-MSI has been most widely used.[3–6] Applications demonstrated thus far include imaging various classes of compounds such as lipids, peptides, proteins, drugs, and small molecules in tissue samples as diverse as animal organs, plant tissues, and bacterial colonies. The benefit of MSI is that it combines the versatility and high specificity of mass spectrometry with high spatial resolution localization information. While MSI cannot reach the spatial resolution of optical imaging techniques, it provides valuable chemical information and the ability to simultaneously image hundreds of chemical compounds in one sample.

MALDI-MSI is often used for targeted imaging of a specific compound or class of compounds (e.g., drugs or drug metabolites[7]); however, its application for complex biological phenomena (e.g., nitrogen fixation[8]) is relatively limited. The lack of such “discovery” type experiments originates from (1) the limited number of compounds that can be characterized with a particular matrix and (2) the difficulty in confidently identifying metabolites directly on tissue. Most discovery type experiments in metabolomics studies, so called ‘untargeted metabolomics’, are being performed with traditional gas chromatography-electron ionization-mass spectrometry (GC-EI-MS) or liquid chromatography-tandem mass spectrometry (LC-MS/MS) experiments, which require sample homogenization, resulting in the loss of spatial localization information of metabolites.

Untargeted metabolomic profiling is limited even in traditional analyses by the difficulty of confidently identifying metabolites due to the lack of EI-MS or MS/MS databases. This issue is especially significant in plant metabolomic analysis because over 200 000 metabolites are expected to be present in the plant kingdom and most of them are unknown.[9,10] For example, the NIST EI-MS library has over 200 000 entries, but most of them are from man-made synthetic compounds or abundant natural products. In typical untargeted GC-MS profiling of a plant metabolome, one-half to two-thirds of the metabolites cannot be confidently identified.[11–13] Unknown compound identification in LC-MS/MS is even more difficult, as its database is much smaller.

Recently there have been some efforts to build widely applicable metabolite MS/MS databases. The Suizdak group has accumulated MS/MS spectra of 12 834 metabolites (as of May 11, 2015) in their Metlin database (metlin.scripps.edu), but that number is only about 5% of the number of known metabolites they list (240 588), not to speak of unknown metabolites. Another difficulty arises from the fact that MS/MS spectral patterns strongly depend on the instrument type and collision energy used. Many of the current MS/MS databases, such as Metlin, are being constructed for a quadrupole time-of-flight mass spectrometer (Q-TOF) and may not be as useful for other instruments, such as an ion trap.

We have previously developed an MSI strategy[14] in which each raster step is split into multiple spiral steps composed of a precursor MS scan followed by several MS/MS or

MSn scans, which we called 'multiplex MSI'. We also demonstrated that a wider variety of lipid classes could be visualized by incorporating polarity switching into multiplex MSI.[15] In this work, we attempt to expand the multiplex MSI approach to a large metabolomics scale by using the inherent bias of matrixes for desorbing/ionizing different classes of compounds to analyze as wide of a range of compounds as possible. Following accurate mass precursor scans, data-dependent MS/MS spectral acquisition is performed so that we can obtain hundreds or thousands of MS/MS spectra directly on tissue. To overcome the lack of chromatographic separation in MSI, we propose to use multiple serial tissue sections and selectively ionize various metabolite classes by utilizing different matrixes and polarities. By improving the two bottlenecks in MSI, the number of compounds that can be visualized and the confidence in their identifications, we propose MSI of an untargeted metabolome is possible.

In the present study, we demonstrate this strategy as applied to a germinated maize seed. Seed germination is a critical stage in the life cycle of a plant when very active metabolic changes occur to break down storage starch and proteins and convert them to developing tissues and organs.[16] Various metabolic pathways are turned on at specialized locations, making it an ideal system to demonstrate the proposed MSI strategy.

Experimental

Materials

Organic matrixes were purchased from Sigma-Aldrich (St. Louis, MO, USA): 1,5-diaminonaphthalene (DAN, 97%), 2,5-dihydroxybenzoic acid (DHB, 98%), and 9-aminoacridine (9AA, 98%) hydrochloride hydrate. 9AA was converted to the free base form upon arrival and before use by dissolving in boiling water and adding an equimolar amount of sodium hydroxide. The precipitate was then filtered, washed three times with cold water, and dried. Iron oxide nanoparticles (NPs) (Fe_3O_4, 11 nm, no organic capping) were synthesized and provided by Dr Javier Vela's research group at Iowa State University.[17] Tungsten oxide (WO_3, 23–65 nm, no organic capping) and silver (20 nm, no organic capping) NPs were obtained from US Research Nanomaterials, Inc. (Houston, TX, USA) and suspended in 2-propanol (Sigma Aldrich, LC-MS Chromasolv) upon arrival. Gelatin from porcine skin (300 bloom) was purchased from Electron Microscopy Sciences (Hatfield, PA, USA). B73 inbreed corn seeds were obtained from Dr Marna Yandeau-Nelson at Iowa State University.

Corn seed growth

A B73 inbreed corn seed was imbibed by placing it in a glass scintillation vial with deionized water and shaking the vial at 300 rpm for 10 minutes. The seed was then placed on a moist piece of filter paper in a plastic petri dish with the embryo side of the corn seed down. The petri dish was covered with a transparent, plastic lid and placed in a climate-controlled greenhouse (27 °C at day time, 24 °C at night time, 15 hours of day light each day) to grow. The seed was allowed to germinate for 29 hours with water periodically added to keep the filter paper moist but without standing water.

After 29 hours, the seed was removed from the greenhouse. Using a razor blade, the seed was cut longitudinally approximately halfway between the edge and center. Immediately after cutting, the seed was flash-frozen in liquid nitrogen to prevent metabolite turnover. Once the seed was frozen, it was stored at −80 °C until cryosectioning and transported on dry ice to prevent thawing.

Sample preparation for imaging

Sample preparation procedure for MSI of plant tissues is described in detail in our recent protocol paper[18] and is briefly described below. The procedure consists of cryosectioning, drying, and matrix application. For cryosectioning, the frozen seed was placed in a cryo-mold with the flat, cut face down. A warm, aqueous, 10% w/v gelatin solution was poured into the mold to completely cover the seed. The mold was immediately floated on liquid nitrogen until the gelatin in the mold had become mostly opaque, then transferred to a cryostat prechilled to −22 °C. Once the gelatin medium was completely frozen and thermally equilibrated (~30 min), the block was mounted onto the cryostat chuck and sections of the region of interest were cut at 10 μm thickness and captured intact using adhesive tape windows (Leica Biosystems, Buffalo Grove, IL, USA). The tape windows with tissue sections were taped faceup onto chilled glass slides to prevent thawing, then transported on dry ice and stored at −80 °C until further processing.

Adjacent serial tissue sections were selected for imaging. The slides with the attached seed sections were placed onto a chilled aluminum block, and then lyophilized under moderate vacuum (~250 mtorr) while slowly equilibrating to room temperature.

Matrix was then either applied by sublimation-vapor deposition as previously described (for DHB),[19] or by a homemade oscillating capillary nebulizer (for 9AA, DAN, Fe_3O_4 NPs, WO_3 NPs, Ag NPs).[20] The matrix-coated tissue section on the tape window was transferred to a stainless steel slide, which was put into the MALDI plate holder and inserted into the mass spectrometer.

MALDI mass spectrometry imaging

Optical images of each tissue were obtained by scanning and combining camera shots in the instrument (image resolution of ~6 μm per pixel). Imaging data was acquired using a MALDI-linear ion trap (LIT)-Orbitrap mass spectrometer (MALDI-LTQ-Orbitrap Discovery; Thermo Finnigan, San Jose, CA) that has been modified to incorporate an external Nd:YAG laser (UVFQ; Elforlight, Ltd, Daventry, UK). Laser pulse energy and number of shots were optimized individually for each matrix.

A multiplex MSI strategy was adopted for data acquisition using a four spiral step pattern for each pixel (see Fig. 1) with a 100 μm raster step (pixel) size and 50 μm spiral step size. The laser spot size is 25 μm as estimated from the burn mark on thin film of DHB. In the first scan event, a full Orbitrap mass spectrum was acquired for *m/z* 50–800 with a mass resolution of 30 000 at *m/z* 400. Next, a data-dependent ion trap MS/MS scan was performed from the previous scan. In the third scan event, another full Orbitrap scan was acquired for *m/z* 600–1600, followed by another data-dependent ion trap MS/MS scan from the third scan event.

To ensure MS/MS would be performed for known metabolite compounds, two separate precursor mass lists (136 masses in positive mode, 93 in negative mode) consisting of previously observed metabolites were imported to the Excalibur data acquisition program (Thermo) for positive and negative ion mode. It should be noted that MS/MS have not been previously obtained for many of these compounds, and certainly not directly on maize embryos. Collision energies were broadly assigned depending on the precursor mass range for optimal fragmentations (m/z 50–300, 125%; m/z 300–600, 75%; above m/z 600, 35%). If no ion was found among the precursor masses within a 0.05 Da mass tolerance, the instrument was set up to perform MS/MS of the most abundant ion with a default setting of 35% collision energy. Collision duration was 30 ms in all cases. Dynamic exclusion was also adopted to obtain as many useful MS/MS scans as possible using a repeat count of one and an exclusion duration of 50 seconds.

All the images shown in this manuscript were generated using ImageQuest (Thermo) with a ±0.01 Da mass tolerance and in absolute ion intensity scale without any normalization. Normalization with total ion count was also performed but displayed almost no difference.

MS/MS data analysis

Manual interpretation was performed for high quality MS/MS spectra. To reduce the number of MS/MS spectra for manual interpretation, we performed three levels of filtering to extract only those MS/MS spectra that are most likely to be meaningful. The first filtering was performed at the MS/MS level. All MS/MS spectra were extracted from each raw data file as separate ascii files using ExtractMSN.exe (Thermo). Filtering parameters were optimized by trial and error and imposed on these ascii files in order to minimize the loss of MS/MS spectra from real metabolites while removing most of the MS/ MS from contaminants. This procedure removed most of the low quality MS/MS spectra. The following filtering parameters were used for the MS/MS data sets. For negative mode, compounds with m/z 100–300 were filtered with a total ion count (TIC) threshold of 50 and a minimum of 2 fragment ions, whereas compounds of *m/z* 300–1600 were filtered with a TIC threshold of 75 and a minimum of 3 fragment ions. For positive mode, compounds with *m/z* 100–400 were filtered with a TIC threshold of 50 and a minimum of 2 fragment ions while compounds of *m/z* 400–1600 were filtered with a TIC threshold of 1000 and a minimum of 10 fragment ions. In the precursor mass list that passed the above MS/MS filtering, we ignored structural isomers and combined all the same precursor masses by treating all masses within ±0.01 Da as if they were the same compound.

The second filtering was at the precursor MS spectral level. Precursor mass spectra were averaged over the entire sample and low intensity precursor ions were removed if their ion abundance was below 0.1% of the base peaks. Then, 13 carbon isotopes were removed from the remaining precursor masses with the mass difference of 1.00335 Da (i.e., mass difference of ^{13}C–^{12}C).

The final filtering was at the MS image level. The precursor mass list that passed both MS/MS and MS level filtering above was subjected to image inspection and the ions from the non-tissue area were removed. The images were generated in ImageQuest with a ±0.01 Da mass tolerance and manually inspected to determine if the signal was localized only on the tissue. This left a final mass list composed of high-abundance, potentially identifiable metabolite ions.

All MS/MS spectra that passed through the above filtering were then subjected to manual interpretation. Based on the image localization of each precursor mass, MS/MS spectra were averaged where signal was present using QualBrowser (Thermo). The averaged MS/MS were interpreted in a multistep process. First, the accurate precursor mass was searched against metabolite, lipid, or chemical databases (Metlin, LipidMaps (http://www.lipidmaps.org), Chemspider (http://www. chemspider.com)) with a mass tolerance of 5 ppm. If a matching compound was found, Metlin and MassBank (http://www. massbank.jp) were checked for the presence of MS/MS spectra for comparison. If a compound had at least two major fragments matching and no unusual fragments, the assignment was presumed to be correct. If no MS/MS was available for comparison, manual MS/MS spectral interpretation was attempted to explain the possible fragmentation of matching precursor compounds.

Estimation of potential metabolites based on accurate mass

The total number of identifiable metabolites was estimated from the precursor mass spectra based solely on accurate mass. MSiReader[21] was used for automatic MS image generation for both low and high mass scans of the Orbitrap spectra. The Peak Finder tool in MSiReader was used to select the entire tissue sample and generate a peak list for the masses found only on tissue. The parameters used in the Peak Finder tool were a minimum of 0.1% presence in the interrogated zone and a maximum presence of 5% (or maximum S/N of two) in the reference zone.

After the peak list was generated, the Batch Processing feature of MSiReader was used to automatically generate images for all the masses with ±0.005 Da mass tolerance (none of these images are used in the text; rather, this served as a quick and efficient way of determining if peaks were localized on tissue). Any peaks whose images showed localization anywhere off the tissue area were removed. Images that were indeterminate were also generated in ImageQuest to check their localization. For masses that were separated by less than 0.02 Da, their images were compared to see if they showed different localizations. For masses with the same localization, the precursor mass spectrum was carefully inspected for the image area to determine if multiple masses were actually present. If not, the mass of the only peak in the spectrum for that area was used.

After image filtering, ^{13}C isotope peaks were manually removed from this mass list in both positive and negative modes. Additionally, potential multiple alkali metal adducts (+Na, +K) were removed in positive mode data while potential water loss peaks were removed in negative mode data. All removals were based on being within 5 ppm of the suspected mass values. This left a final peak list localized only on the tissue area that are considered as potentially identifiable metabolites. This mass list was searched against the Metlin metabolite database for possible matches within 5 ppm.

Results and discussion

Comparison of different classes of compounds between matrixes

A corn seed was germinated for 29 hours and then serial sections of the seed were subjected to MALDI-MSI analysis with a different matrix applied to each section. To demonstrate selectivity of each matrix in characterizing specific compounds of interest, representative compounds detected in three matrixes in negative ion mode are compared in Fig. 2. Detailed anatomy of a maize seed is shown in ESI Fig. 1.†

There is no perfect way to compare images between different matrixes due to multiple variables. The best method we found is to individually optimize each matrix, especially matrix application and laser energy, and compare ion signal levels obtained at each optimum condition. We minimized other variables as much as possible, such as use of serial sections to minimize biological variations and acquiring data next to each other on the same day to minimize analytical variations. We have found the results were fairly reproducible in this approach. The images shown in Fig. 2 were produced in absolute ion intensity scale, without any normalization. The intensity scale is adjusted for each analyte that can best visualize the image contrast. Normalization to the total ion count (TIC) is often adopted to minimize spot-to-spot variation; however, it may not the best method for the current purpose because it can exaggerate relative ion signals for a matrix that gives low ion signals. We also compared the images with TIC normalization as shown in ESI Fig. 2,† which gave virtually the same results.

The selected compounds show a better desorption ionization efficiency for one matrix compared to the others, as can be observed through the quality of images generated. DAN, for example, shows high quality images for the acidic phospholipids and small molecule classes (shown in the top set of images). Previously, Chaurand has shown DAN to be effective for lipids in negative mode[22] and here we observe similar results. Phosphatidylethanolamine (PE) 34:2 and phosphatidic acid (PA) 36:4 are both localized in the developing embryo and radicle tissue (initial root of the seed) in the images obtained with DAN, while 9AA and Ag NPs have almost no signal present. Other lipids, such as phosphatidylinositol (PI) and phosphatidylglycerol (PG) (not shown), also show much better signal with DAN compared to the other matrixes. DAN is also effective for small molecules such as glutamine, which appears in the radicle of the seed, and malic acid, which is present in the radicle and endosperm (starchy storage reserves of the seed). This is consistent with our recent report that DAN is a good matrix for small molecules in negative ion mode.[23]

9AA is well known for its effectiveness for small molecules in negative mode.[24,25] As shown in Fig. 2, it is comparable with DAN for some organic acids, such as malic acid, but inefficient for some other molecules, such as glutamine.[23] However, 9AA shows much better ionization efficiency for nucleotide type compounds, as has been previously demonstrated.[26] Examples shown here include uridine monophosphate (UMP), adenosine diphosphate (ADP), and uridine diphosphate glucose (UDP-Glc), all distributed throughout the radicle and embryo of the seed. DAN and Ag NPs show no signal for this class of compounds however.

Silver nanoparticles were selected as one of the matrixes in this study because they are known to be effective for fatty acids and phospholipids.[27,28] However, at least for the current tissue sample of a germinated maize seed, they were not as efficient for phospholipids as DAN. Fatty acids could be successfully visualized with silver nanoparticles, but DAN produced much better images (not shown). Ag NPs showed better selectivity for some small molecules, such as phosphonoacetaldehyde (PALD), and for two unidentified peaks (likely small, organic acid type compounds) at *m/z* 143.035 and 113.024. PALD and *m/z* 143.035 were also detected with DAN, but with much lower signals. PALD is evenly distributed throughout the embryo of the seed while *m/z* 143.035 and 113.024 species are distributed throughout the endosperm area of the seed.

Similar results were obtained in positive mode as demonstrated with nine representative compounds in Fig. 3. DHB, tungsten oxide NPs, and iron oxide NPs show different desorption ionization efficiency behavior for various classes of compounds, although there was some similarity between the two metal oxide nanoparticles. DHB is well known to have good efficiency for a relatively wide variety of compounds, especially for large molecules including lipids, proteins, and oligosaccharides.[22,29–31] Neutral or cationic lipids, such as ceramide 42:1 and phosphatidylcholine (PC) 34:2, are efficiently detected with DHB, along with large oligosaccharides and an unidentified compound at *m/z* 972.521. The sphingolipid ceramide is very uniquely localized on the boundary area between the embryo and endosperm part of the seed. PC 34:2 and the compound at *m/z* 972.521 are seen primarily in the radicle of the seed with some distribution throughout the rest of the embryo. Large oligosaccharides, such as heptahexose, are localized in the endosperm area. Neither of the NPs shows any signal for these classes of compounds.

Iron oxide and tungsten oxide NPs show significant differences with DHB, but share some similarity between themselves. Both are able to effectively ionize small sugars (e.g., monohexose and dihexose, most likely glucose and sucrose) and triacylglycerols (TG) much better than DHB. For instance, in the case of dihexose, iron oxide and tungsten oxide NPs have about fifteen times and five times higher ion signals than DHB, respectively. Overall, iron oxide NPs are slightly better than tungsten oxide NPs, except for certain compounds such as proline.

It is interesting to note that large oligosaccharides (e.g., Hex_7; the same for Hex_3 to Hex_9, images not shown) are localized in the endosperm area whereas small oligosaccharides (i.e., Hex, Hex_2) are localized in the embryo area. This suggests that starch is broken down in the endosperm and then small sugars are transported to the embryo. Most importantly, the use of multiple matrixes could effectively visualize the localization of both small and large sugars.

All together, the results above suggest that a wide range of compounds can be characterized by combining several different matrixes in positive and negative mode.

In negative mode, we are able to detect acidic phospholipids such as PE and PA, amino acids, nucleotides, nucleotide sugars, organic acids and other small molecules. Positive mode presents neutral or cationic phospholipids, amino acids, sugars, and non-acidic small molecules.

MS/MS based metabolite identification

The previous section demonstrated that the combined use of various matrixes in dual polarities is a good strategy to increase the chemical coverage in MALDI-MSI. The other major obstacle to overcome for MSI in metabolomics scale is confident identification of compounds. In-parallel metabolomics analysis by traditional GC- or LC-MS methods is expected to assist metabolite identifications in MSI data; however, it is still necessary to identify metabolites on tissue because there may be several structural isomers with different tissue localizations or possible alterations of metabolites during sample preparation.

As detailed in the Experimental section, the six data sets shown in Fig. 2 and 3 were acquired using a multiplex MSI strategy. Fig. 1 summarized the overall data acquisition scheme. Two precursor MS scans in low and high mass range (*m/z* 50–800 and *m/z* 600–1600, respectively) were acquired in Orbitrap, followed by data-dependent MS/MS scans in ion trap. We envision high-throughput MS/MS database searches would be possible for thousands of MS/MS spectra acquired through this multiplex MSI. Currently, however, we encounter several obstacles, most notably the lack of an MS/MS database. Our MS/MS data was acquired in an ion trap mass spectrometer, and publicly available ion trap MS/MS databases are very limited. MassBank has some ion trap MS/MS spectra, but the total number is not any more than a few hundred compounds. Hence, in this proof-of-concept study, we performed manual evaluation of each MS/MS spectra for possible identification.

The total number of MS/MS spectra from the six multiplex MSI data sets, three positive and three negative, is 92 248. Many of them are from the same precursor masses, in spite of data-dependent acquisitions, but there are still a large amount of unique MS/MS spectra from different compounds. To minimize the workload in manually interpreting all the MS/MS spectra, we first filtered out low quality MS/MS spectra that were expected to be structurally uninformative. Then, to further minimize the manual labor, we ignored structural isomers and combined MS/MS spectra from the same precursor mass by averaging these spectra together. Additionally, low abundance ions in the precursor MS spectra and ^{13}C isotope ions were removed as well as ions present outside the tissue area. After this filtering, detailed in the Experimental section, we obtained a total of 104 unique ions with high quality MS/ MS spectra in positive mode and 62 in negative mode, as listed in ESI Tables 1 and 2† and summarized in Fig. 4A. A few ions were obtained in all three matrixes, 13 and 4, for positive and negative mode, respectively; however, the majority were obtained only in one matrix and some in two matrixes, as expected from Fig. 2 and 3.

Manual interpretation was performed for the 166 MS/MS datasets, as described in the Experimental section, based on accurate precursor mass and MS/MS spectra. When MS/MS spectra were available on Metlin or MassBank, careful comparison was made while considering the differences in MS/MS spectral patterns between QTOF and ion trap. Namely, our MS/ MS spectra were acquired in an ion trap, which is known to have a low mass cutoff, losing the fragment ion signals below 28% of the precursor *m/z* values.[32] Meanwhile, QTOF fragmentation often produces significant low mass fragments due to multiple fragmentations. Accordingly, we mostly compared fragments in higher mass ranges and ignored the difference in fragment ion intensities. If MS/MS spectra were not available or did not match with the queried experimental spectra, metabolites matching the precursor mass either in Metlin, LipidMaps or ChemSpider were subjected to manual interpretations to attempt to match experimental fragment spectra with expected fragment structures.

After manual interpretation of the 166 MS/MS spectra, a total of 41 and 25 spectra were tentatively identified in positive and negative mode, respectively, as summarized in ESI Tables 3 and 4.† Out of those, 27 were determined to be unique compounds in positive mode (multiple cation adducts and identifiable fragments such as PC trimethylamine losses were counted as the same species), and all 25 were unique in negative mode. These results are summarized in Fig. 4B as Venn diagrams.

We were tentatively able to identify only ~40% of the ions in each polarity among the potentially identifiable MS/MS spectra, largely due to the lack of an MS/MS database. MS/MS spectra common in all three matrixes were mostly identified, with 12 out of 13 in positive mode and 3 out of 4 in negative mode. However, MS/MS spectra detected in only one matrix had a much lower success rate; e.g., only 1 out 12 and 12 out of 46 identified in WO_3 and Fe_3O_4, respectively. This is likely due to the fact that the metabolites found in all three matrixes are present in high abundance, thus giving multiple sets of high-quality MS/MS spectra. In contrast, those found in only one matrix might be present in low abundance and/or with weak MS/MS signals. In other words, some high-abundance compounds could be detected regardless of matrix, although ion signals could be low in some matrixes, and thus have a good chance to be identified. Hence, it is especially for low abundance metabolites that we need to carefully optimize matrix selectivity and MS/MS conditions for effective detection and characterization.

Fig. 5 shows two examples of metabolites identified through this analysis. MS/MS spectra for *m/z* 833.521 were obtained using both silver NPs and DAN. The two spectra are very similar to each other, but DAN gives better signals and is shown in Fig. 5A. Searching the precursor mass against the Metlin database gives 19 metabolites within 5 ppm mass tolerance, all various structural isomers of PI (34:2), but MS/MS spectra are present for none of them. Phospholipids can be manually characterized in MS/MS, most notably from the easily identifiable loss of fatty acid side chains.[33,34] The most intense ion in Fig. 5A, *m/z* 553.3, corresponds to C18:2 fatty acid loss (280.2 Da). The C16:0 fatty acid loss (256.2 Da) is also found at *m/z* 577.3. Further fragmentation results in the two lysophosphatidic acid (LPA) peaks seen at *m/z* 391.3 and 415.3, respectively. These two peaks represent species where the inositol headgroup and one of the fatty acid side chains have fragmented off. Additionally, deprotonated C16:0 and C18:2 fatty acid fragments are found at *m/z* 255.3 and 279.3 respectively. Thus, we can confidently assign this *m/z* 833.517 as PI (18:2/16:0).

It should be noted that we might lose identification of possible structural isomers due to averaging multiple spectra. In the case of PI (34:2) (Fig. 5A), we only see two fatty acid fragments in the averaged spectrum and therefore most likely there is only one structural isomer present in the spectra we averaged. However, some other lipids displayed patterns of fatty acids that could result in multiple structural isomers. For example, MS/MS of PA (36:3) shown in ESI Fig. 3† is an averaged spectrum of 91 MS/MS spectra with the same precursor mass of *m/z* 697.483, and has fragments corresponding to 16:0, 18:0, 18:1, and 18:2 fatty acid chains, suggesting it is most likely the mixture of PA

(16:0/20:3), PA (18:2/18:1) and PA (18:3/18:0), although 20:3 and 18:3 fatty acids and their losses are not detected. However, for the current purpose, we did not verify each MS/MS spectrum, but simply assigned it as PA (36:3). Separate identification of structural isomers could be done efficiently by developing an MS/MS database for automatic searching.

In some cases, interpretation of MS/MS data was not straightforward without reference MS/MS spectra. Fig. 5B shows MS/MS of *m/z* 650.644, which matches with ceramide 42:1 according to the Metlin database. MS/MS spectrum for Cer (d18:1/24:0) was available at Metlin with predicted fragment structures, based on which our MS/MS spectra could be interpreted and was found to match. Although the presence of ceramides is not reported in maize seeds to our knowledge, it has been studied in roots of maize[35] and seeds of other plants.[36] This fact, combined with our MS/MS spectrum matching with that on Metlin, allows us to be confident in the identification of this compound as Cer (d18:1/24:0).

To confirm the robustness of this approach, a replicate experiment was performed on another seed, which showed similar results, as summarized in ESI Fig. 4.† The number of metabolites was lower in negative mode, especially for small molecules, and it was attributed to have come from biological variations. Specifically, acquiring MS/MS of low abundance metabolites is significantly dependent on the native abundance.

Potential metabolites based on accurate mass

As summarized in Fig. 4A, this work suggests that multiplex MSI can potentially identify and visualize over one hundred metabolite ions. Some of them are from the same compound with different alkali metal ion adducts, but there also are many compounds we ignored in this study, including structural isomers and those with low quality MS/MS spectra. As a result, we expect the number of metabolites we can identify to be much higher if we have an available, comprehensive, automatically searchable MS/MS database. In addition to database development, another important step would be to optimize experimental conditions to increase ion signals for low abundance compounds and also their MS/MS spectral quality. While we are working on an MS/MS database for automatic searching and the optimization of experimental conditions, in this section we present the analysis of precursor mass scans to extract how many peaks could be assigned as potential metabolites based only on accurate mass. This allowed us to estimate how many metabolites could be potentially identified once we have an available database and optimized experimental conditions.

The details of how we extracted the potential metabolite mass list from the precursor mass spectra are described in the Experimental section. In short, a peak list present exclusively on the tissue was generated using the peak finder tool in MSiReader with at least 0.1% ion abundance of the base peak; then, ^{13}C isotopes, apparent multiple cation adducts, and possible in-source fragmentations of water loss were manually removed. Fig. 6A shows the summary of this analysis. A total of 341 and 258 peaks were identified as potential unique metabolites present in the precursor mass spectra of positive and negative mode, respectively. The mass values were searched against the Metlin database and Fig. 6B summarizes the result for those peaks that matched with at least one metabolite in the Metlin database within 5 ppm. It suggests a total of 128 and 89 metabolites could be potentially characterized in positive and negative mode, respectively, totaling over two hundred compounds combining both ion modes even in the current ‘limited’ metabolome. Accordingly, this analysis suggests that over two hundred compounds are potentially identifiable, once an MS/MS database becomes available and MS/MS experimental conditions are optimized. Ultimately, five hundred or more compounds could be identified if a more complete understanding of the corn seed metabolome becomes available.

Localization of metabolites in energy-related metabolic pathways

Once we identify hundreds of compounds, the next goal would be understanding the data in the context of metabolic biology. Quantitative analysis is often essential for this purpose in typical metabolomics analysis. Quantifying hundreds of compounds directly on the tissue in MSI, however, is a daunting task; yet, relative quantification could be done comparing different biological states. In the present work, we demonstrate how MSI can be utilized to visualize localization information of metabolic pathways. Two metabolic pathways closely related with energy production, glycolysis and the tricarboxylic acid (TCA) cycle, are demonstrated here as examples. These two pathways are biologically relevant as both of them produce energy needed during seed development, while glycolysis also provides the base units for macromolecule generation and the starting materials for the TCA cycle.[37]

We could visualize the distributions of nine of the ten metabolites involved in glycolysis as shown in Fig. 7. It should be noted that there are some ambiguities in these images. Glucose 6-phosphate (G6P), fructose 6-phosphate (F6P), and fructose 1,6-bisphosphate (F 1,6BP) are confidently identified through MS/MS, but others are solely based on accurate mass in the precursor spectra. Additionally, G6P/F6P and 2&3PG/ PEP are structural isomers and cannot be easily distinguished, even in MS/MS. Thus, the images of G6P/F6P and 2&3PG/PEP shown in Fig. 7 are the same. For the same reason, 2- and 3-phosphoglycerate (2PG, 3PG) are essentially identical.

It is clear from the figure that the use of various matrixes and both polarities is essential to visualize as many compounds as possible in a metabolic pathway. Overall, metabolites involved in the glycolysis metabolic pathway appear to be mostly enriched in the embryo, which is not surprising as metabolic biology is most active when new tissues are being generated such as the radicle (root) and coleoptile (shoot). However, we could see some localization differences between the metabolites. Glucose looks to be localized predominantly to the radicle while fructose 1,6-bisphosphate seems to be more localized to the scutellum of the seed. Meanwhile, compounds like the phosphate sugars and phosphoglycerate compounds seem to be homogeneously distributed throughout the entire embryo region of the seed.

There are several possible explanations why some metabolites show different localization in the same metabolic pathway. For example, glucose is involved not only in glycolysis but also as a building block of many molecular components, which would be especially needed in newly developing tissues such as radicles. Pyruvate was not detected in this study and the images for GADP/DHAP and 1,3BPG were also not clear, potentially due to their low abundance and/or chemical instability.

Fig. 8 shows eight out of the nine metabolites in the TCA cycle, with all of them observed only in negative mode. This is not surprising as all the compounds in the pathway are organic acids, other than succinyl-CoA which is the only nonobserved species in the pathway. Malate, citrate, cis-aconitate, and isocitrate are confirmed with MS/MS, but others are assigned based only on accurate masses.

Similar to Fig. 7, most of the metabolites appear to be localized in the embryo region of the seed. However, some small organic acid compounds (fumarate, succinate, malate) are also observed in the endosperm of the seed. This fact is surprising as typically the endosperm of the seed serves only as an energy source where starch and proteins are broken down for use by the developing seed.[38] According to an in-parallel GC-MS analysis (data not shown; a separate manuscript is in preparation to investigate metabolomic changes at various germination time points), malate is in fact present both in the embryo and endosperm in significant levels. This may indicate that parts of the TCA cycle do occur in the endosperm of the seed, or they could be localized in those areas as parts of other metabolic processes.

Conclusions

A multi-matrix, dual polarity, tandem mass spectrometry imaging strategy is proposed to perform MSI in a large, metabolomics scale. This approach is applied to a germinated corn seed, visualizing a total of 599 potential metabolite ions based solely on accurate mass. Over 90 000 MS/MS spectra were acquired in six multiplex MS imaging data sets, among which at least 166 are unique ions with high quality MS/MS spectra that are potentially identifiable if we have an appropriate MS/ MS library. Among those, 66 ions were confidently identified through manual MS/MS interpretation, with 52 of them being unique compounds. We were able to further demonstrate the utility of this approach by visualizing metabolites involved in the glycolysis and TCA pathways.

Limited by matrix selectivity, MALDI is often considered as a targeted analysis tool. As a result, MALDI-MSI has been limited to visualizing only certain classes of compounds. The current work intends to shift the paradigm and demonstrate MALDI-MSI can be used to visualize metabolites in a large scale. The proposed approach has several limitations compared to conventional untargeted metabolomics analysis. Most of all, due to the lack of chromatographic separation, metabolomic coverage and confidence in identification cannot reach those of LC-MS/MS. These limitations were partly overcome in this approach using natural localization of metabolites and matrix-specific analyte selectivity as ways of separation. Future study will include (1) developing many more matrixes to widen the classes of metabolites that can be efficiently ionized, especially for low abundance compounds, (2) optimizing MS/MS conditions for small molecules, and (3) establishing an ion trap MS/MS database for confident identification and high-throughput analysis. Once successfully accomplished, we envision the proposed approach could be a powerful tool to fully understand metabolic biology with high-spatial localization information.

Acknowledgments

This work was supported by the US Department of Energy (DOE), Office of Basic Energy Sciences, Division of Chemical Sciences, Geosciences and Biosciences. The Ames Laboratory is operated by Iowa State University under DOE Contract DE-AC02-07CH11358. A special thanks to Dr Javier Vela and Marna Yandau-Nelson from Iowa State University for providing materials.

References

1. B. Spengler, M. Hubert, and R. Kaufmann, 1994.
2. R. M. Caprioli, T.B. Farmer and J. Gile, *Anal. Chem.*, 1997, **69**, 4751-4760.
3. A. Svatoš, *Trends Biotechnol.*, 2010, **28,** 425-434.
4. E. M. Weaver and A. B. Hummon, *Adv. Drug Delivery Rev.*, 2013, **65**, 1039-1055.
5. L. A. McDonnell and R. Heeren, *Mass Spectrom. Rev.*, 2007, **26**, 606-643.
6. E. R. A. van Hove, D. F. Smith and R. M. Heeren, *J. Chromatogr., A*, 2010, **1217**, 3946-3954.
7. G. Marko-Varga, T. E. Fehniger, M. Rezeli, B. Döme, T. Laurell and Á. Végvári, *J. Proteomics*, 2011, **74**, 982-992.
8. H. Ye, E. Gemperline, M. Venkateshwaran, R. Chen, P. M. Delaux, M. Howes-Podoll, J. M. Ané, and L. Li, *Plant J.*, 2013, **75**, 130-145.
9. R. A. Dixon and D. Strack, *Phytochemistry*, 2003, **62**, 815-816.
10. R. Goodacre, S. Vaidyanathan, W. B. Dunn, G. G. Harrigan and D. B. Kell, *Trends Biotechnol.*, 2004, **22**, 245-252.
11. X.-L. Shu, T. Frank, Q.-Y. Shu and K.-H. Engel, *J. Agric. Food Chem.*, 2008, **56**, 11612-11620.
12. U. Roessner, C. Wagner, J. Kopka, R. N. Trethewey and L. Willmitzer, *Plant J.* 2000, **23**, 131-142.
13. Y. Tikunov, A. Lommen, C. R. de Vos, H. A. Verhoeven, R. J. Bino, R. D. Hall and A. G. Bovy, *Plant Physiol.,* 2005, **139**, 1125-1137.
14. D. Perdian and Y. J. Lee, *Anal. Chem.*, 2010, **82**, 9393-9400.
15. A. R. Korte and Y. J. Lee, *J. Am. Soc. Mass Spectrom.*, 2013, **24**, 949-955.
16. J. D. Bewley, *Plant Cell*, 1997, **9**, 1055.
17. A. T. Klein, G. B. Yagnik, J. D. Hohenstein, Z. Ji, J. Zi, M. D. Reichert, G. C. MacIntosh, B. Yang, R. J. Peters and J. Vela, *Anal. Chem.*, 2015.
18. A. R. Korte, G. B. Yagnik, A. D. Feenstra and Y. J. Lee, in *Mass Spectrometry Imaging of Small Molecules*, Springer, 2015, pp. 49-62.
19. J. A. Hankin, R. M. Barkley and R. C. Murphy, *J. Am. Soc. Mass Spectrom.*, 2007, **18,** 1646-1652.
20. J. H. Jun, Z. Song, Z. Liu, B. J. Nikolau, E. S. Yeung and Y. J. Lee, *Anal. Chem*, 2010, **82**, 3255-3265.
21. G. Robichaud, K. P. Garrard, J. A. Barry and D. C. Muddiman, *J. Am. Soc. Mass Spectrom.*, 2013, **24**, 718-721.
22. A. I. Thomas, J. L. Charbonneau, E. Fournaise and P. Chaurand, *Anal. Chem.*, 2012, **84**, 2048-2054.
23. A. R. Korte and Y. J. Lee, *J. Mass Spectrom.*, 2014, **49**, 737-741.
24. R. L. Vermillion-Salsbury and D. M. Hercules, *Rapid Commun. Mass Spectrom.*, 2002, **16**, 1575-1581.
25. M. Burrell, C. Earnshaw and M. Clench, *J. Exp. Bot.*, 2007, **58**, 757-763.
26. F. Benabdellah, D. Toubol, A. Brunelle and O. Laprévote, *Anal. Chem.*, 2009, **81**, 5557-5560.
27. S. N. Jackson, K. Baldwin, L. Muller, V. M. Womack, J. A. Schultz, C. Balaban and A. S. Woods, *Anal Bioanal. Chem.,* 2014, **406**, 1377-1386.
28. T. Hayasaka, N. Goto-Inoue, N. Zaima, K. Shrivas, Y. Kashiwagi, M. Yamamoto, M. Nakamoto and M. Setou, *J. Am. Soc. Mass Spectrom.*, 2010, **21**, 1446-1454.

29. J. Schiller, J. Arnhold, S. Benard, M. Müller, S. Reichl and K. Arnold, *Anal. Biochem.*, 1999, **267**, 46-56.
30. K. Strupat, M. Karas and F. Hillenkamp, *Int. J. Mass Spectrom. Ion Processes*, 1991, **111**, 89-102.
31. D. Harvey, *Rapid Commun. Mass Spectrom.*, 1993, **7**, 614-619.
32. K. R. Jonscher and J. R. Yates, *Anal. Biochem.*, 1997, **244**, 1-15.
33. S. N. Jackson, H.-Y. J. Wang and A. S. Woods, *J. Am. Soc. Mass Spectrom.*, 2005, **16**, 2052-2056.
34. N. E. Manicke, J. M. Wiseman, D. R. Ifa and R. G. Cooks, *J. Am. Soc. Mass Spectrom.*, 2008, **19**, 531-543.
35. L. D. Williams, A. E. Glenn, A. M. Zimeri, C. W. Bacon, M. A. Smith and R. T. Riley, *J. Agric. Food Chem.*, 2007, **55**, 2937-2946.
36. J. J. Salas, J. E. Markham, E. Martínez-Force and R. Garcés, *J. Agric. Food Chem.*, 2011, **59**, 12486-12492.
37. W. C. Plaxton, *Annu. Rev. Plant Biol.*, 1996, **47**, 185-214.
38. D. Yan, L. Duermeyer, C. Leoveanu and E. Nambara, *Plant Cell Physiol.*, 2014, pcu089.

Figures

Fig. 1 Four step multiplex MSI setup used in this work. Steps 1 and 3 are high resolution Orbitrap scans in low and high mass range. Steps 2 and 4 are data dependent ion trap MS/MS scans.

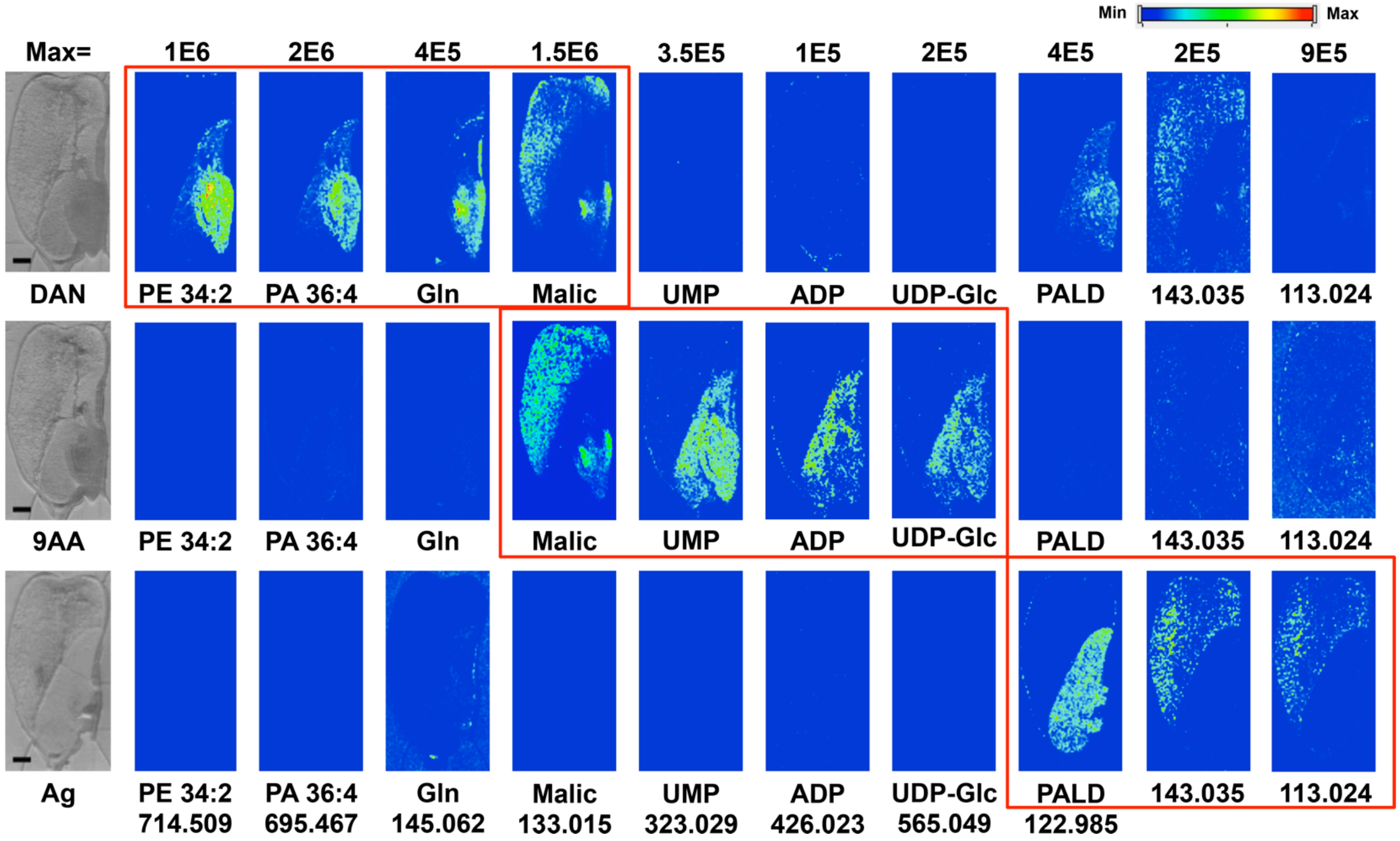

Fig. 2 Comparison of ten representative compounds in a germinated maize seed showing different selectivity between three matrixes in negative ion mode. MS images are shown for phosphatidylethanolamine 34:2 (PE 34:2), phosphatidic acid 36:4 (PA 36:4), glutamine (Gln), malic acid (Malic), uridine monophosphate (UMP), adenosine diphosphate (ADP), uridine diphosphate glucose (UDP-Glc), phosphonoacetaldehyde (PALD), and two unknown compounds at *m/z* 143.035 and 113.024. *m/z* values used in generating images are given at the bottom of the figure. Red boxes highlight ion images more selectively detected with a given matrix than in other matrixes. All ions are observed as deprotonated species. Scale bars represent 1 mm.

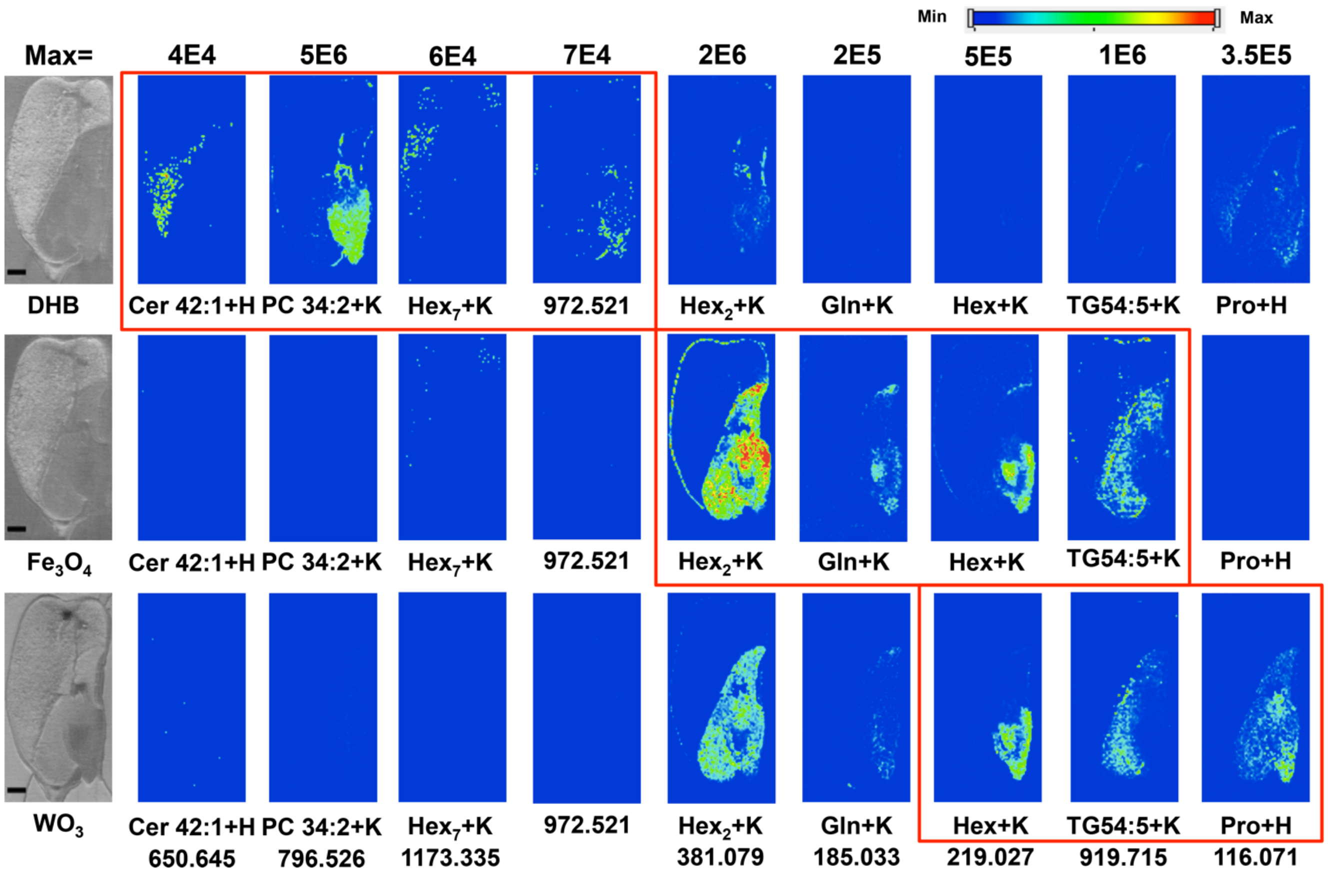

Fig. 3 Comparison of nine representative compounds in a germinated maize seed between three matrixes in positive ion mode. MS images are shown for ceramide 42:1 (Cer 42:1), phosphatidylcholine 34:2 (PC 34:2), heptahexose (Hex$_7$), an unknown compound at *m/z* 972.521, dihexose (Hex$_2$), glutamine (Gln), monohexose (Hex), triacylglycerol 54:5 (TG 54:5), and proline (Pro). Red boxes highlight ion images more selectively detected with a given matrix than in other matrixes. All known compounds are shown as a potassium adduct, except for ceramide and proline, which are shown as a proton adduct. Scale bars represent 1 mm.

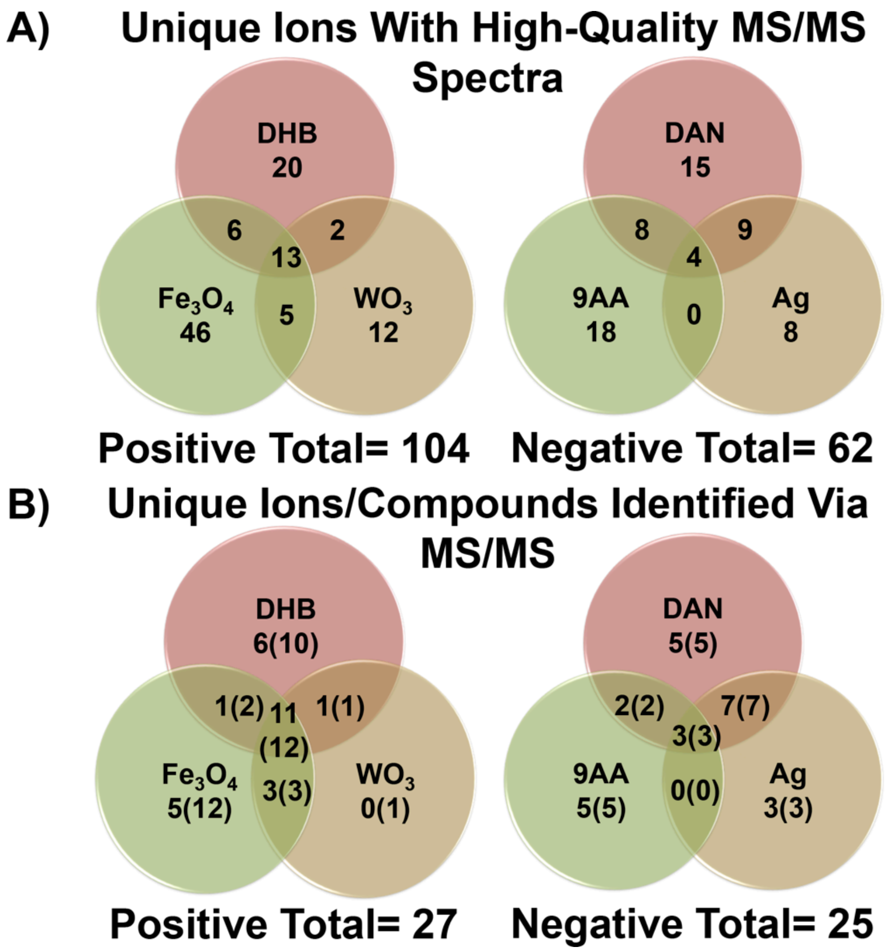

Fig. 4 Venn diagrams displaying (A) the number of unique ions with high-quality MS/MS spectra and (B) the number of unique compounds (outside parentheses) and total number of ions (in parentheses) identified via manual interpretation of MS/MS spectra. The number of unique compounds identified is after the removal of multiple adducts or fragments of the same species.

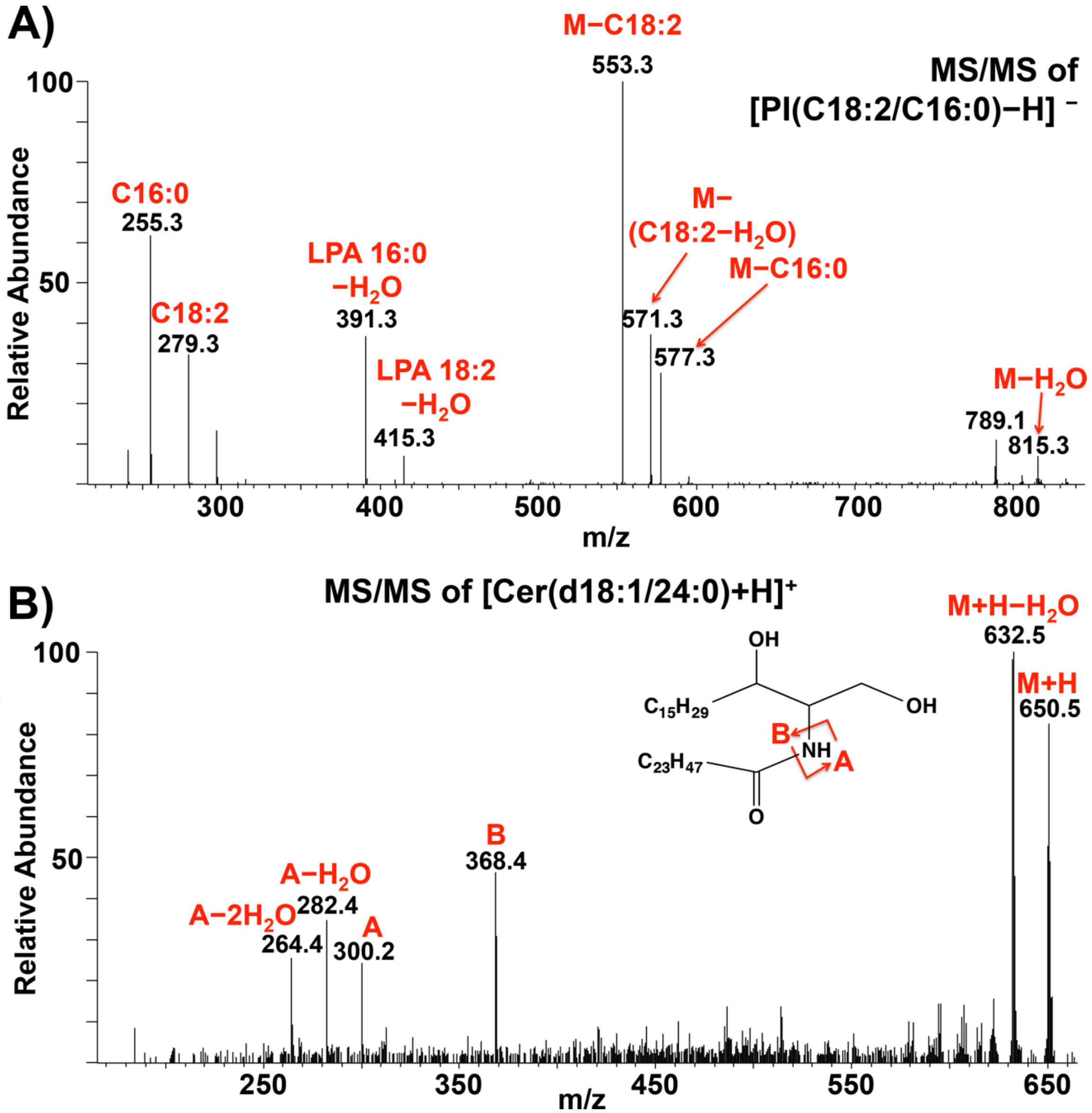

Fig. 5 MS/MS spectra for (A) *m/z* 833.521 with DAN as a matrix in negative ion mode, and (B) *m/z* 650.644 with DHB as a matrix in positive ion mode. They are assigned as deprotonated PI (18:2/16:0) and protonated Cer (d18:1/24:0), respectively, according to accurate precursor mass and MS/MS analysis.

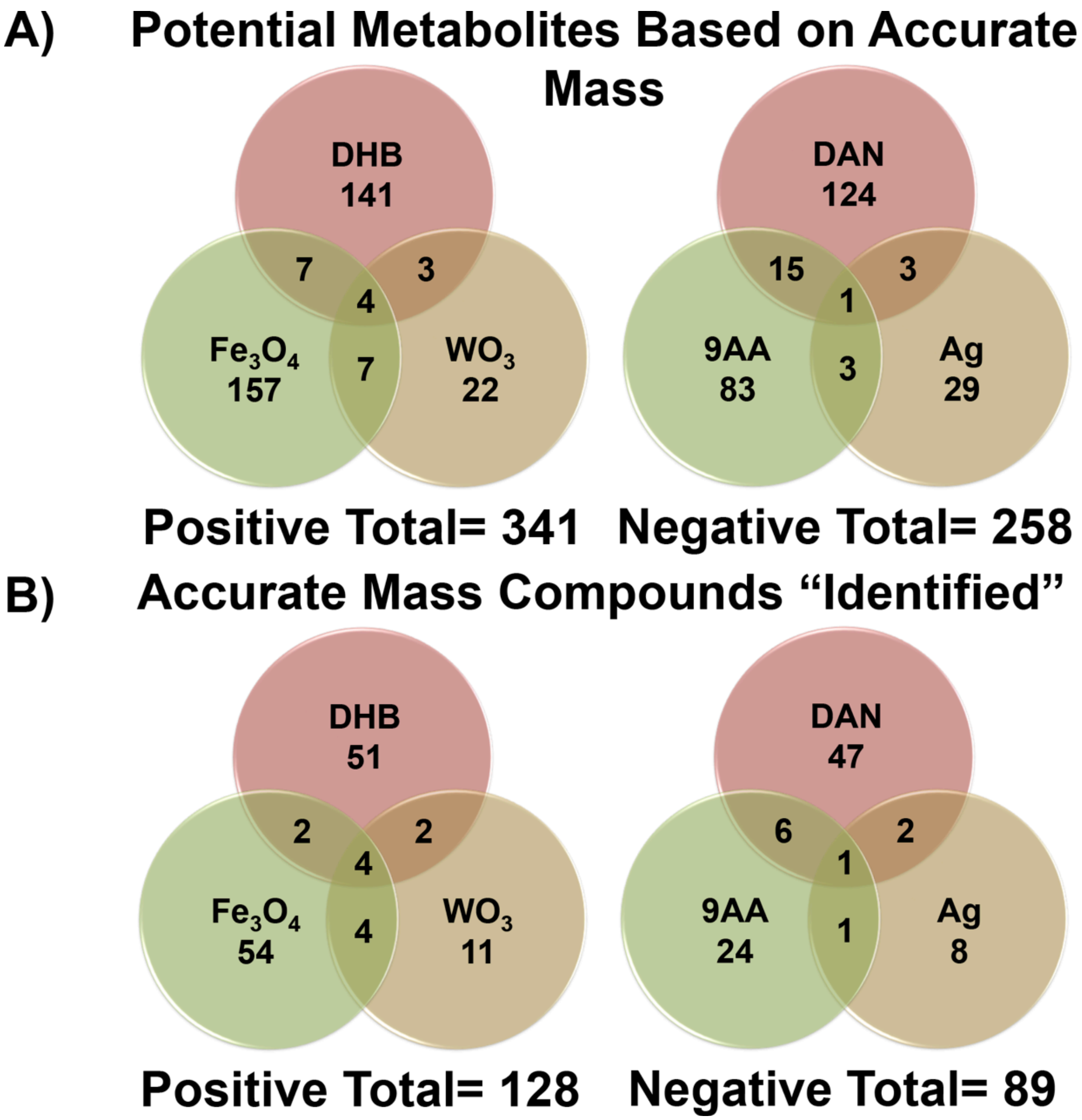

Fig. 6 Venn diagrams displaying (A) number of potential compounds based only on accurate mass, and (B) number of potentially identified compounds from accurate mass search against the Metlin database.

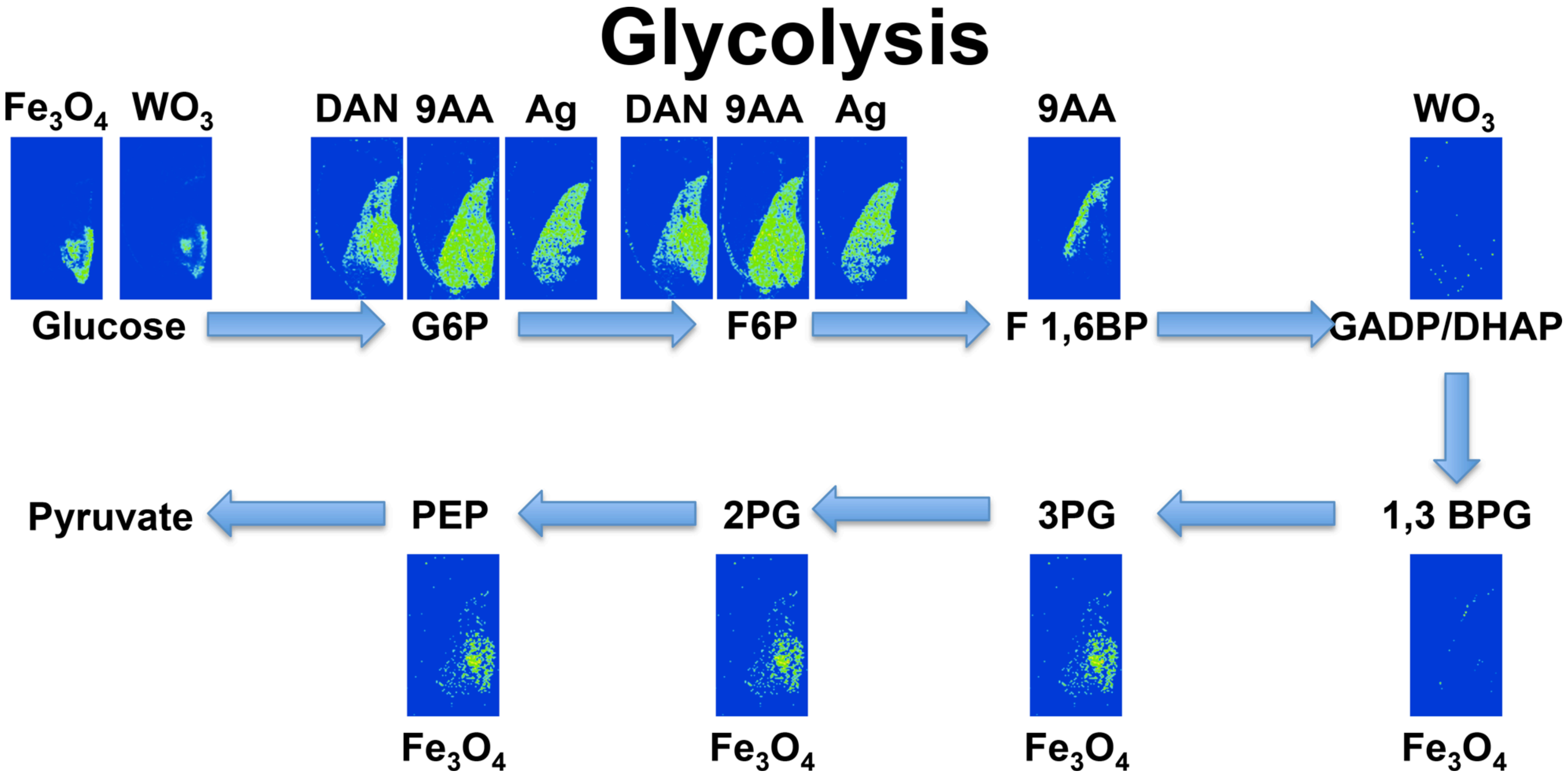

Fig. 7 The images of metabolites involved in the glycolysis pathway. Compounds in negative mode are shown as deprotonated species. In positive mode, glucose, glyceraldehyde 3-phosphate (GADP)/dihydroxyacetonephosphate (DHAP), 1,3 bisphosphoglycerate (1,3 BPG), and phosphoenolpyruvate (PEP) are seen as potassium adducts and 2- and 3-phosphoglycerate (2PG, 3PG) are seen as potassiated water loss species.

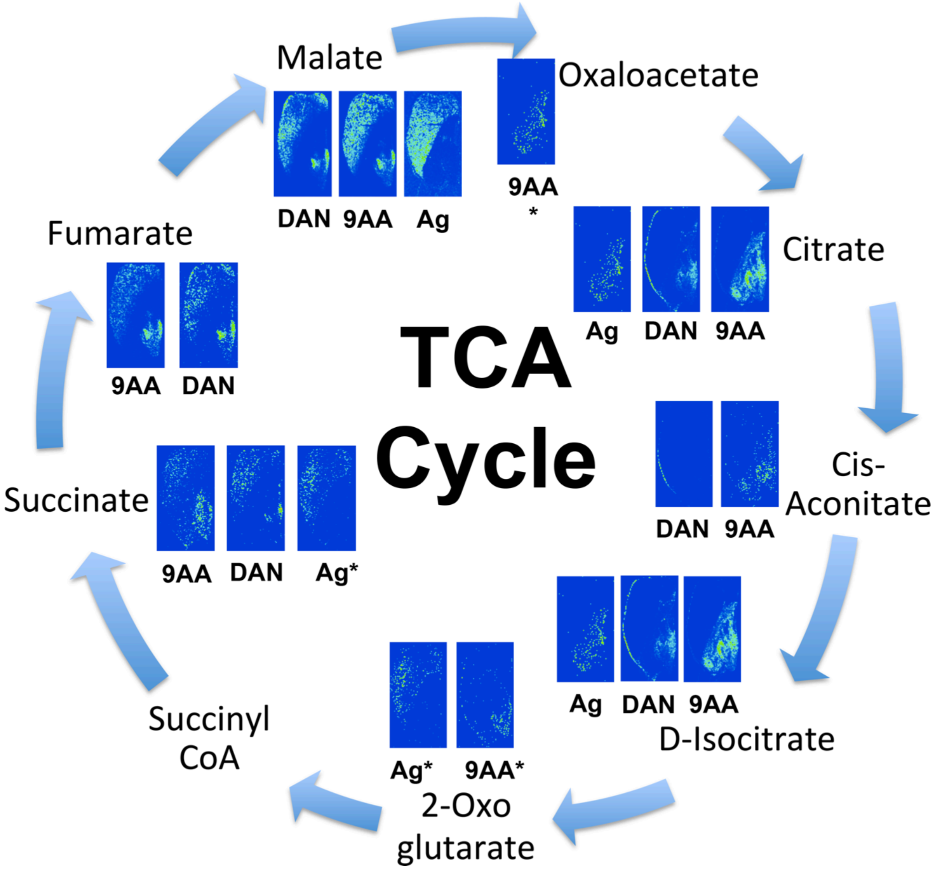

Fig. 8 The images of metabolites involved in the TCA Cycle. Ions are all observed in negative mode as deprotonated species, except for those with asterisks, which are shown as deprotonated water loss species.

Supplemental Figures and Tables

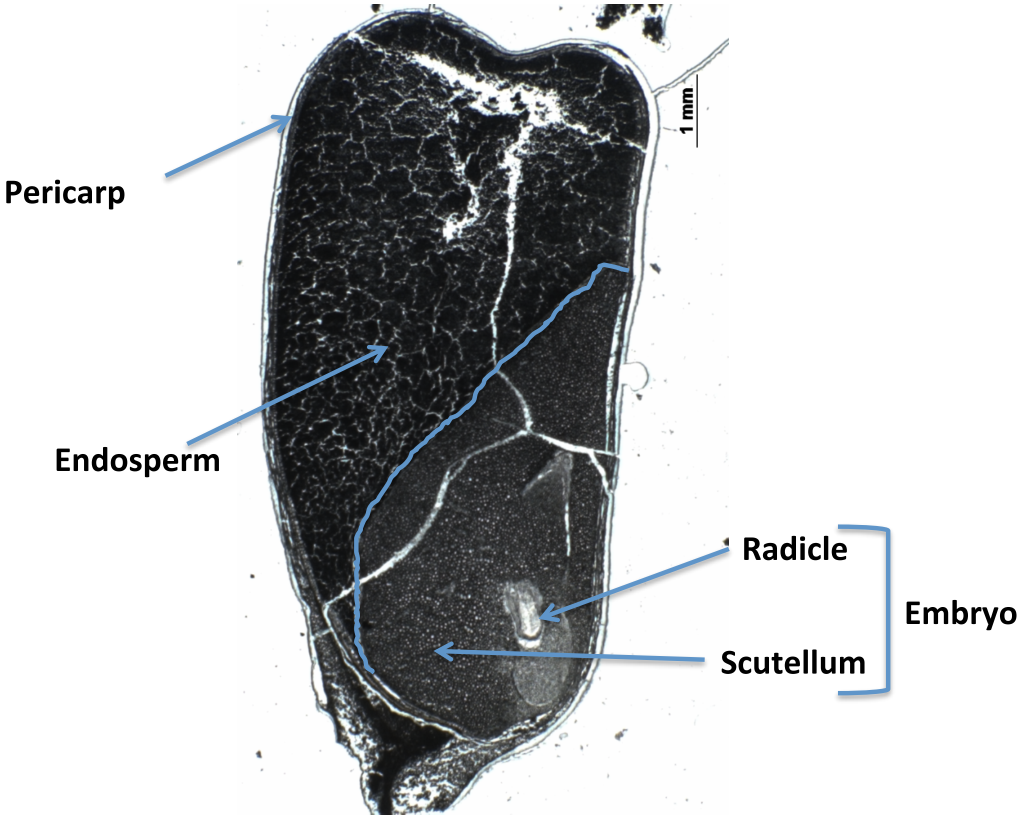

Supplementary Figure 1: Anatomy of maize seed. Pericarp: Outer layers of the seed that protect the seed. Endosperm: Starchy storage area. Scutellum: Oil storage area and metabolically active region during germination. Radicle: Primary root. Coleoptile, protective sheath of emerging shoot and also a part of embryo, is not seen yet in this image. The blue line through the seed serves as a visual representation of the boundary between the embryo and endosperm.

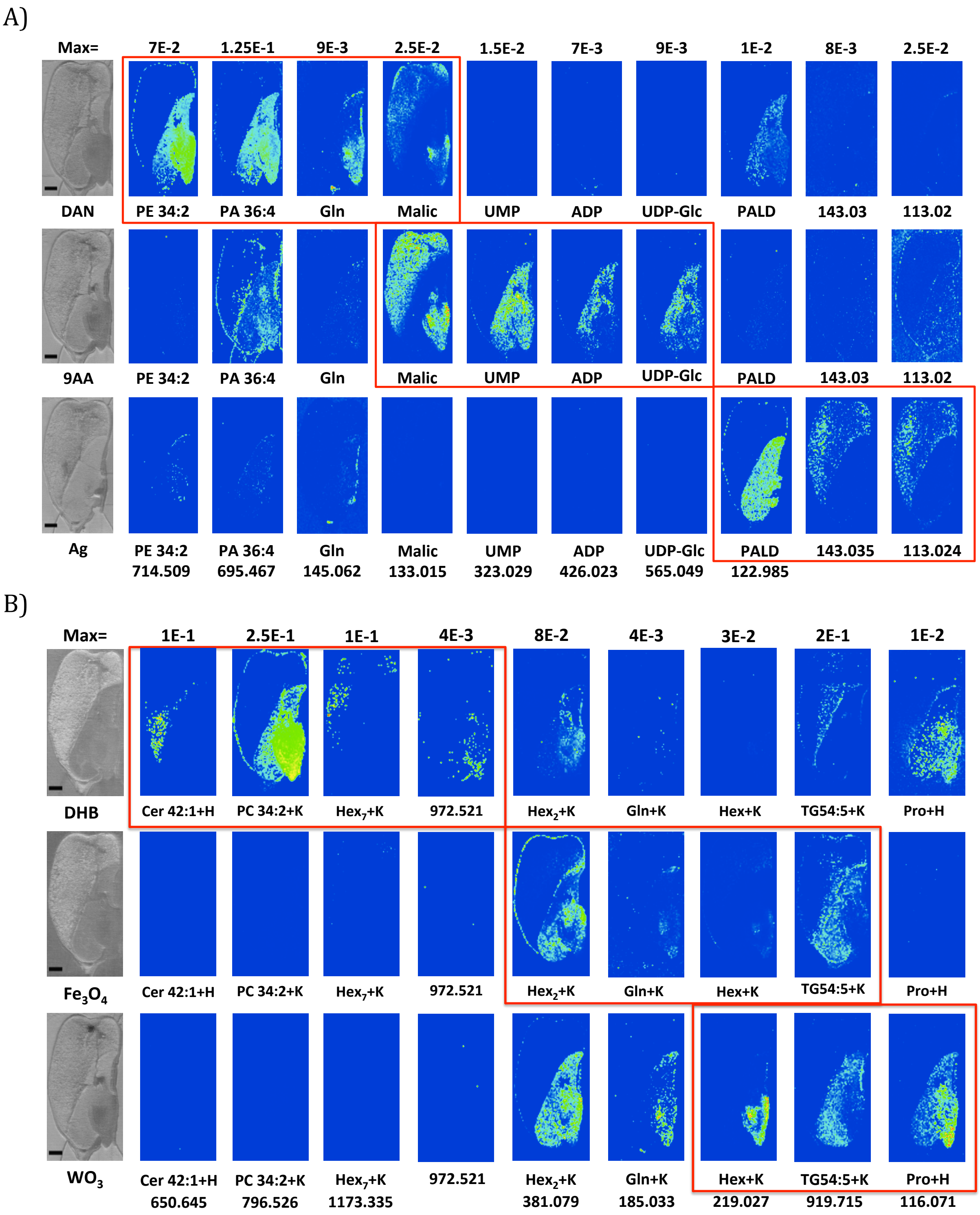

Supplementary Figure 2. Comparison of matrix effectiveness for various classes of compounds. The same images shown in Figure 2 for negative mode (A) and Figure 3 for positive mode (B) but normalized against total ion count with maximum values adjusted for each compound. Scale bars represent 1mm.

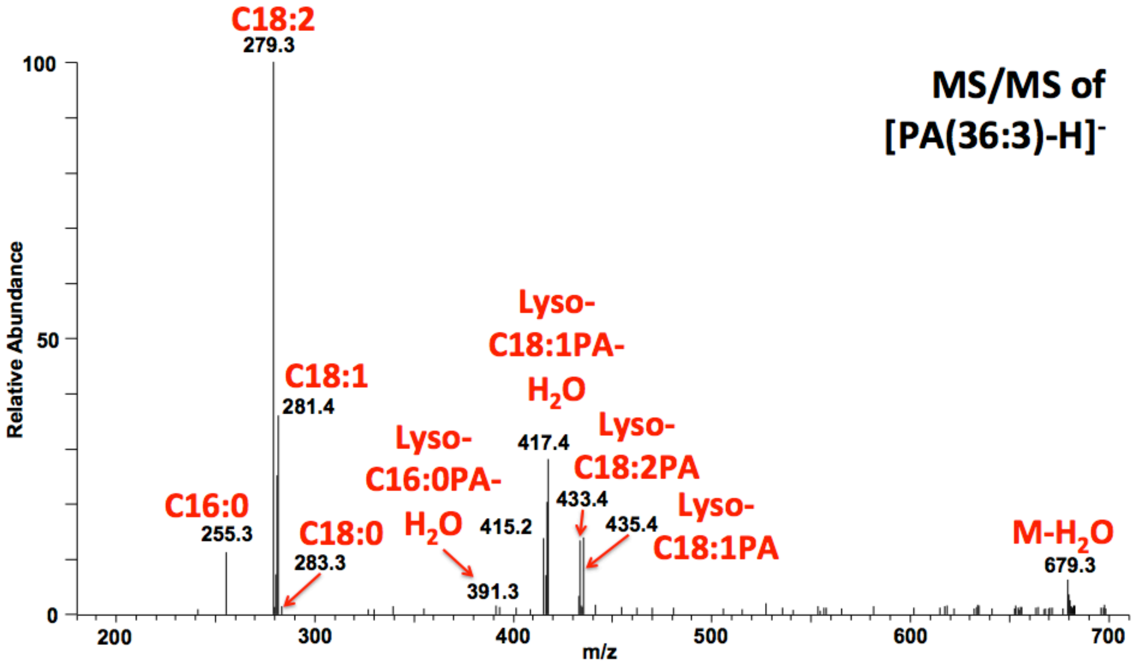

Supplementary Figure 3. An average of 91 MS/MS spectra for PA (36:3) at *m/z* 697.483 using DAN as a matrix in negative ion mode. Fragments include C16:0 (*m/z* 255.3), C18:2 (*m/z* 279.3), C18:1 (*m/z* 281.4), and C18:0 (*m/z* 283.3) fatty acid chains, along with several corresponding Lyso-PA fragments. This MS/MS spectrum is considered as a mixture of PA (16:0/20:3), PA (18:1/18:2), and PA (18:0/18:3).

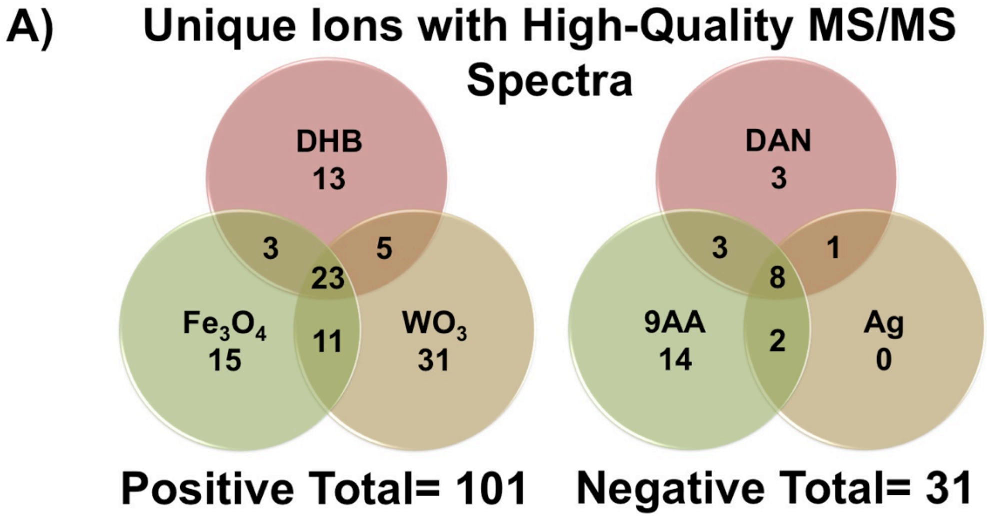

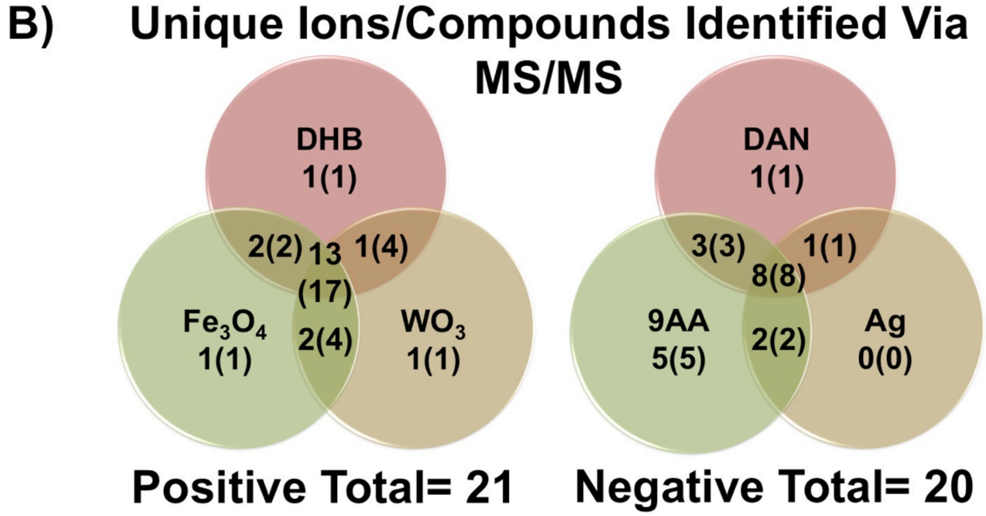

Supplementary Figure 4. The same as Figure 4 but in a replicate experiment with another seed, to demonstrate the robustness of the method. A lower number of small molecules were detected in negative mode. This was attributed to biological variations between the seeds.

Supplementary Table 1: All 104 unique positive ions with high quality MS/MS spectra that passed through MS/MS filtering. Highlighted are ions identified via MS/MS, as assigned in Suppl. Table 3.

All Three	DHB/Fe_3O_4	WO_3/Fe_3O_4	WO_3/DHB	DHB Only	Fe_3O_4 Only		WO_3 Only
184.073	212.852	749.393	739.469	198.089	112.896	706.612	600.763
381.080	765.485	785.472	901.218	222.029	119.930	713.455	631.142
601.520	777.427	903.740		230.946	120.926	727.731	647.092
603.535	792.435	917.701		268.901	154.027	745.238	649.095
735.437	824.559	921.731		614.910	156.886	751.411	651.098
737.453	911.446			637.458	185.042	773.394	655.470
775.410				645.166	274.808	787.468	687.052
796.526				650.644	310.913	798.545	741.154
820.526				692.619	379.203	816.436	761.453
822.542				697.343	607.011	831.510	808.571
893.701				756.554	611.179	833.253	935.712
895.717				758.570	626.529	833.494	949.692
919.716				763.469	629.143	877.726	
				784.585	631.411	879.741	
				786.600	635.413	881.755	
				913.447	638.550	901.365	
				913.704	645.116	901.727	
				1011.281	654.511	905.757	
				1173.337	659.502	907.771	
				1497.440	671.200	917.338	
					681.220	995.306	
					699.195	1169.735	
					699.699	1331.145	

Supplementary Table 2: All 62 unique negative ions with high quality MS/MS spectra that passed through MS/MS filtering. Highlighted are ions identified via MS/MS, as assigned in Supp. Table 4

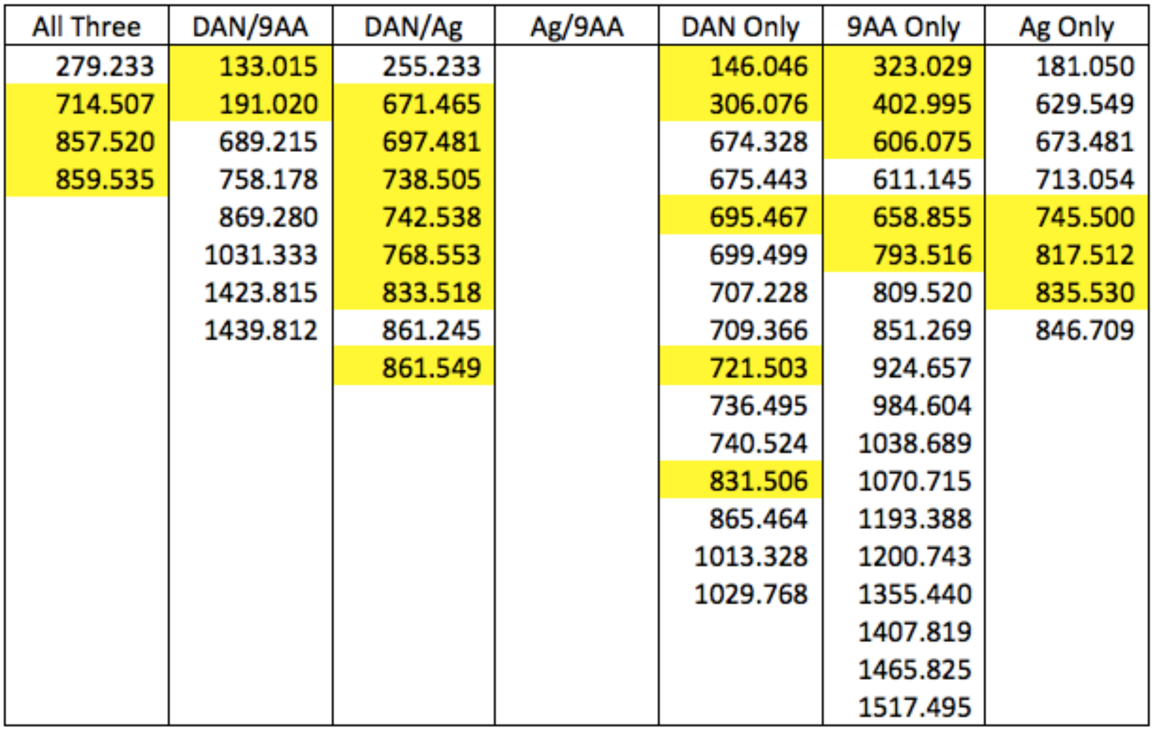

All Three	DAN/9AA	DAN/Ag	Ag/9AA	DAN Only	9AA Only	Ag Only
279.233	133.015	255.233		146.046	323.029	181.050
714.507	191.020	671.465		306.076	402.995	629.549
857.520	689.215	697.481		674.328	606.075	673.481
859.535	758.178	738.505		675.443	611.145	713.054
	869.280	742.538		695.467	658.855	745.500
	1031.333	768.553		699.499	793.516	817.512
	1423.815	833.518		707.228	809.520	835.530
	1439.812	861.245		709.366	851.269	846.709
		861.549		721.503	924.657	
				736.495	984.604	
				740.524	1038.689	
				831.506	1070.715	
				865.464	1193.388	
				1013.328	1200.743	
				1029.768	1355.440	
					1407.819	
					1465.825	
					1517.495	

Supplementary Table 3. Tentatively identified compounds in positive mode summarized in Figure 4B.

m/z[a]	Suspected Identity[b]	Species Observed[a]	Mass Error[c] (ppm)	*m/z* of fragment ions and assignments[d]
184.074	Phosphocholine†‡	+H	0.9, 0.8, 1.5	125 (-$N(CH_3)_3$), 86(-Phos)
222.029		+K	-0.1, XX, XX	163 (-$N(CH_3)_3$)
198.089	Methacholine†	+K	-0.7, XX, XX	139 (-$N(CH_3)_3$)
381.080	Disaccharide†	+K	-0.3, 2.6, 0.9	219 (-Hex-H_2O), 201 (-Hex)
601.519	DAG 36:3 Frag	+H	0.3, 0.4, 1.0	319 (-18:1), 345 (-16:0)
603.535	DAG 36:2 Frag	+H	0.6, 0.4, 1.5	347 (-16:0)
659.502	DAG 36:2	+K	XX, 0.6, XX	403 (-16:0), 379 (-18:2)
650.644	Cer 42:1†	+H	-1.6, XX, XX	300 (-24:0), 282 (300-H_2O), 264 (282-H_2O), 368 (-18:1dOH) See Figure 6 for structures
671.200	Hex 4	-H_2O+Na	XX, 0.7, XX	509.20 (-Hex-H_2O), 347.18 (-2Hex-2H_2O)
735.437	PC 32:0	-$N(CH_3)_3$+Na+K	3.5, 5.0, 4.1	611 (-(PCho-$N(CH_3)_3$)), 479 (-16:0)
751.411		-$N(CH_3)_3$+2K	XX, 4.1, XX	495 (-16:0)
737.453	PC 34:2	-$N(CH_3)_3$+K+H	0.3, 3.0, 1.2	613 (-(PCho-$N(CH_3)_3$)), 481 (-16:0)
796.526		+K	0.7, 2.1, 0.9	737 (-$N(CH_3)_3$), 613 (-PCho), 540 (-16:0), 516 (-18:2)
758.570		+H	0.3, XX, XX	699 (-$N(CH_3)_3$), 575 (-PCho), 502 (-16:0), 478 (-18:2)
739.470	PC 34:1	-$N(CH_3)_3$+K+H	3.9, XX, 2.5	615 (-(PCho-$N(CH_3)_3$)), 483 (-16:0)
777.427		-$N(CH_3)_3$+2K	4.2, 4.8, XX	734 (-C_2H_4O), 521 (-16:0), 495 (-18:1), 493 (-18:0)
798.545		+K	XX, 4.5, XX	739 (-$N(CH_3)_3$)
761.453		-$N(CH_3)_3$+Na+K	XX, XX, 4.0	637 (-(PCho-$N(CH_3)_3$)), 505 (-16:0)
763.469	PC 34:0	-$N(CH_3)_3$+Na+K	5.3, XX, XX	639 (-(PCho-$N(CH_3)_3$))
820.526	PC 36:4	+K	0.6, 1.9, 0.9	761 (-$N(CH_3)_3$), 637 (-PCho), 564 (-16:0), 540 (-18:2), 538 (-18:1)
822.542	PC 36:3	+K	-2.0, 1.9, 0.8	763 (-$N(CH_3)_3$), 639 (-PCho), 566 (-16:0), 542 (-18:2), 540 (-18:1)
784.585		+H	-0.3, XX, XX	725 (-$N(CH_3)_3$), 504 (-18:2), 502 (-18:1)
824.559	PC 36:2	+K	2.0, 4.7, XX	765 (-$N(CH_3)_3$), 641 (-PCho)
786.600		+H	-1.0, XX, XX	506 (-18:2), 504 (-18:1)

Table S3 (cont'd)

893.701 877.726	TAG 52:4	+K +Na	1.0, 2.2, 1.8 XX, 1.0, XX	637 (-16:0), 613 (-18:2), 319 (-DAG 34:2) 621 (-16:0), 597 (-18:2), 575 (DAG 34:2 Frag+H)
895.716 879.741	TAG 52:3†	+K +Na	0.4, 2.3, 1.9 XX, -0.1, XX	639 (-16:0), 615 (-18:2), 613 (-18:1) 623 (-16:0), 599 (-18:2), 597 (-18:1), 577 (DAG 34:1 Frag+H), 575 (DAG 34:2 Frag+H)
881.755	TAG 52:2	+Na	XX, -1.6, XX	625 (-16:0), 599 (-18:1), 577 (DAG 34:1 Frag+H)
917.701 901.727	TAG 54:6‡	+K +Na	XX, 1.8, 1.5 XX, 0.8, XX	661 (-16:0), 637 (-18:2), 655 (-(18:2-H2O)) 621 (-18:2), 599 (DAG 36:4 Frag+H)
919.716	TAG 54:5‡	+K	1.0, 1.0, 1.6	663 (-16:0), 639 (-18:2), 637 (-18:1)
921.732 905.757	TAG 54:4‡	+K +Na	XX, 0.7, 1.7 XX, -0.6, XX	641 (-18:2), 639 (-18:1) 625 (-18:2), 623 (-18:1), 601 (DAG 36:3 Frag+H)
907.771	TAG 54:3	+Na	XX, -1.8, XX	651 (-16:0), 625 (-18:1), 623 (-18:0), 333 (-DAG 34:2)
903.740	TAG 56:8	+H	XX, -2.4, -3.7	623 (-18:2), 621 (-18:1), 601 (DAG 36:3 Frag+H)
833.253	Hexose 5	-H_2O+Na	XX, 2.0, XX	671 (-(Hex-H_2O)), 509 (-(2Hex-2H_2O)), 347 (-(3Hex-3H_2O))
1011.281 995.306	Hexose 6†	-H_2O+K -H_2O+Na	0.7, XX, XX XX, 0.3, XX	849 (-(Hex-H_2O)), 687 (-(2Hex-2H_2O)) 833 (-(Hex-H_2O)), 671 (-(2Hex-2H_2O)), 509 (-(3Hex-3H_2O))
1173.337	Hexose 7†	-H_2O+K	0.0, XX, XX	1011 (-(Hex-H_2O)), 849 (-(2Hex-2H_2O))
1497.440	Hexose 9	-H_2O+K	1.0, XX, XX	1335 (-(Hex-H_2O)), 1173 (-(2Hex-2H_2O)), 1011 (-(3Hex-3H_2O))

a. The same compound detected as various adducts were grouped together and species observed were shown.
b. Assignments were based on accurate mass search on Metlin and manual MS/MS interpretation. † and ‡ denote when MS/MS spectra were available in Metlin and MassBank database, respectively, and used for comparison.
c. Mass errors are shown in the order of DHB, Fe_3O_4 NP and WO_3 NP matrix. XX represents that there is no peak for the given matrix.
d. Fragment assignments are shown in the parenthesis. $N(CH_3)_3$: choline head group. Phos: phosphoric acid (H_3PO_4). Hex: hexose (e.g., glucose). (Hex-H_2O): water loss from hexose. PCho: phosphocholine head group. PCho-$N(CH_3)_3$: Phosphocholine head group with trimethyl amine loss. 16:0, 18:0, 18:1, 18:2: C16:0, C18:0, C18:1 and C18:2 fatty acid, respectively.

Supplementary Table 4. Tentatively identified compounds in negative mode summarized in Figure 4B.

m/z	Suspected Identity[a]	Species Observed	Mass Error[b] (ppm)	*m/z* of fragment ions and assignments[c]
133.015	Malic Acid†‡	-H	4.5, 3.7, XX	87, 71
146.046	Glutamic Acid†‡	-H	3.1, XX, XX	128 (-H_2O), 102 (-CO_2)
191.020	Citric Acid/Isocitrate†‡	-H	1.1, 1.7, XX	111, 87
306.076	Glutathione†‡	-H	-0.2, XX, XX	288, 272, 254
323.029	Uridine monophosphate†‡	-H	XX, -0.3, XX	280, 211
402.995	Uridine diphosphate†‡	-H	XX, 0.5, XX	385, 305, 273
606.075	UDP-N-acetylglucosamine†‡	-H	XX, 1.6, XX	403, 385, 282, 273
658.855	Phytic Acid	-H	XX, 0.8, XX	561 (-Phos), 463 (-2 Phos)
671.464	PA 34:2	-H	0.0, XX, -3.2	415 (-16:0), 409 (-(18:2-H_2O)), 391 (-18:2), 279 (18:2-H), 255 (16:0-H)
695.467	PA 36:4	-H	2.1, XX, XX	433 (-(18:2-H_2O)), 415 (-18:2), 279 (18:2-H)
697.480	PA 36:3	-H	2.9, XX, -2.8	417 (-18:2), 415 (-18:1), 281 (18:1-H), 279 (18:2-H)
714.508	PE 34:2	-H	2.3, -0.0, -2.6	452 (-(18:2-H_2O)), 434 (-18:2), 279 (18:2-H), 255 (16:0-H)
738.505	PE 36:4‡	-H	2.5, XX, -4.4	476 (-(18:2-H_2O)), 279 (18:2-H)
742.540	PE 36:2‡	-H	2.5, XX, -4.2	480 (-(18:2-H_2O)), 462 (-18:2), 281 (18:1-H), 279 (18:2-H), 255 (16:0-H)
768.553	PE 38:3	-H	1.7, XX, -2.8	281 (18:1-H), 279 (18:2-H)
721.503	PG 32:0	-H	1.3, XX, XX	483 (-(16:0-H_2O)), 465 (-16:0), 391 (LPA16:0-H_2O), 255 (-16:0)

Table S4 (cont'd)

745.500	PG 34:2	-H	XX, XX, -3.2	279 (18:2-H), 255 (16:0-H)
831.506	PI 34:3‡	-H	3.4, XX, XX	553 (-18:3), 391 (LPA 16:0-H_2O), 277 (18:3-H), 255 (16:0-H), 241 (Inositol 6-phosphate-H_2O)
833.517	PI 34:2‡	-H	3.2, XX, -2.4	577 (-16:0), 571 (-(18:2-H_2O)), 553 (-18:2), 391 (LPA 16:0-H_2O), 279 (18:2-H), 255 (16:0-H), 241 (Inositol 6-Phosphate-H_2O)
835.530	PI 34:1‡	-H	XX, XX, -4.9	579 (-16:0), 571 (-(18:1-H_2O)), 553 (-18:1), 391 (LPA16:0-H_2O), 281 (18:1-H), 255 (16:0-H)
857.520	PI 36:4	-H	2.7, 1.9, -1.3	595 (-(18:2-H_2O)), 577 (-18:2), 415 (LPA18:2-H_2O), 279 (18:2-H), 241 (Inositol 6-phosphate-H_2O)
859.535	PI 36:3‡	-H	1.7, 2.1, -2.6	579 (-18:2), 577(-18:1) 417 (LPA18:1-H_2O), 281 (18:1-H), 279 (18:2-H)
861.550	PI 36:2‡	-H	2.4, XX, -3.0	581 (-18:2), 579 (-18:1), 283 (18:0-H)
793.516	SQDG 32:0	-H	XX, 1.8, XX	537 (-16:0)
817.512	SQDG 34:2	-H	XX, XX, -2.5	561 (-16:0), 537 (-18:2)

a. Assignments were based on accurate mass search on Metlin and manual MS/MS interpretation. † and ‡ denote when MS/MS spectra were available in Metlin and MassBank database, respectively, and used for comparison.

b. Mass errors are shown in the order of DAN, 9AA, and Ag NP matrix. XX represents there is no peak for the given matrix.

c. Fragment assignments are shown in the parenthesis. Phos: phosphoric acid (H_3PO_4). LPA: lysophosphatidic acid species with fatty acid chain denoted. 16:0, 18:0, 18:1, 18:2, 18:3: C16:0, C18:0, C18:1, C18:2, and C18:3 fatty acid, respectively. Masses without easily assigned fragments are not labeled. Rather, matching structures can be found online at the Metlin or MassBank databases.

CHAPTER 4

ORGANIC-INORGANIC BINARY MIXTURE MATRIX FOR COMPREHENSIVE LASER-DESORPTION IONIZATION MASS SPECTROMETRIC ANALYSIS AND IMAGING OF MEDIUM-SIZE MOLECULES INCLUDING PHOSPHOLIPIDS, GLYCEROLIPIDS, AND OLIGOSACCHARIDES

A paper published in *RSC Advances*

RSC Adv., 2016, **6**, 99260-99268
Reproduced by permission of the Royal Society of Chemistry

Adam D. Feenstra, Kelly C. O'Neill, Gargey B. Yagnik, and Young Jin Lee

Abstract

Matrix-assisted laser desorption/ionization mass spectrometry (MALDI-MS) is a widely adopted, versatile technique, especially in high-throughput analysis and imaging. However, matrix-dependent selectivity of analytes is often a severe limitation. In this work, a mixture of organic 2,5-dihydroxybenzoic acid and inorganic Fe_3O_4 nanoparticles is developed as a binary MALDI matrix to alleviate the well-known issue of triacylglycerol (TG) ion suppression by phosphatidylcholine (PC). In application to lipid standards and maize seed cross-sections, the binary matrix not only dramatically reduced the ion suppression of TG, but also efficiently desorbed and ionized a wide variety of lipids such as cationic PC, anionic phosphatidylethanolamine (PE) and phosphatidylinositol (PI), and neutral digalactosyldiacylglycerol (DGDG). The binary matrix was also very efficient for large polysaccharides, which were not detected by either of the individual matrices. The usefulness of the binary matrix is demonstrated in MS imaging of maize seed sections,

successfully visualizing diverse medium-size molecules and acquiring high-quality MS/MS spectra for these compounds.

Introduction

Matrix-assisted laser desorption/ionization-mass spectrometry (MALDI-MS) is widely used for various biological applications, including analysis of small molecule drugs,[1] lipids,[2] peptides and proteins,[3] oligosaccharides,[4] and polymers.[5] Recently, it has become especially popular for *in situ* molecular imaging of tissues.[6] In a typical MALDI-MS experiment, choice of matrix plays a crucial role in determining the types of compounds that can be ionized and detected. While the exact mechanism of how matrices affect desorption/ionization is still not fully understood,[7] it is well known that different matrices preferentially ionize different classes of compounds. For example, trihydroxyacetophenone (THAP) is well known to be useful for studying oligosaccharides, while α-cyano-4-hydroxycinnamic acid (CHCA) is commonly used for studying peptides and small proteins.[6] In addition to traditional organic matrices, many nanoparticles (NPs) have recently proven useful as matrices, but they also demonstrate some selectivity.[8-10]

Due to this matrix selectivity, it is challenging to obtain a complete metabolic profile of a sample in a single MALDI-MS analysis. Recently, we have shown multiple matrices can be used to visualize wide classes of compounds in MALDI-mass spectrometry imaging (MSI) by using different matrices for consecutive tissue sections.[11] While this approach allows for more comprehensive metabolite coverage, it comes at the cost of increased time and sample consumption. For high-throughput analysis, it would be desirable to develop a methodology that allows for comprehensive metabolite coverage in a single analysis.

Various combinations of two organic matrices have been used to overcome this limitation. A binary mixture of 2,5-dihydroxybenzoic acid (DHB) and CHCA is the most common example, especially for the analysis of phospholipids[12], peptides, and glycoproteins[13]; this mixture is now sold as 'universal MALDI matrix' by Sigma. Other organic matrix mixtures have also been formulated for the analysis of proteins[14], carbohydrates and glycoproteins[15], and small drugs and amino acids.[16]

More recent studies have investigated combining nanoparticle and organic matrices. Functionalized magnetic NPs, with CHCA or DHB conjugated to Fe_3O_4 NPs through polymerized SiO_2, were demonstrated to dramatically reduce the low mass matrix peaks[17], while at the same time enhancing ion signals with minimal fragmentations in small molecule analysis[18]. A hybrid matrix of 9AA-SiO_2 NPs has been used for homogeneous matrix application, where 9AA can be released from the NPs with exposure to NH_3(g) and act as a matrix.[19] Most recently, a combination of 9AA and carbon nanodots was utilized for the analysis of small molecules.[20] These organic-inorganic matrix studies have been mostly focused on small molecules (i.e., MW <~600 Da) in contrast to organic matrices that are commonly used for medium-sized (say, MW of 600-2,000 Da) or macromolecules (> 2 kDa).

Triacylglycerol (TG) is a neutral lipid that is stored as oil bodies in plant cells,[21] and in adipose tissue of animals.[22] It is a final destination for long-term energy storage, to be used when simple energy sources are not available, such as during seed germination or animal starvation. Phosphatidylcholine (PC) plays a key role in the TG biosynthetic pathway in plants,[23] and simultaneous detection of both classes of compounds is crucial for a better understanding of the underlying biology. DHB is commonly used for the MALDI-MS analysis of TGs, which are detected as alkali ion adducts.[24] However, it is well known that

TGs are highly prone to suppression by PC present in samples. The fact that DHB is also highly efficient at ionizing PC (also commonly detected as alkali cation adducts[24]) often makes it difficult to obtain a complete lipid profile for a sample.[25, 26] This is a very challenging problem in MALDI-MS, especially MALDI-MS imaging, because of the lack of chromatographic separation.

Recently, our group performed a large-scale matrix screening of thirteen different non-functionalized NPs, testing their laser desorption/ionization efficiency for two-dozen small metabolites and lipids.[27] In this study, Fe_3O_4 NPs were found to have an extraordinary MALDI efficiency for triacylglycerol (TG) species. While the Fe_3O_4 NP matrix was efficient for the detection of TG species, it showed very poor efficiency for the analysis of PCs. It is in contrast to DHB, which is efficient for PC analysis but not for TGs in the presence of PCs. In a separate study, we also have demonstrated the effectiveness of Fe_3O_4 NPs for the analysis of TG and DHB for PC in MALDI-MSI of a germinated maize seed.[11]

In the present work, we propose a simple binary matrix mixture comprised of non-functionalized inorganic Fe_3O_4 NPs and organic DHB as a new binary matrix that can help alleviate TG suppression by PC, and therefore efficiently desorb and ionize both PC and TG species in the same sample. The binary matrix was first demonstrated for the analysis of standard mixtures, and then applied to MALDI-MSI of a maize seed cross-section. To our surprise, we found the binary matrix not only is efficient for simultaneous visualization of PC and TG, but also effective at detecting various other classes of lipid species. Furthermore, the binary matrix demonstrates a synergy effect to ionize very large polysaccharides that are not efficiently detected by either of the individual matrices alone.

Experimental

Materials

2,5-dihydroxybenzoic acid (98%), chloroform (LC-MS grade), isopropanol (LC-MS grade), and glyceryl tripalmitate (approx. 99%) were purchased from Sigma-Aldrich (St. Louis, MO, USA). Gelatin from porcine skin (300 bloom) was purchased from Electron Microscopy Sciences (Hatfield, PA, USA). Phospholipid mixture [L-α-Phosphatidylcholine, 95% (Soy)] was purchased from Avanti Polar Lipids, Inc. (Alabaster, AL, USA). Maltodextrin-dextrose equivalent 4.0-7.0 was purchased from Carbosynth (from maize, CAS No: 9050-36-6; Berkshire, UK). Certified ACS Pellets of potassium hydroxide were purchased from Fisher Scientific (Hampton, NH, USA). Sodium acetate (99%) was purchased from Alfa Aesar (Ward Hill, MA, USA). B73 inbred corn seeds were obtained from Dr. Marna Yandau-Nelson at Iowa State University. Iron oxide nanoparticles were synthesized as has been previously described.[28]

Instrumentation and Software

All samples were run on a MALDI-linear ion trap (LIT)-Orbitrap mass spectrometer (MALDI-LTQ-Orbitrap Discovery; Thermo Finnigan, San Jose, CA) that has been modified to incorporate an external, frequency-tripled, 355 nm Nd:YAG laser (UVFQ; Elforlight, Ltd., Daventry, UK). Data collection and imaging runs were set up using Xcalibur software (Thermo), and data were analyzed using Xcalibur and ImageQuest (Thermo) software. Image generation parameters including *m/z* values, mass tolerance values, and maximum and minimum intensity values can be found in Table S2.

Standard Analysis

Stock solutions of 5mM glyceryl tripalmitate (TG 16:0/16:0/16:0) and 100 mM, 10 mM, and 1 mM 95% PC Soy extract (average MW is treated as 758.07 Da for the concentration calculation, per manufacturer specifications) were prepared in chloroform. For every standard sample, 20 µL of 5mM TG 48:0 was mixed with a combination of varying amounts of DHB and/or Fe_3O_4 nanoparticles in isopropanol, PC extract in chloroform, and sodium acetate in methanol to give a final volume of 1000 µL. In all samples, DHB had a final concentration of 10 mM, Fe_3O_4 had a final concentration of 5 mM, and sodium acetate had a final concentration of 10 mM. The resulting concentration of TG 48:0 was 100 µM and the PC concentration was varied from 0 to 2000 µM.

500 µL of each resulting matrix/standard solution was sprayed onto a stainless steel slide at 50 µL/min using an oscillating capillary nebulizer created from a modified airbrush.[29] After spraying, each sample was analyzed in positive ion mode using a raster step of 75 µm, one MS scan/step, and 10 laser shots/scan for the *m/z* range of 500-1000, while changing a laser energy by 0.5% per minute for 83-92% (0.4 - 2.3 µJ). Laser spot size varies from 12 to 30 µm depending on the laser energy.

Corn Seed Germination

A B73 corn seed was imbibed by placing it in a glass scintillation vial with deionized water and shaking for 10 minutes at 300rpm. After imbibing, the seed was placed on moist filter paper in a plastic petri dish with the embryo side of the seed facing down. The petri dish was covered and the seed was allowed to germinate in a climate-controlled greenhouse with water periodically added to keep the filter paper moist, but without standing water.

After germinating for 27 hours, the seed was removed from the greenhouse. A razor blade was used to cut the seed longitudinally approximately halfway between the center and edge. The seed was then immediately flash frozen in liquid nitrogen to prevent metabolite turnover.

Tissue Harvesting and Preparation

Sample preparation for MALDI-MSI of plant tissues can be found in our recent protocol paper[30] and is briefly described below. Initially, frozen samples are placed with the cut face down in a plastic cryo-mold. Then, a warm, aqueous, 10% w/v gelatin solution is poured into the cryo-mold to surround the sample. The mold is immediately floated on liquid nitrogen and held there until the gelatin becomes ~50% opaque (tissues completely frozen on liquid nitrogen have been found to be prone to cracking). The frozen gelatin medium was then placed into a pre-chilled cryostat at -22 °C and allowed to thermally equilibrate. Finally, the gelatin block was removed from the cryo-mold, mounted on a cryostat chuck, and sectioned at a thickness of 10 μm in the area of morphological interest. Sections were captured intact using adhesive tape windows (Leica Biosystems, Buffalo Grove, IL, USA). The tape windows with tissue sections were then taped face-up on pre-chilled glass slides to prevent thawing, and stored at -80 °C.

Serial tissue sections were selected for analysis. The sections were lyophilized on a chilled aluminum block under vacuum in order to prevent condensation and metabolite delocalization as the samples were brought to room temperature for preparation.

On-Tissue Laser Optimization

For on-tissue optimization, the concentration of iron oxide was held constant at 5 mM in isopropanol. The concentration of DHB was optimized between 60-100 mM in isopropanol. The binary matrix was prepared by mixing 750 μL of 10 mM Fe_3O_4 with 750 μL of varying concentrations of DHB in isopropanol. No additional salt was added to matrices for tissue imaging due to the fact that sufficiently high levels of potassium are present in most plant organs, including seeds. As such, most analytes were observed as potassium ion adducts.

One milliliter of the resulting matrix solutions was sprayed over the tissue sections using a homemade oscillating capillary nebulizer. Laser energy optimization was performed on the embryo region of the corn seed (the area of the seed known to contain PCs and TGs; a labeled optical image of maize seed can be found in Figure 4A) for the *m/z* range of 500-1000 in positive ion mode with a raster step size of 75 μm while increasing the laser energy from 84 to 91% (0.6 – 2.2 μJ) by 0.5% per minute. The laser energy providing the best signal levels for compounds of interest was selected for imaging runs.

Mass Spectrometry Imaging Data Acquisition

Three serial sections were analyzed using a 4-step multiplex MS imaging strategy.[11, 31] In the first and third steps, a high-resolution Orbitrap scan was obtained from *m/z* 50-800 and *m/z* 600-1600, respectively. For the second and fourth steps, data-dependent MS/MS scans were obtained with the ion trap. The laser energy used for the imaging runs was selected based on the previously described on-tissue optimization.

For the data-dependent MS/MS scans, a parent mass list consisting of 139 compounds was imported to the Xcalibur data acquisition program (Thermo) to preferentially acquire MS/MS of known compounds of interest. The data acquisition method was setup to perform MS/MS on the most abundant ion in the scan if no masses from the precursor mass list were present. Collision energies were pre-assigned depending on precursor mass range to help with optimal fragmentation; collision energy of 125, 75, and 35 for *m/z* 50-300, *m/z* 300-600, and above *m/z* 600, respectively. For compounds not on the precursor mass list, default settings were used (collision energy of 35). Collision duration of 30 ms and an isolation width of 1.5 Da were used in all cases. Dynamic exclusion was also employed to minimize the repeated acquisition of the same MS/MS scans using a repeat count of one and exclusion duration of 50 seconds.

Polysaccharide Standard Analysis

For polysaccharide standard analysis, solutions were made at a final concentration of 1 mg/mL maltodextrin-dextrose equivalent, 50 mM potassium hydroxide, and either 70 mM DHB, 5 mM Fe_3O_4 nanoparticles, or a binary mixture with final concentrations of each matrix the same as when used individually. One milliliter of each of the three solutions was sprayed on separate glass slides and analyzed using a laser ramping procedure for 86 - 91% (1.1 - 2.2 μJ) laser energy by increasing 0.5% every minute. MS spectra were acquired with Orbitrap and analyzed using Xcalibur software.

Results and Discussion

Binary Matrix for Standard Mixture Analysis

A mixture of DHB and Fe_3O_4 NPs is presented here as a binary matrix to minimize TG ion suppression by PCs, thereby allowing for the simultaneous detection of both TG and PC species in a single analysis. As an initial proof of concept experiment, TG ion signals were monitored in the presence of varying amounts of PC standard and a matrix of either DHB, Fe_3O_4 NPs, or a mixture of the two matrices. Because the optimum laser energy is slightly different for each matrix, the spectra were collected by increasing the laser energy every minute while rastering across the sample area. After data collection, the spectra were averaged at each laser energy (~66 spectra per energy). Then, the highest signal of sodiated TG, $[TG\ 48{:}0 + Na]^+$ at *m/z* 829.72, was used to create a plot at each PC concentration, as shown in Figure 1. Sodium acetate was added at a final concentration of 10 mM in all samples to provide sufficient cations and reduce signals from other cation adducts. The TG concentration was maintained at 0.1 mM, and the maximum PC concentration used was 2 mM; thus, sodium adduct formation of lipids should not be limited by the availability of sodium ions.

Figure 1 shows that the TG signal declines rapidly as the concentration of PC increases when using DHB as a matrix, down to ~10% of the original TG signal at 2000 μM PC concentration. For Fe_3O_4 NPs, the TG signal increases with a small amount of PC added, before decreasing at high concentrations of PC. The TG signal with Fe_3O_4 NPs however does not decrease as much as with DHB alone, and is maintained at ~44% of the TG only signal in the 2000 μM PC sample. The TG signal in the binary matrix meanwhile demonstrates behavior in-between the two matrices. Addition of 10 μM PC causes a slight decrease in TG signal, before a slight increase at 20 µM PC concentration. Then, the TG signal steadily decreases with increasing PC concentration. At the final 2000 µM PC concentration, the binary matrix maintains TG signal at ~32% of the original TG only signal, which is three times better than DHB alone.

It should be mentioned that a simple 2:1 molar mixture of DHB and Fe_3O_4 NPs was used as the binary matrix for this standard analysis, with a concentration of 10 mM and 5 mM, respectively. While not pursued in this proof of concept experiment, further optimization can be performed for the matrix ratio in order to achieve optimum signal levels for both classes of compounds depending on the amount of TG and PC present, as was done in the following tissue analysis for MALDI-MSI of a maize seed.

Binary Matrix Applied for Tissue Analysis

Encouraged by the success in the proof of concept experiment on standards, we applied the binary matrix to MS imaging of a germinated maize seed. Preliminary tests were performed to find optimum DHB and Fe_3O_4 NP concentrations for maize seed analysis, and we decided to use a DHB concentration of 70 mM and Fe_3O_4 NP concentration of 5 mM both as a single matrix and in the binary mixture. After laser energy optimization as described in the experimental section, a MALDI-MSI data set was acquired for three consecutive maize seed sections using each matrix at the optimum laser energy using a four step multiplex MS imaging setup (Figure S1), similar to our previous work.[11, 31] In multiplex MS imaging, each raster step is divided into smaller spiral steps with separate mass spectral scan events acquired for each spiral step. Using this four-step data acquisition with a hybrid MALDI-ion trap-Orbitrap mass spectrometer, we can separately acquire mass spectra for the low mass range (*m/z* 50-800) and high-mass range (*m/z* 600-1600) using an Orbitrap high-resolution mass spectrometer, as well as corresponding data-dependent MS/MS scans using an ion trap mass spectrometer, all in a single MALDI-MSI experiment.

Figure 2 compares representative mass spectra from each matrix averaged over the embryo region of the seed, where TG and PC are most abundant (see Figure 4A for the anatomy of maize seed). As expected, DHB efficiently ionized PCs (dark circle) but TGs (dark square) are almost undetectable, while Fe_3O_4 NPs were efficient for TGs but not as efficient for PCs. In contrast, the binary matrix could efficiently ionize both PCs and TGs, maintaining essentially the same ion signals as in DHB or Fe_3O_4 NPs. Major PCs observed at *m/*z 796 and 822 correspond to $[PC\ 34:2+K]^+$ and $[PC\ 36:3+K]^+$, respectively. Significant peaks observed nearby at *m/z* 798, 820, and 824 are PCs with varying degrees of unsaturation, $[PC\ 34:1+K]^+$, $[PC\ 36:4+K]^+$, and $[PC\ 36:2+K]^+$, respectively. Trimethylamine loss ($-N(CH_3)_3$) from the headgroup of PCs is found in all three matrices, such as *m/z* 737, 761, and 763, corresponding to the 59 Da loss of *m/z* 796, 820 and 822, respectively. PCs are the dominant species in DHB and the binary matrix, but in Fe_3O_4 NPs, they are only about 10-15% of the base peak, even for the most abundant species. In Fe_3O_4 NPs and the binary matrix, two distinct series of TGs are observed in the *m/z* range around 893 and 917, corresponding to $[TG\ 52:x+K]^+$ (x =4-3) and $[TG\ 54:y+K]^+$ (y = 6-4), respectively. TGs are also found in DHB, but in very low abundance, ~0.1% of the base peak.

Three intense peaks (dark triangle) are observed in the PC range of the spectrum for Fe_3O_4 at *m/z* 792.434, 816.434, and 818.451, but have significantly lower mass defects than typical PC species. These peaks are assigned as dipotassiated phosphatidylethanolamines (PEs), $[PE\ 34:2 + 2K -H]^+$, $[PE\ 36:4 + 2K -H]^+$, and $[PE\ 36:3 + 2K -H]^+$, respectively, with mass errors less than 2 ppm (Table S1). These assignments are also confirmed by MS/MS shown in Figure S2, and similar dicationized PE species have been reported previously.[32] Other peaks with similarly low mass defects are observed at *m/z* 873.489 and 911.445, and are identified as phosphatidylinositol (PI) species $[\text{PI } 34{:}2+\text{K}]^+$ and $[\text{PI } 34{:}2+2\text{K-H}]^+$, respectively, based on accurate mass and MS/MS (Figure S2). PE and PI are most commonly detected in negative ion mode, and dipotassiated phospholipids are not commonly found with DHB, although a low amount of $[\text{PI } 34{:}2+2\text{K-H}]^+$ is seen at *m/z* 911.

Two series of peaks are observed around *m/*z 950 and 980 in the Fe_3O_4 and binary spectra (dark cross). While the MS/MS spectra were not informative for the identification of these peaks, accurate mass analysis tentatively identified them as the potassium adduct of digalactosyldiacylglycerol (DGDG) lipid species of varying unsaturations, all within 1ppm mass error (Table S1). We also could observe suspected monogalactosyldiacylglycerol (MGDG) species in the Fe_3O_4 and binary spectra (not labeled), although in very low abundance. This finding is not surprising considering both MGDG and DGDG are known to be abundant in plants, comprising ~80% of thylakoid lipids.[33] Additionally, MGDG and DGDG are neutral lipids, similar to neutral TG lipids, which Fe_3O_4 NPs seem to very effectively desorb and ionize.

Combined all together, the binary matrix is efficient in ionizing a wide class of lipids, including cationic lipids such as PC, neutral lipids such as TG, DGDG and MGDG, and anionic lipids such as PE and PI. Figure 3 compares the effectiveness of MALDI-MS for various lipid classes between the three matrices for the maize seed section. For this analysis, the ion signals of intact species from each class were summed together and normalized to those of binary matrix. For PE, TG, and DGDG, the binary matrix is less effective than Fe_3O_4 NPs, but still able to maintain more than 40% of the signals with Fe_3O_4 NPs. Meanwhile, for PI and PC species, the binary matrix is comparable or even slightly better than the optimum individual matrix. Lastly, for large polysaccharide compounds, the binary matrix shows much higher abundance levels compared to either of the individual matrices, as will be further discussed in the next section. In total, these results indicate that the binary matrix provides effective MALDI-MS efficiencies for a wide range of these medium-size molecules. MS imaging data discussed in the next section is also consistent with this trend. Similar trends were also seen in a replicate experiment, as shown in Figure S3.

MALDI-MS Imaging with Binary Matrix

To compare the effectiveness of the binary matrix in MALDI-MSI, MS images were generated for various lipid compounds, along with other selected compounds, and compared between three matrices as shown in Figure 4B. It should be noted that no normalization was applied to generate these images, so the ion intensity scales can be directly compared; however, the ion images generated with normalization to the total ion count (TIC) showed essentially the same images (Figure S4). The optical image is shown in Figure 4A for the anatomy of this 27 hr-germinated maize seed section. The two major components are the endosperm and the embryo. The endosperm is a storage area of starch that will be used as energy during seed development. The embryo contains developing tissues of the seed, including the radicle (initial root) and cotyledon (first leaf, not seen here). The scutellum is an oil storage area of the embryo that is metabolically active throughout germination.[21]

The images in Figure 4B confirm the trends discussed in the mass spectra of Figure 2 and class comparison of Figure 3. Namely, DHB shows high quality images for PCs but not TGs, Fe_3O_4 NPs show high quality images for TGs but not PCs, and the binary mixture presents high quality images for both PCs and TGs. Additionally, the binary matrix shows high quality images for proline, as with DHB, and PE, PI, and DGDG, as with Fe_3O_4 NPs. The localizations of these metabolite molecules are also consistent between single matrices and the binary matrix. PC, PE, PI and DGDG are observed throughout the entire embryo, including the radicle, while TG and proline are observed in the scutellum of the seed. Similar results are obtained in a replicate experiment as shown in Figure S5.

A particularly interesting observation arises upon examination of large polysaccharide species. As shown in the images for Hex_6 in Figure 4B, both Fe_3O_4 and DHB show no apparent signal anywhere in the seed. However, the binary matrix shows a clearly visible Hex_6 polysaccharide in the endosperm of the seed. The localization of Hex_6 is consistent with the fact that large starch molecules in the endosperm are broken down to smaller size sugars by amylases before they are transported to embryo.[21] Closer investigation of the mass spectra in the endosperm area shows no signal with Fe_3O_4 for this compound, while DHB does have signal, but at levels ~15% of those in the binary matrix.

To further investigate this phenomenon, images were generated for several large-size polysaccharide species, shown in Figure 5. The result is consistent with that in Figure 4B, in that the binary matrix outperforms each of the single matrices for effective desorption/ionization and visualization of these large polysaccharide compounds. Similar results were also obtained for a replicate experiment (see Figure S6A). The sum of these polysaccharide ion signals is also much greater with the binary matrix than with the individual matrices as we have shown in Figures 3 and S3. We have used slightly higher laser energy for the binary matrix [LP = 89% (1.7 μJ)] than DHB [LP = 87% (1.3 μJ)] and it is possible that a higher laser energy would cause more efficient desorption of large oligosaccharides. To test such a possibility, an experiment was performed on a separate seed section with only DHB as a matrix at the same laser energy as the binary mixture. However, the higher laser energy does not help to improve desorption and ionization of these compounds by DHB as shown in Figure S6B.

This suggests that the binary matrix not only yields results similar to a simple addition of the two matrices, but also has a synergistic effect, wherein the two matrices work together to efficiently ionize some compounds. To confirm this unusual behavior, a standard analysis was performed for a maltodextrin mixture using each of the three matrices and a laser ramping procedure similar to that in Figure 1. As shown in Figure 6, both DHB and Fe_3O_4 nanoparticles show little to no signal overall other than some minor noise peaks. Meanwhile, the binary matrix is able to effectively ionize maltodextrin compounds similar to those on the maize seed tissues, as well as an unidentified class of compounds conjugated with a series of hexose units. These results further validate the synergy effect for polysaccharides using the binary matrix, as seen on the maize seed tissue sections. Interestingly, this experiment failed when performed on a stainless steel MALDI plate, suggesting heat dissipation might interfere with the synergy effect.

One possible explanation on this synergy effect would be specific interaction between DHB and Fe_3O_4 NPs in the mixture. Metal oxides are basic and they may interact with DHB to form functionalized nanoparticles. UV-Visible absorption spectra were measured for each matrix and the binary matrix (Figure S7); however, we do not see any apparent change in the UV-Visible spectrum of the binary matrix such as the shift of absorption maximum or appearance of new peaks. Hence, it is very unlikely there exists direct interaction between DHB and nanoparticles, at least in measurable amount.

Further study is necessary to understand the specific origin of the synergy effect. However, our current hypothesis is that DHB produces microcrystals on the tissue surface to effectively incorporate non-volatile, large size polysaccharides, while high temperatures generated by nearby Fe_3O_4 NPs assist their effective desorption and ionization. More specifically, the decomposition of microcrystals would be necessary in the gas phase after desorption, so that analytes can fly into the mass spectrometer. Trimpin et al. demonstrated the importance of heating to generate multiply charged protein ions in atmospheric pressure MALDI-MS.[34] Metal oxide NP matrices have a high heat capacity and low heat conductivity, and therefore produce high temperatures when irradiated by the laser.

The advantage of this synergy effect is not limited to providing high quality ion images for polysaccharides, as it also is able to provide high quality MS/MS spectra. Figure 7 compares MS/MS spectra of *m/z* 1011.3, corresponding to $[Hex_6+K-H_2O]^+$, obtained from multiplex MS imaging data sets with each of the three matrices. The MS/MS spectrum from the binary matrix shows clear structural information of typical polysaccharides; i.e., the loss of one and two hexose units as well as a water loss. In contrast, the MS/MS spectrum from DHB shows one hexose loss and a water loss but also multiple unassignable fragments from MS/MS of contamination peak(s), and the MS/MS spectrum from Fe_3O_4 NPs shows predominantly noise peaks.

The high quality MS/MS spectra from the binary matrix is not limited to large oligosaccharides, but also applies to broad metabolite coverage thanks to its high efficiency for a wide range of compounds (Figure 3). To determine how many high quality MS/MS spectra can be obtained by the binary matrix compared to the individual matrices, a filtering process described previously[11] was employed to calculate the total number of high-quality MS/MS spectra. Out of ~10,000 MS/MS spectra in each multiplex MS data set, the binary matrix produced 5,026 high-quality MS/MS spectra from 79 unique compounds, while DHB collected 4,458 from 60 unique compounds, and Fe_3O_4 NPs collected only 2,915 from 64 unique compounds. In terms of lipids, specifically those referenced in Table S1, the binary matrix produced a total of 2,171 high-quality MS/MS, while DHB and Fe_3O_4 NPs had 1,825 and 1,755, respectively. These results suggest that the binary matrix could not only detect more compounds, but also obtain more structurally informative MS/MS to aid in their identification.

Conclusions

There are not many efficient matrices available for medium-size analytes in the mass range around *m/*z 600-2,000, and the matrices that do exist for this range are often highly selective. For example, DHB and DAN are efficient for cationic lipids in positive mode and anionic lipids in negative mode, respectively, and THAP is efficient for large oligosaccharides. DHB also works for neutral lipids such as TG and DGDG, but is very inefficient in the presence of cationic PCs. In this study, we discovered that a new binary matrix of DHB and Fe_3O_4 NPs is very efficient for a wide range of medium-size molecules, allowing for the simultaneous detection of cationic and anionic phospholipids such as PC, PE, and PI, neutral glycerolipids such as TG and DGDG, and highly polar oligosaccharides.

The binary matrix was successfully applied for a lipid standard mixture and MS imaging of maize seed cross-sections, demonstrating the efficient detection of TG in the presence of PC, along with visualization of various medium-size compounds. Organic-inorganic binary matrices have been previously demonstrated by several researchers[17, 18, 20]; however, they were developed for the analysis of small molecules, and this is the first effort for the analysis of medium-size molecules. Furthermore, the binary matrix employed here does not require special functionalization unlike most other organic-inorganic matrices, but is made of a simple mixture between DHB and non-functionalized Fe_3O_4 NPs, for which the ratio can be tuned, if necessary, to enhance specific compounds of interest versus another. Additionally, non-functionalized Fe_3O_4 NPs used here can be easily synthesized in a few straightforward steps.[28]

The high MALDI efficiency for large polysaccharides by the new binary matrix is especially unique, and could not be achieved by DHB or Fe_3O_4 NPs alone. The origin of this synergy effect is yet to be explored, but we hypothesize that DHB produces microcrystals that effectively incorporate large polysaccharides, which are then effectively desorbed and decomposed in the high temperature laser plume provided by Fe_3O_4 NPs. Further exploration and utilization of this unusual organic-inorganic matrix will expand the utilization of MALDI-MSI for various chemical compounds, and may even lead to the wide adoption of MALDI-MS for metabolomics and lipidomics, which currently is mostly performed by GC-MS and LC-MS.

Acknowledgments

This work was supported by the US Department of Energy (DOE), Office of Basic Energy Sciences, Division of Chemical Sciences, Geosciences and Biosciences. The Ames Laboratory is operated by Iowa State University under DOE Contract DE-AC02-07CH11358.

References

1. S. Notari, C. Mancone, M. Tripodi, P. Narciso, M. Fasano and P. Ascenzi, *Journal of Chromatography B*, 2006, **833**, 109-116.
2. J. Schiller, R. Süß, J. Arnhold, B. Fuchs, J. Lessig, M. Müller, M. Petković, H. Spalteholz, O. Zschörnig and K. Arnold, *Progress in lipid research*, 2004, **43**, 449-488.
3. P. Chaurand, F. Luetzenkirchen and B. Spengler, *Journal of the American Society for Mass Spectrometry*, 1999, **10**, 91-103.
4. Y. Mechref, M. V. Novotny and C. Krishnan, *Analytical chemistry*, 2003, **75**, 4895-4903.
5. M. W. Nielen, *Mass Spectrometry Reviews*, 1999, **18**, 309-344.
6. E. M. Weaver and A. B. Hummon, *Advanced drug delivery reviews*, 2013, **65**, 1039-1055.
7. M. Glückmann, A. Pfenninger, R. Krüger, M. Thierolf, M. Karasa, V. Horneffer, F. Hillenkamp and K. Strupat, *Int. J. Mass spectrom.*, 2001, **210**, 121-132.
8. S. N. Jackson, M. Ugarov, T. Egan, J. D. Post, D. Langlais, J. Albert Schultz and A. S. Woods, *J. Mass Spectrom.*, 2007, **42**, 1093-1098.
9. L. Hua, J. Chen, L. Ge and S. N. Tan, *J. Nanopart. Res.*, 2007, **9**, 1133-1138.
10. J. A. McLean, K. A. Stumpo and D. H. Russell, *Journal of the American Chemical Society*, 2005, **127**, 5304-5305.
11. A. D. Feenstra, R. L. Hansen and Y. J. Lee, *Analyst*, 2015, **140**, 7293-7304.
12. S. R. Shanta, L.-H. Zhou, Y. S. Park, Y. H. Kim, Y. Kim and K. P. Kim, *Anal. Chem.*, 2011, **83**, 1252-1259.
13. S. Laugesen and P. Roepstorff, *J. Am. Soc. Mass Spectrom.*, 2003, **14**, 992-1002.
14. S. Khatib-Shahidi, M. Andersson, J. L. Herman, T. A. Gillespie and R. M. Caprioli, *Anal. Chem.*, 2006, **78**, 6448-6456.
15. N.-Y. Hsu, W.-B. Yang, C.-H. Wong, Y.-C. Lee, R. T. Lee, Y.-S. Wang and C.-H. Chen, *Rapid Commun. Mass Spectrom.*, 2007, **21**, 2137-2146.
16. S. R. Shanta, T. Y. Kim, J. H. Hong, J. H. Lee, C. Y. Shin, K.-H. Kim, Y. H. Kim, S. K. Kim and K. P. Kim, *Analyst*, 2012, **137**, 5757-5762.
17. P.-C. Lin, M.-C. Tseng, A.-K. Su, Y.-J. Chen and C.-C. Lin, *Anal. Chem.*, 2007, **79**, 3401-3408.

18. M.-C. Tseng, R. Obena, Y.-W. Lu, P.-C. Lin, P.-Y. Lin, Y.-S. Yen, J.-T. Lin, L.-D. Huang, K.-L. Lu, L.-L. Lai, C.-C. Lin and Y.-J. Chen, *J. Am. Soc. Mass Spectrom.*, 2010, **21**, 1930-1939.
19. P.-H. Li, S.-Y. Huang, Y.-C. Chen and P. L. Urban, *Rsc Advances*, 2013, **3**, 6865-6870.
20. Y. Chen, D. Gao, H. Bai, H. Liu, S. Lin and Y. Jiang, *Journal of The American Society for Mass Spectrometry*, 2016, 1-9.
21. J. D. Bewley, K. Bradford and H. Hilhorst, *Seeds: physiology of development, germination and dormancy*, Springer Science & Business Media, 2012.
22. G. F. Gibbons, K. Islam and R. J. Pease, *Biochimica et Biophysica Acta (BBA)-Molecular and Cell Biology of Lipids*, 2000, **1483**, 37-57.
23. P. D. Bates and J. Browse, *The Plant Journal*, 2011, **68**, 387-399.
24. K. A. Zemski Berry, J. A. Hankin, R. M. Barkley, J. M. Spraggins, R. M. Caprioli and R. C. Murphy, *Chemical reviews*, 2011, **111**, 6491-6512.
25. X. Lou, J. L. van Dongen, J. A. Vekemans and E. Meijer, *Rapid Commun. Mass Spectrom.*, 2009, **23**, 3077-3082.
26. B. Emerson, J. Gidden, J. O. Lay and B. Durham, *Journal of lipid research*, 2010, **51**, 2428-2434.
27. G. B. Yagnik, R. L. Hansen, A. R. Korte, M. D. Reichert, J. Vela and Y. J. Lee, *Analytical Chemistry*, 2016.
28. A. T. Klein, G. B. Yagnik, J. D. Hohenstein, Z. Ji, J. Zi, M. D. Reichert, G. C. MacIntosh, B. Yang, R. J. Peters and J. Vela, *Anal. Chem.*, 2015, **87**, 5294-5301.
29. Y. Chen, J. Allegood, Y. Liu, E. Wang, B. Cachón-González, T. M. Cox, A. H. Merrill and M. C. Sullards, *Anal. Chem.*, 2008, **80**, 2780-2788.
30. A. R. Korte, G. B. Yagnik, A. D. Feenstra and Y. J. Lee, *Mass spectrometry imaging of small molecules*, 2015, 49-62.
31. D. Perdian and Y. J. Lee, *Anal. Chem.*, 2010, **82**, 9393-9400.
32. K. A. Al‐Saad, V. Zabrouskov, W. F. Siems, N. R. Knowles, R. M. Hannan and H. H. Hill, *Rapid Commun. Mass Spectrom.*, 2003, **17**, 87-96.
33. M. A. Block, A.-J. Dorne, J. Joyard and R. Douce, *Journal of Biological Chemistry*, 1983, **258**, 13281-13286.
34. S. Trimpin, E. D. Inutan, T. N. Herath and C. N. McEwen, *Molecular & Cellular Proteomics*, 2010, **9**, 362-367.

Figures

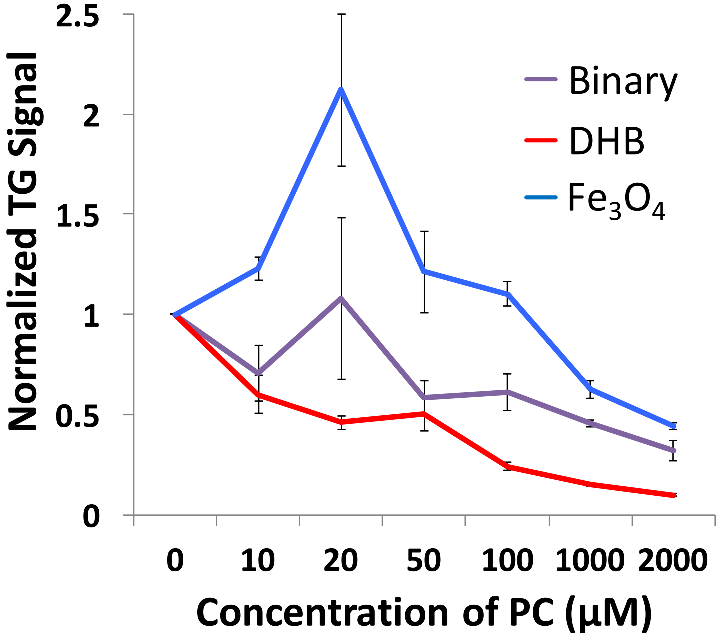

Figure 1. Effect of PC concentration on TG signals. TG concentration is maintained at 100 μM as PC concentration increases from zero to 2 mM. Y-scale represents the ion signal for the sodium ion adduct of TG 48:0, normalized to that of TG only sample in each matrix. Error bars represent the standard error from 3 replicates.

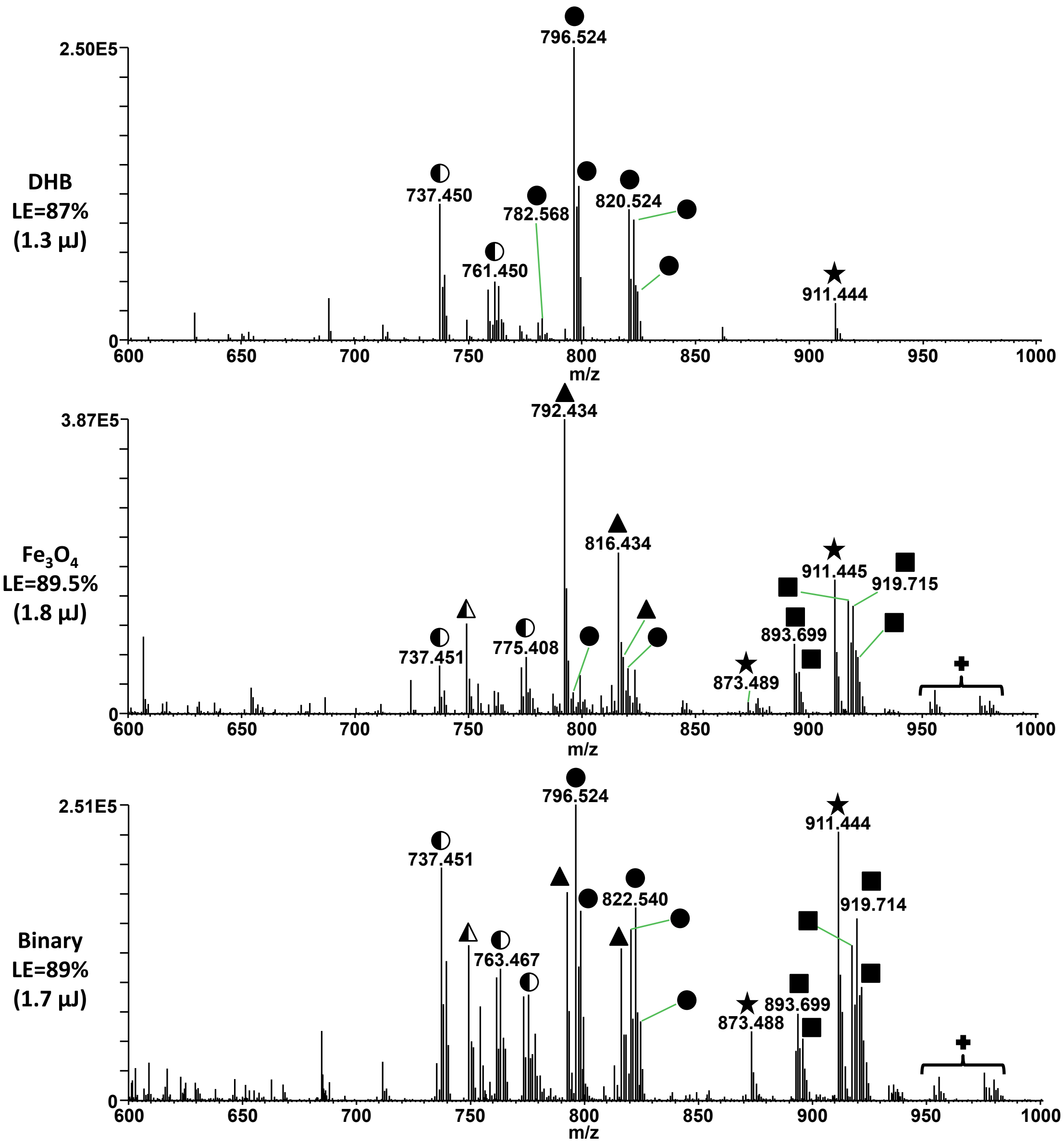

Figure 2. Mass spectra of maize seed sections averaged over the embryo region obtained with three matrices. LE denotes the laser energy used for each sample. Legend: solid circle=PC, half-filled circle=PC Fragment, solid box=TG, solid triangle=PE, half-filled triangle=PE Fragment, star=PI, cross=digalactosyldiacylglycerol (DGDG). Assignments of the labeled peaks are listed in Table S1.

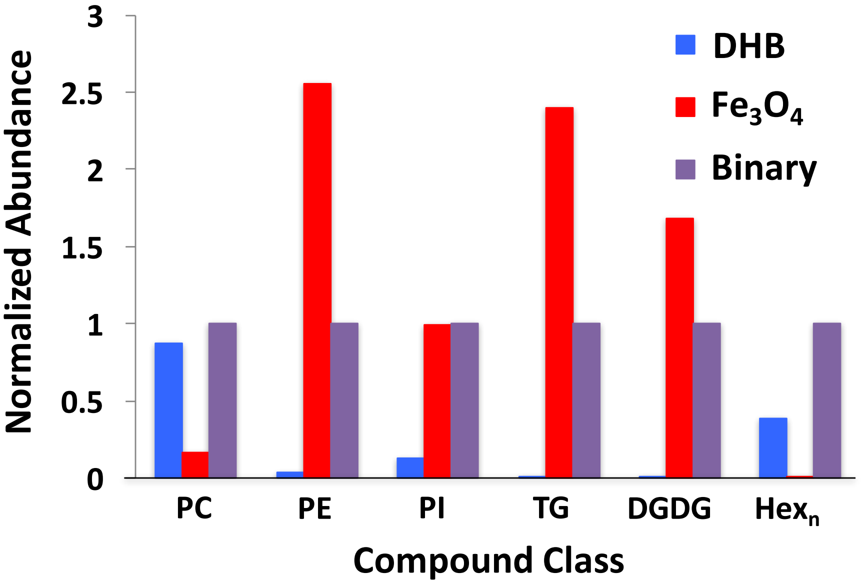

Figure 3. Comparison of compound class abundance between three matrices for a maize seed section. Ion intensities from a representative area of the seeds were summed for each lipid class and normalized to the summed intensity for the binary matrix. Summed ion intensities of oligosaccharides shown in Figure 5 are also compared.

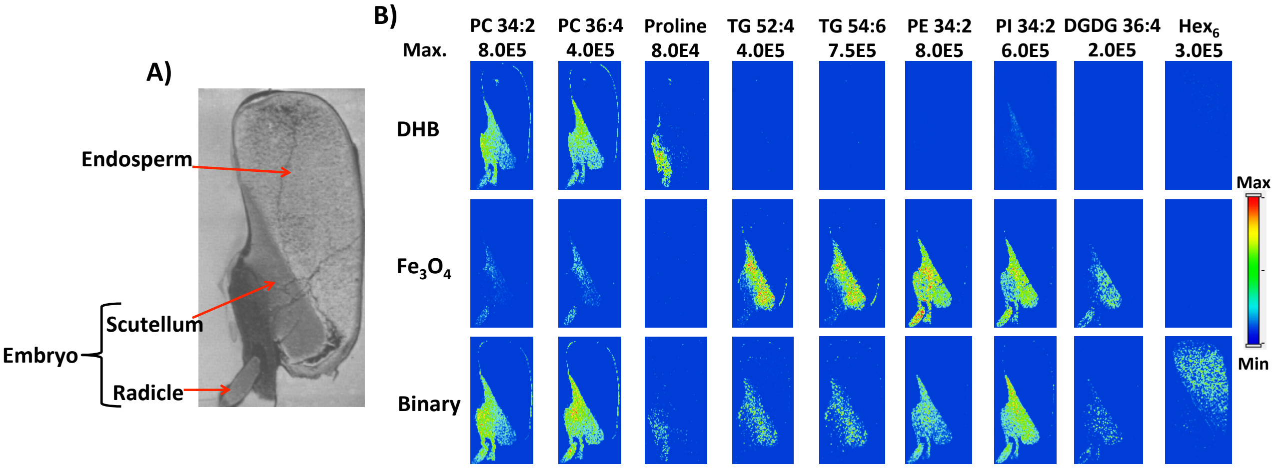

Figure 4. A) Optical image of a maize seed section with major morphological features labeled. B) MS images from consecutive maize seed sections for selected compounds with DHB, Fe_3O_4 NPs, and the binary matrix. Images are generated without normalization. Laser energies are the same as those referenced in Figure 2. Details of peak assignment and imaging parameters are summarized in Table S2.

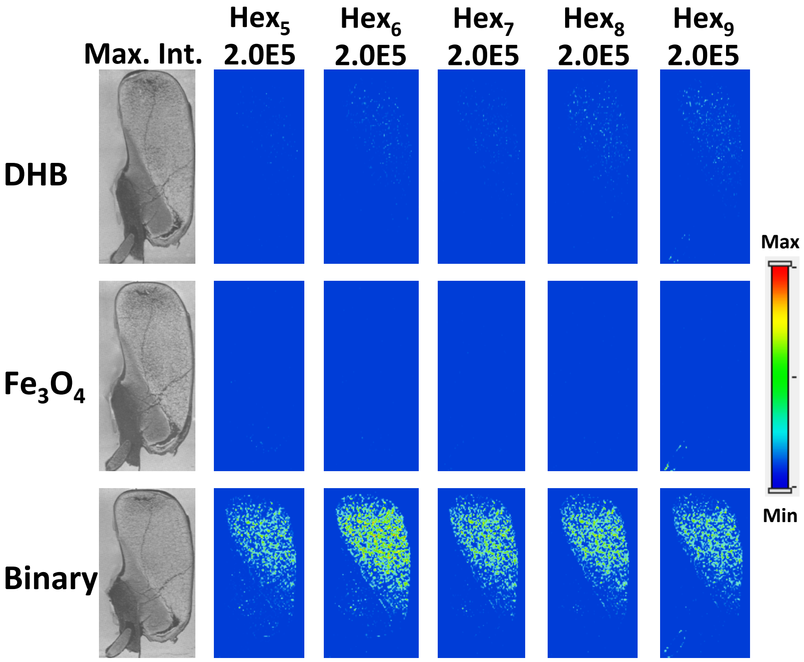

Figure 5. MS images of maize seed sections for hexose polysaccharides, Hex$_x$ (x=5-9), with DHB, Fe_3O_4 NPs, and the binary matrix. All species are detected and shown as a potassium ion adduct with a water loss, $[M-H_2O+K]^+$. Images are generated using absolute ion intensity with no normalization. Laser energies are the same as those referenced in Figure 2. Detailed parameters for image generation can be found in Table S2.

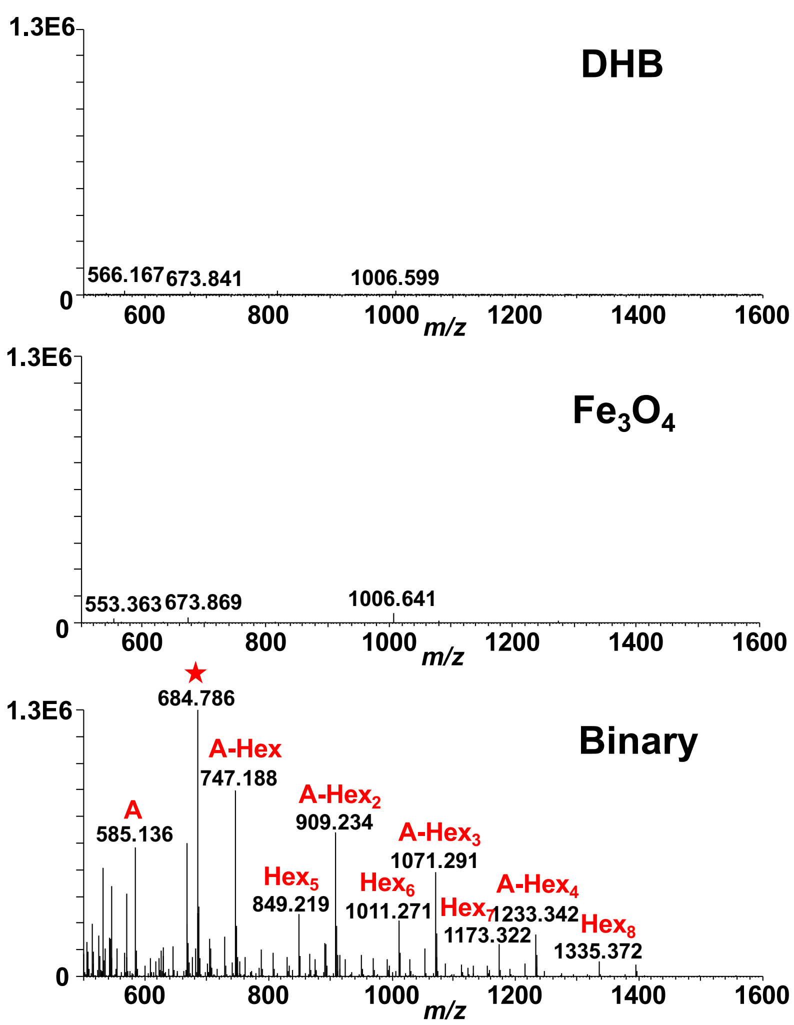

Figure 6. MS spectra for a maltodextrin mixture using each matrix. All compounds labeled are detected as $[M+K-H_2O]^+$. A is an unidentified compound present in this crude mixture also detected as conjugated with a series of hexose units. The red star denotes a background peak. All spectra shown are averages of ~66 spectra using a laser power of 89% (1.7 μJ).

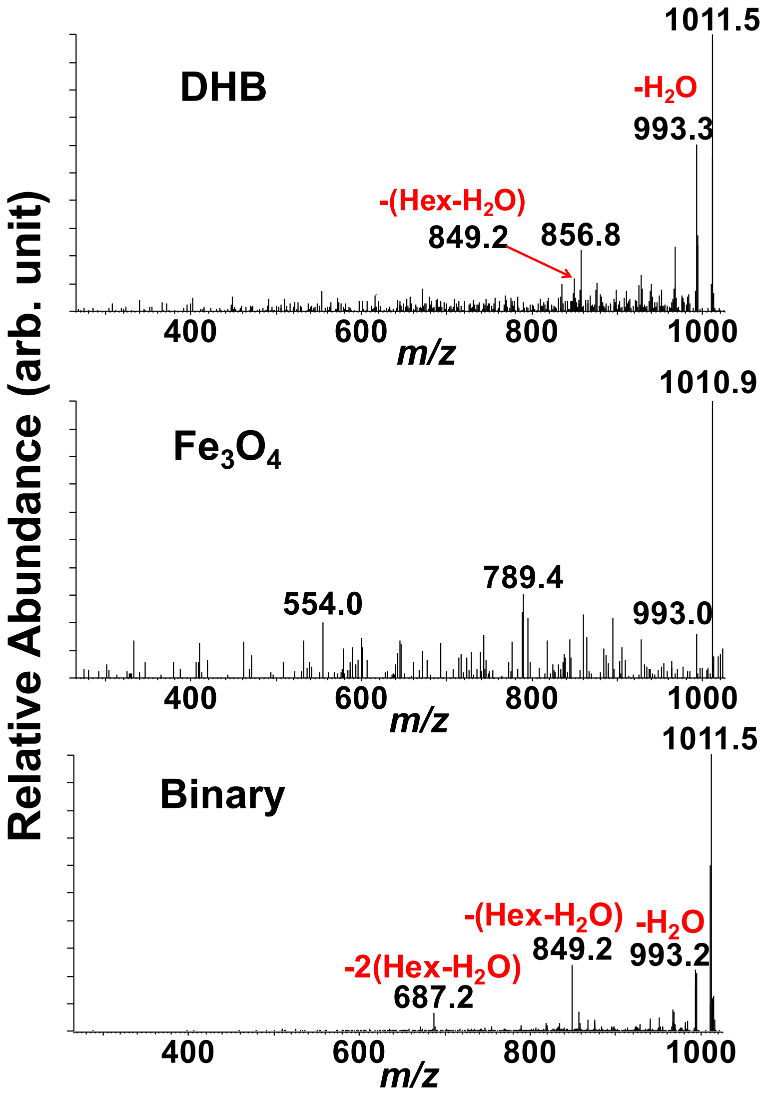

Figure 7. The MS/MS spectra of *m/z* 1011.3, corresponding to $[Hex_6+K-H_2O]^+$, from the multiplex MS imaging data set of all three matrices.

Supplemental Figures and Tables

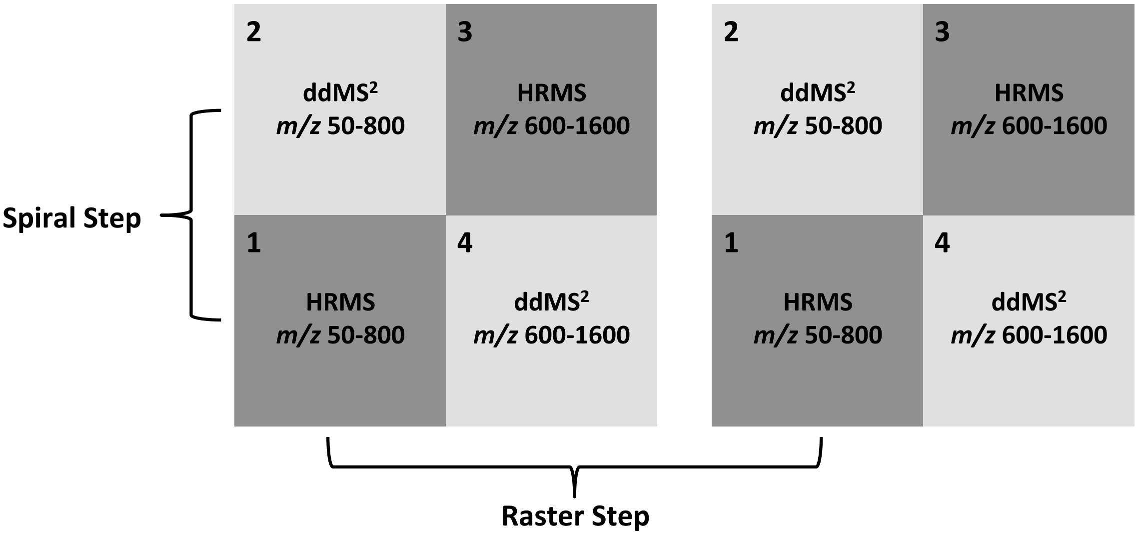

Figure S1. A schematic diagram of the multiplex MS imaging strategy used in this work. In a multiplex data acquisition, each imaging raster step is broken up into multiple spiral steps that can be defined by different MS parameters. In this work, the first and third spiral steps were high resolution Orbitrap scans (HRMS) in the low and high mass range, respectively. The second and fourth steps were data dependent MS/MS scans (ddMS^2) from the preceding HRMS scan.

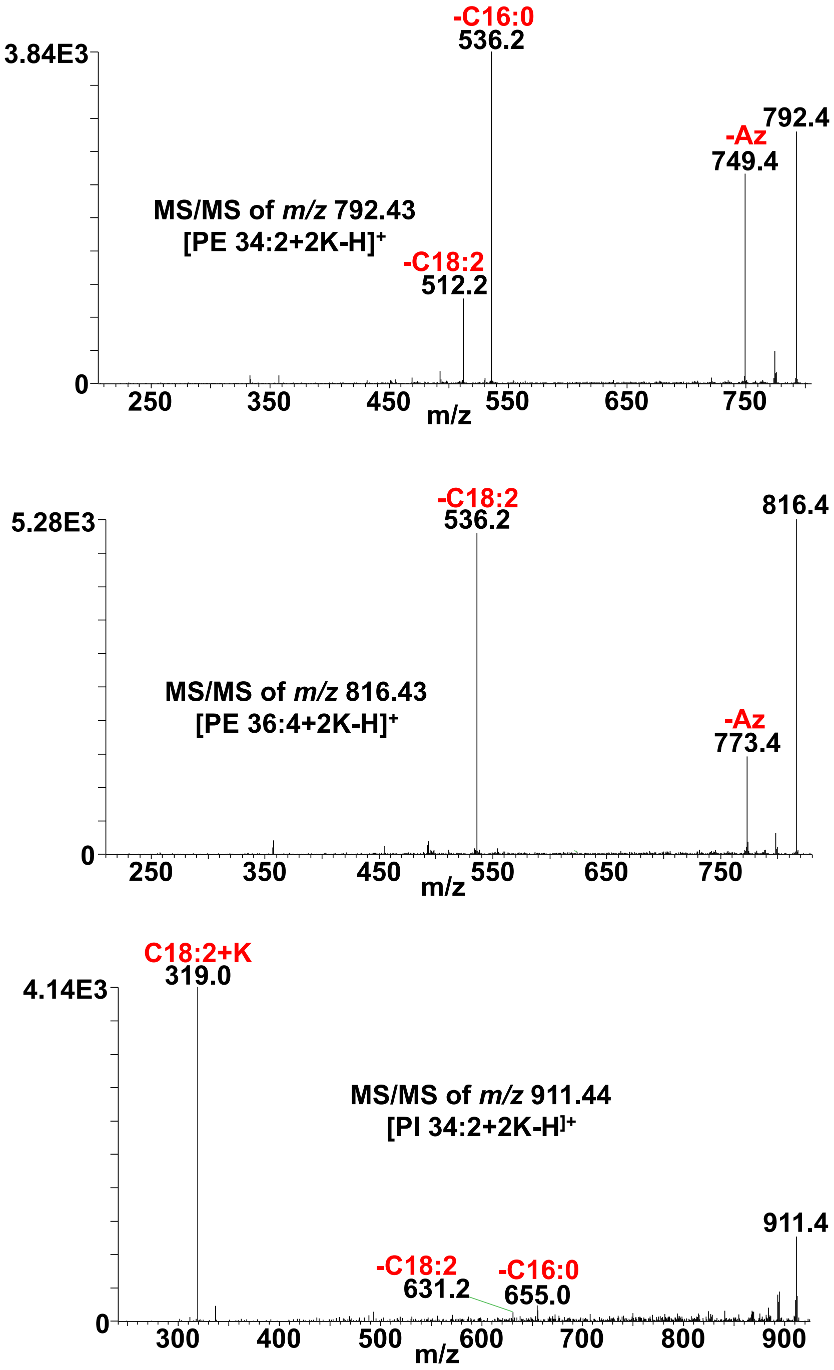

Figure S2. MS/MS spectra for [PE 34:2+2K-H]$^+$ (Top), [PE 36:4+2K-H]$^+$ (Middle), and [PI 34:2+2K-H]$^+$ (Bottom). MS/MS spectra of PEs contain a loss of 43 Da, corresponding to the azidine (Az) fragment previously described by Hsu and Turk (2000, *J Mass Spectrom,* **35**, 596-606). All spectra are from the Fe_3O_4 NP only data set.

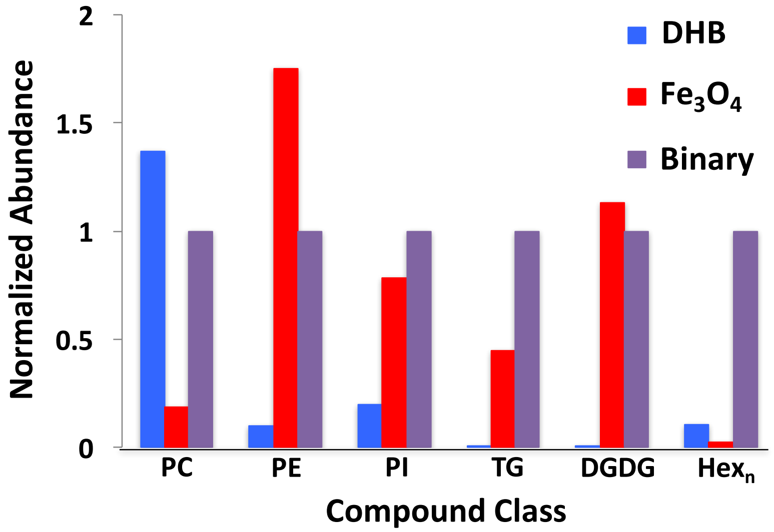

Figure S3. Similar data with Figure 3, but from a separate replicate experiment. Some differences from Figure 3 originate from biological and/or analytical variations.

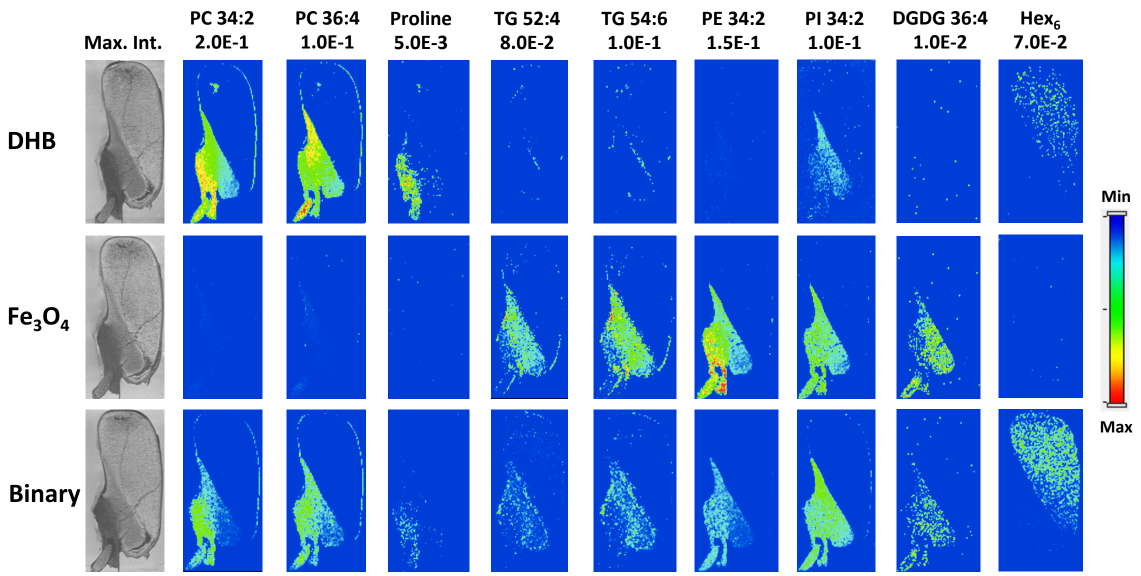

Figure S4. The same MS images as in Figure 4B but generated with normalization to the total ion count. The images demonstrate little to no difference with those generated from absolute ion intensity. Detailed parameters for image generation can be found in Table S2.

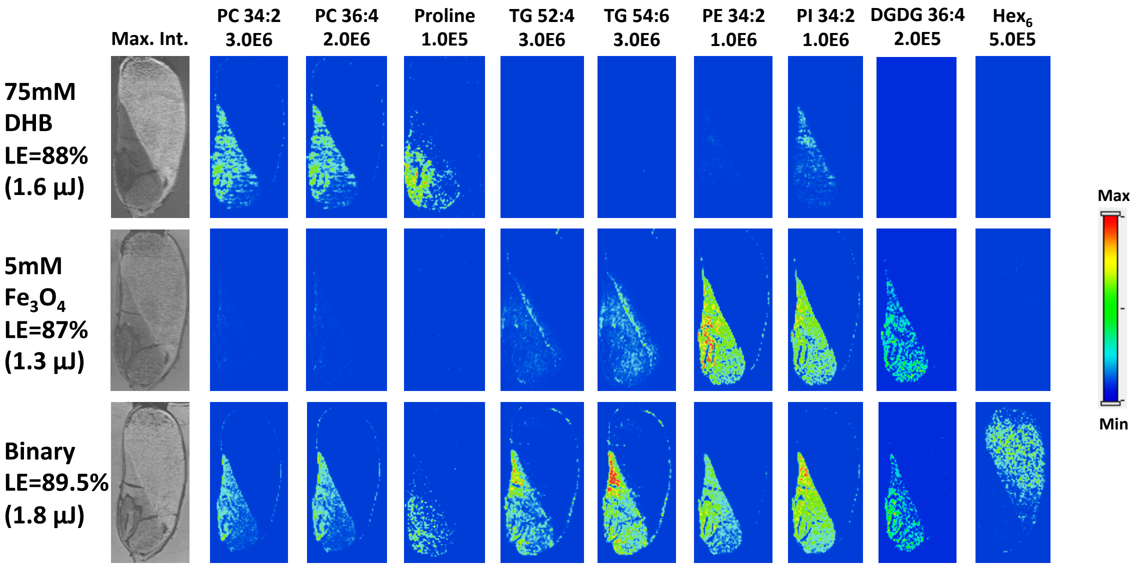

Figure S5. Similar MS images as in Figure 4B but from a separate replicate experiment. Detailed parameters for image generation can be found in Table S2.

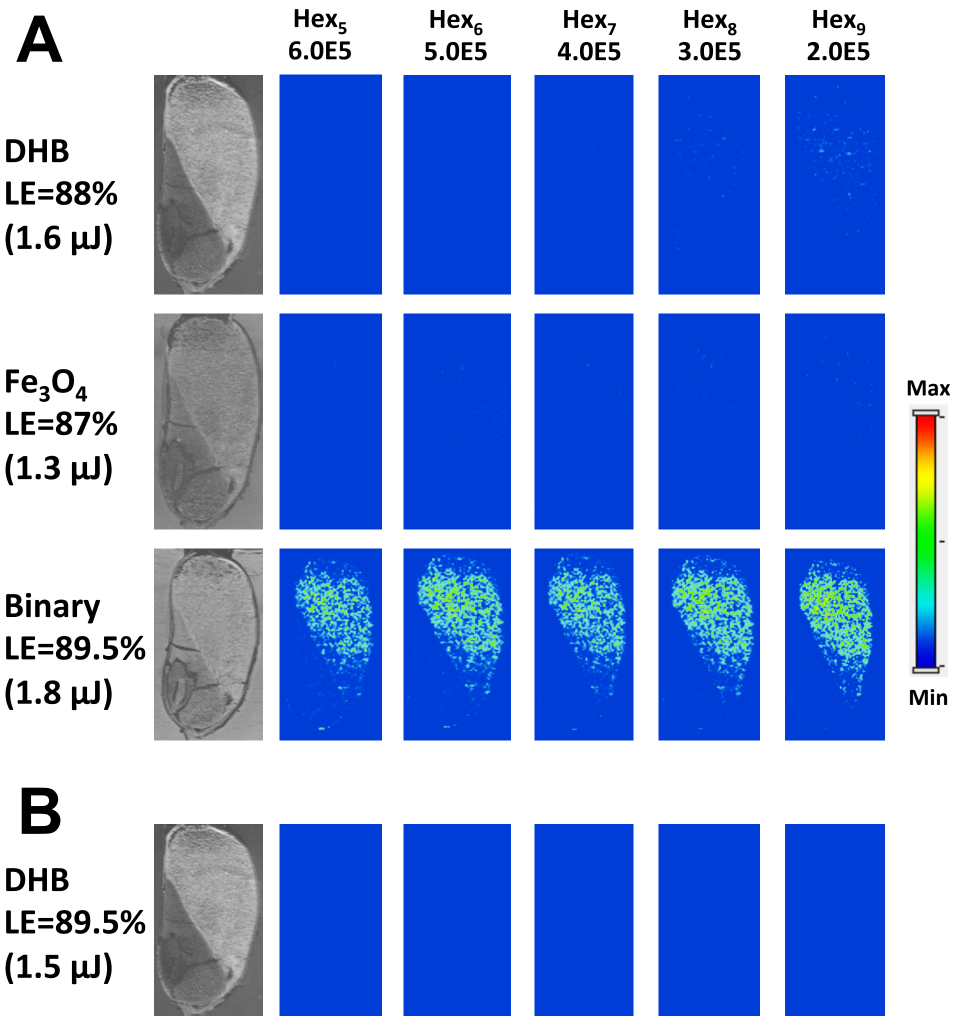

Figure S6. A) Similar MS images as in Figure 5, but from a separate replicate experiment. All species are detected as $[M+K-H_2O]^+$. B) MS images of various polysaccharides with DHB only matrix at the same laser energy as the binary matrix, demonstrating that the high ion signals of large oligosaccharides in the binary matrix is not due to the high laser energy. Detailed parameters for image generation can be found in Table S2.

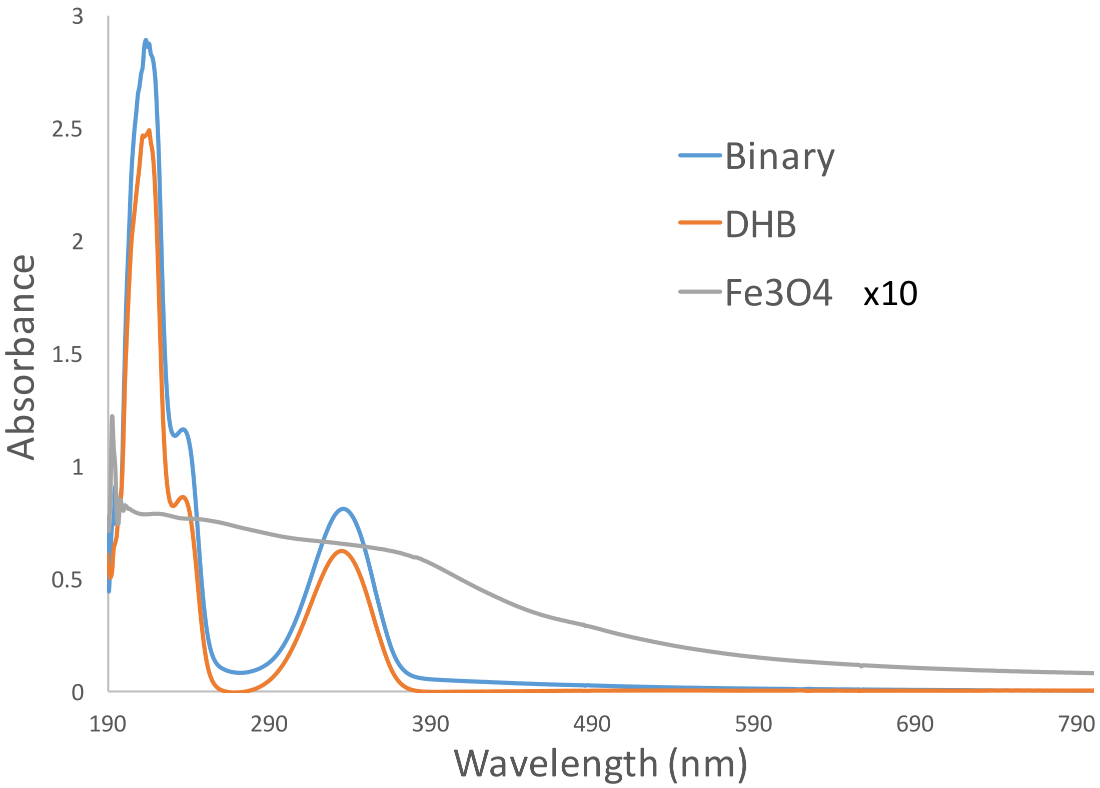

Figure S7. UV-Visible Absorption spectra of DHB, Fe_3O_4 NPs and the binary matrix. DHB and Fe_3O_4 NPs are at the concentration of 0.175 and 0.125 mM, respectively, and the binary matrix contains 0.175 mM DHB and 0.0125 mM Fe_3O_4. This is 400 times dilute concentration than we used in the application to maize seed sections, except the Fe_3O_4 NPs which is 40 times dilute or 10 times more concentrate than used in the UV-Vis of the binary matrix.

Table S1. Assignment of lipid compounds shown in Figure 2.

Accurate mass *m/z*	Identification	Formula	Mass Error (ppm)
737.45024	PC 34:2+K-$N(CH_3)_3$	$C_{39}H_{71}O_8PK$	-2.1
749.39153	PE 34:2+2K-NC_2H_5	$C_{37}H_{68}O_8PK_2$	-0.7
761.45033	PC 36:4+K-$N(CH_3)_3$	$C_{41}H_{71}O_8PK$	-1.9
763.46628	PC 36:3+K-$N(CH_3)_3$	$C_{41}H_{73}O_8PK$	-1.6
775.40824	PC 34:2+2K-N(CH3)$_3$-H	$C_{39}H_{70}O_8PK_2$	0.7
782.56776	PC 36:4+H	$C_{44}H_{81}NO_8P$	-2.1
792.43367	PE 34:2+2K-H	$C_{39}H_{73}O_8NPK_2$	-0.7
796.52383	PC 34:2+K	$C_{42}H_{80}NO_8PK$	-1.9
798.54036	PC 34:1+K	$C_{42}H_{82}NO_8PK$	-0.8
816.43377	PE 36:4+2K-H	$C_{41}H_{73}O_8NPK_2$	-0.6
818.45095	PE 36:3+2K-H	$C_{41}H_{75}O_8NPK_2$	1.3
820.52362	PC 36:4+K	$C_{44}H_{80}NO_8PK$	-2.1
822.54004	PC 36:3+K	$C_{44}H_{82}NO_8PK$	-1.1
824.55610	PC 36:2+K	$C_{44}H_{84}NO_8PK$	-0.6
873.48869	PI 34:2+K	$C_{43}H_{79}O_{13}PK$	-0.3
893.69903	TG 52:4+K	$C_{55}H_{98}O_6K$	-0.5
895.71470	TG 52:3+K	$C_{55}H_{100}O_6K$	-0.5
911.44480	PI 34:2+2K-H	$C_{43}H_{78}O_{13}PK_2$	-0.1
917.69916	TG 54:6+K	$C_{57}H_{98}O_6K$	-0.4
919.71467	TG 54:5+K	$C_{57}H_{100}O_6K$	-0.5
921.72997	TG 54:4+K	$C_{57}H_{102}O_6K$	-0.9
953.55981	DGDG (34:3)+K	$C_{49}H_{86}O_{15}K$	-0.0
955.57515	DGDG (34:2)+K	$C_{49}H_{88}O_{15}K$	-0.3
957.59055	DGDG (34:1)+K	$C_{49}H_{90}O_{15}K$	-0.6
975.54417	DGDG (36:6)+K	$C_{51}H_{84}O_{15}K$	-0.0
977.55957	DGDG (36:5)+K	$C_{51}H_{86}O_{15}K$	-0.3
979.57579	DGDG (36:4)+K	$C_{51}H_{88}O_{15}K$	0.3
981.59073	DGDG (36:3)+K	$C_{51}H_{90}O_{15}K$	-0.4

Table S2. Parameters used in the generation of MS images.

Compound	*m/z*	Tolerance	Min Intensity	Max Intensity
Figure 4B				
PC 34:2+K	796.525	.035	1.00	8.0E5
PC 36:4+K	820.525	.036	1.00	4.0E5
Proline+H	116.071	.002	1.00	8.0E4
TG 52:4+K	893.700	.041	1.00	4.0E5
TG 54:6+K	917.700	.042	1.00	7.5E5
PE 34:2+2K-H	792.435	.034	1.00	8.0E5
PI 34:2+2K-H	911.445	.041	1.00	6.0E5
DGDG 36:4+K	979.576	.046	1.00	2.0E5
Hex_6+K-H_2O	1011.280	.048	1.00	3.0E5
Figure 5				
Hex_5+K-H_2O	849.227	.037	1.00	2.0E5
Hex_6+K-H_2O	1011.280	.048	1.00	2.0E5
Hex_7+K-H_2O	1173.333	.062	1.00	2.0E5
Hex_8+K-H_2O	1335.386	.079	1.00	2.0E5
Hex_9+K-H_2O	1497.439	.088	1.00	2.0E5
Figure S4				
PC 34:2+K	796.525	.035	0.00	2.0E-1
PC 36:4+K	820.525	.036	0.00	1.0E-1
Proline+H	116.071	.002	0.00	5.0E-3
TG 52:4+K	893.700	.041	0.00	8.0E-2
TG 54:6+K	917.700	.042	0.00	1.0E-1
PE 34:2+2K-H	792.435	.034	0.00	1.5E-1
PI 34:2+2K-H	911.445	.041	0.00	1.0E-1
DGDG 36:4+K	979.576	.046	0.00	1.0E-2
Hex_6+K-H_2O	1011.280	.048	0.00	7.0E-2
Figure S5				
PC 34:2+K	796.525	.035	1.00	3.0E6
PC 36:4+K	820.525	.036	1.00	2.0E6
Proline+H	116.071	.002	1.00	1.0E5
TG 52:4+K	893.700	.041	1.00	3.0E6

Table S2 (cont'd)

TG 54:6+K	917.700	.042	1.00	3.0E6
PE 34:2+2K-H	792.435	.034	1.00	1.0E6
PI 34:2+2K-H	911.445	.041	1.00	1.0E6
DGDG 36:4+K	979.576	.046	1.00	2.0E5
Hex$_6$+K-H$_2$O	1011.280	.048	1.00	5.0E5
Figure S6				
Hex$_5$+K-H$_2$O	849.227	.037	1.00	6.0E5
Hex$_6$+K-H$_2$O	1011.280	.048	1.00	5.0E5
Hex$_7$+K-H$_2$O	1173.333	.062	1.00	4.0E5
Hex$_8$+K-H$_2$O	1335.386	.079	1.00	3.0E5
Hex$_9$+K-H$_2$O	1497.439	.010*	1.00	2.0E5

* Tolerance refers to mass windows used in the generation of MS images. Sufficiently large tolerance is used as to be appropriate for corresponding mass resolution at the given mass. In case of [Hex$_9$+K-H$_2$O]$^+$, a narrow tolerance is used to avoid the contribution from a near-by contamination peak.

CHAPTER 5

FIVE MICRON HIGH RESOLUTION MALDI MASS SPECTROMETRY IMAGING WITH SIMPLE, INTERCHANGEABLE, MULTI-RESOLUTION OPTICAL SYSTEM

A paper submitted to the *Journal of American Society of Mass Spectrometry*

Adam D. Feenstra, Maria E. Dueñas, and Young Jin Lee

Abstract

High spatial resolution mass spectrometry imaging (MSI) is crucial for the mapping of chemical distributions at the cellular and subcellular level. In this work, we improved our previous laser optical system for matrix-assisted laser desorption ionization (MALDI)-MSI, from ~9 μm practical laser spot size to a practical laser spot size of ~4 μm, thereby allowing for 5 μm resolution imaging without oversampling. This is accomplished through a combination of spatial filtering, beam expansion, and reduction of the final focal length. Most importantly, the new laser optics system allows for simple modification of the spot size solely through the interchanging of the beam expander component. Using 10x, 5x, and no beam expander, we could routinely change between ~4, ~7 and ~45 μm laser spot size, in less than five minutes. We applied this multi-resolution MALDI-MSI system to a single maize root tissue section with three different spatial resolutions of 5, 10, and 50 μm and compared the differences in imaging quality and signal sensitivity. We also demonstrated the difference in depth of focus between the optical systems with 10x and 5x beam expanders.

Introduction

Mass spectrometry imaging (MSI) has seen a surge in popularity as a biological imaging technique in the last decade due to its versatility, sensitivity, and label-free approach. These characteristics allow MSI to be applied to study a broad range of chemical compounds across a wide range of systems. This technique has been expanded to visualize compound classes such as lipids, proteins, and small molecules directly in plant and animal tissues [1-5]. General overviews of mass spectrometry imaging techniques can be found in various reviews [6-8].

Recently, high-resolution MSI has drawn enormous attention to visualize metabolites at a fine spatial resolution [9, 10]. The inherent characteristics of MS analysis combined with high-spatial resolution allow for detailed metabolite information to be visualized in cellular and subcellular localization, offering unprecedented detail in terms of localization and metabolite composition of various tissue types. This type of information can be incredibly useful for complex tissue types such as plant tissue, where various metabolic processes utilizing hundreds of thousands of metabolites are highly sequestered among various cell types [11, 12].

In matrix-assisted laser desorption/ionization (MALDI)-MSI experiments, the achievable spatial resolution for a given analysis is largely determined by the spot size of the laser beam at the sample surface. As such, significant work has been focused on methods to reduce the laser spot size in order to increase the achievable spatial resolution. Early efforts have been made using co-axial laser optics within the time of flight mass spectrometer, which achieved down to ~1 μm laser spot size for small molecules [13] or ~7 μm size for proteins [14]. These approaches, however, could not maintain high sensitivity in limited sampling size, restricting their biological applications; hence, later works have been mostly focused on laser optics, without modifying mass analyzer. Spengler's group combined the co-axial laser optics with atmospheric pressure MALDI [15], and successfully applied it for 3-10 μm high-spatial resolution imaging [9, 16]. Another approach that achieved extremely high-spatial resolution is to utilize transmission geometry [17, 18]. In this instrumental setup, the laser beam is focused onto a sample tissue through the backside of microscope slides. This transmission geometry setup has been shown to focus the laser beam to less than 1 μm and MSI data acquisition was made down to 2.5 μm resolution [19].

Caprioli [20] and our own group [21] have previously reported a simple approach by modifying the laser optics of commercially available instruments to use a larger beam diameter and a shorter laser focal length. Both approaches utilized a spatial filter setup, where the laser beam is focused through a small diameter pinhole, to filter out non-Gaussian components of the beam. Combined together, we were able to reduce the final laser spot size down to 5 μm, but the practical spot size was ~9 μm to obtain sufficient ion signals, and we used oversampling (use of a raster step smaller than the laser spot size with complete depletion of analytes or matrix in each step [22]) to achieve 5 μm resolution MS imaging of maize leaf cross-sections. For these works, the laser burn mark was used as a measure of spatial resolution; however, there are some ambiguities in this approach. The line scan across a sharp edge has been used to better define the spatial resolution in secondary ion mass spectrometry [23]. This effort has been recently extended to MALDI-MS imaging with a specially designed pattern [24], but it is not available to most scientists yet. Hence, here we use the laser burn mark as a simple measure of the spatial resolution, even though it might measure slightly smaller than the actual resolution.

In this work, we improved our previous high-resolution optical setup to achieve a practical laser spot size below 5 μm, so that 5 μm high-resolution MALDI-MSI can be achieved without oversampling. Furthermore, the new setup allows easy change of the final spot size, ~4 , ~7, and ~45 μm, through the simple interchange of the beam expander between 10x, 5x, and no beam expander, respectively. This multi-resolution setup is applied on maize root, and visualized various metabolites at spatial resolutions of 5, 10, and 50 μm, all on a single tissue section comparing analytical characteristics between the three resolution setups.

Experimental

Materials

2,5-dihydroxybenzoic acid (DHB, 98%) was purchased from Sigma-Aldrich (St. Louis, MO, USA). Gelatin from porcine skin (300 bloom) was purchased from Electron Microscopy Sciences (Hatfield, PA, USA). A 1 mm diamond aperture (HP-3/8-DISC-DIM-1000) was purchased from Lenox Laser, Inc. (Glen Arm, MD, USA). A 60 mm focal length near UV achromatic lens (#65-977) and a 25/25.4 mm diameter lens mount (#56-354) were purchased from Edmund Optics (Barrington, NJ, USA). A 10x and 5x beam expander were purchased from ThorLabs Inc. (BE10x and BE5x, Newton, NJ, USA). B73 inbred maize seeds were obtained courtesy of Dr. Marna Yandeau-Nelson at Iowa State University.

Maize Root Growth and Sectioning

For MALDI-MSI analysis of root sections, inbred B73 maize seeds were grown using a procedure slightly modified from previously described methods [25]. Briefly, a row of seeds (embryo facing down) was arranged along the top edge of a moist paper towel. The paper towel was then rolled up and the bottom of the roll was placed into a 1 L beaker half filled with water. The seeds were allowed to grow for 10 d while kept in the dark. The beaker was checked periodically to ensure enough water remained to submerge the lower portion of the paper towel roll. After 10 d, the roots were collected and flash-frozen for the area of interest in liquid nitrogen to quench the metabolism. The frozen roots were then embedded in a 10% w/v gelatin solution in a cryo-mold and held on liquid nitrogen until the gelatin was mostly frozen. The roots were then moved to a cryostat (CM1520; Leica Biosystems, Buffalo Grove, IL, USA) with the temperature set at -22 °C, thermally equilibrated for 30 min, and then cryo-sectioned at a thickness of 10 μm and collected on adhesive tape windows (Leica).

Mass spectrometry imaging analysis

A maize root section selected for MSI was initially placed onto a chilled aluminum block and lyophilized under moderate vacuum to prevent condensation as the section was brought to room temperature. A matrix layer of DHB was then deposited onto the gelatin sections by sublimation-vapor deposition, as has been previously described [26] at a temperature of 140 °C for 6 minutes.

The MALDI-MSI experiments were performed on a MALDI-linear ion trap (LIT)-Orbitrap mass spectrometer (MALDI-LTQ-Orbitrap Discovery; Thermo Finnigan, San Jose, CA, USA) modified to incorporate an external, 355 nm Nd:YAG laser (UVFQ, Elforlight, Daventry, UK). Three separate MS imaging runs were performed on the tissue section at different spatial resolutions of 5, 10, and 50 μm using a 10x, 5x, and no beam expander, respectively. The laser energy used was 84%, 87%, and 89%, respectively, optimized for each resolution setup with slightly higher laser energy required as the laser spot size is increasing. The same ten laser shots were used per raster step for all three resolutions. Mass spectra were acquired in positive ion mode using an Orbitrap for a scan range of *m/z* 50-1,000 at a mass resolution of 30,000 at *m/z* 400. After data acquisition, MS images were generated using ImageQuest software (Thermo Finnigan) and mass spectra were analyzed using Xcalibur (Thermo Finnigan). All images were generated using a mass tolerance of ±0.005 and no normalization was applied.

MS/MS analysis was performed on an adjacent tissue section prepared identically to the one used for MS imaging. A multiplex imaging run [27] was performed at 50 μm resolution using no beam expander to collect MS/MS for multiple ions in a single run. The three ions shown in this work were analyzed with a mass window of 1.0 Da. The collision energies were 125 for *m/z* 184.072, and 75 for *m/z* 365.102 and 426.077. All ions were activated for 30 ms.

Depth of Focus Experiment

A 10% w/v solution of gelatin was poured into a cryo-mold and frozen on liquid nitrogen. The gelatin was then cryo-sectioned at varying thicknesses and the sections were collected using adhesive tape windows. The sections were taped onto pre-chilled glass slides and stored at -80 °C. For spot size determination, the gelatin sections were prepared identically to those for imaging runs. Then, employing the various beam expander setups (10x, 5x, and no beam expander), laser spots at varying energies were laid and measured through optical microscopy.

Safety Warning

Replacement of the manufacturer's enclosed laser system with an external laser such as the one described here results in a class IIIB laser system. Appropriate precautions should be taken when utilizing this system, including the use of appropriate eyewear and safety controls.

Results and Discussion

Modifications to Laser Optical System

In this work, the optics of a commercial MALDI-LIT-Orbitrap instrument were modified to achieve 5 μm high-resolution imaging, while also allowing for multi-resolution imaging through the interchanging of beam expanders. This work represents a significant improvement from our group's previous work reducing the laser spot size for high-resolution MALDI-MSI applications. Descriptions of the original MALDI source [28] and our previous modification [21] can be found in earlier publications.

For a laser beam, the diffraction limited spot size is given by the following equation [20]:

$$D_s = M^2 \cdot \frac{4}{\pi} \cdot \lambda \cdot \frac{f}{D_b} \cdot \frac{1}{\cos\theta} \qquad (1)$$

where D_s represents the diffraction limited spot size, M represents the beam quality factor (M=1 for a perfect Gaussian beam), λ represents the laser wavelength, f represents the focal length of the focusing lens, D_b represents the input beam diameter to the final focusing lens, and cos θ represents the incident angle of the laser beam on the sample.

Based on this equation, there are three main ways to reduce the laser spot size for a given optical system: (1) improving the beam quality factor (M closer to 1), (2) reducing the focal length of the focusing lens, and (3) increasing the input beam diameter. For the adjusted optical system in this work, all three factors were taken into consideration and optimized to the best of our abilities without requiring extensive instrumental modifications. A schematic representation and photographs of the modified optical setup and source can be found in Figure 1a and 1b, respectively.

In our previous work [21], a home-built Keplerian configuration was employed as a beam expander. In this setup, the laser beam is focused down to a small spot, and then re-expanded to a bigger laser beam size. The laser beam in this home-built configuration was focused through a small diameter pinhole (25 µm) to remove significant non-Gaussian beam components. However, optical alignment to focus the laser beam through a 25 µm pinhole proved to be a very difficult and time consuming process, and turned out to be problematic to interconvert between different laser spot sizes when more moderate resolution imaging was desired. Additionally, focusing the laser beam down to a small enough spot size to fit through the pinhole increases the laser fluence and energy density, which we found can cause significant damage to a pinhole, even for those with a high-energy damage threshold.

In this work, to improve the beam quality factor (<1.2 initially, per manufacturer specifications), a one millimeter diameter pinhole (4) was placed into the beam path before the beam expander. While this setup may not be as effective at removing non-Gaussian components compared to focusing through a small pinhole, it does remove the majority of the non-Gaussian laser beam components while avoiding the issues of aligning with a small opening, as well as damage or destruction of the pinhole that arise from exposure to a highly focused laser beam.

The most important benefit of this setup is that we can adjust the laser spot size by simply changing the beam expander in a process that requires less than 5 min. For this work, we adopted commercially available Galilean configuration beam expanders with an encased, fixed geometry, which can be easily changed between different magnification beam expanders. To achieve the highest spatial resolution, a 10x beam expander was inserted into the laser beam path (5), resulting in an expanded beam diameter of 10 mm, which is almost the maximum size that can pass through instrumental openings and into final focus lens in the current geometry. The beam expander is positioned after the 1mm pinhole and is held in place by a simple locking screw. As such, the beam expander can easily be inserted or removed as desired, allowing for a fast and simple way to change between input beam diameters, and therefore, final laser spot size.

Lastly, we modified the lens holder to position the focus lens as close as possible to the MALDI plate. The original focal length of the final lens was 125 mm [28], which we previously modified to accommodate a 100 mm focal length lens [21]. In this work, we further reduced the focal length down to 60 mm by integrating a custom-built lens holder into the source of the instrument. As the photograph in Figure 1b shows, the position of lens and lens holder can be adjusted by threading the bronze intermediate component in or out on the male rod; the optimum focal position for the smallest laser spot size was found by manually adjusting the z-position of the bronze intermediate (C). At the optimum position, the focus lens is almost touching the outer case of the quadrupole ion lens.

Altogether, three optical modifications were made in this work, with the pinhole reducing the value of M close to 1, the beam expander increasing the value of D_b to 10 mm, and the final focus lens reducing the value of f to 60 mm. Assuming M= 1.0, equation 1 gives the minimum achievable spot size as 3.2 μm with f= 60 mm, D_b= 10 mm, λ= 0.355 μm, and θ= 32°, dramatically improved from the original ~50 μm, and our previous work of 4.9 μm. In our previous work, ~5 μm laser spot sizes were obtained but without any ion signals (laser energy of 79%), and the practical laser spot size was ~9 μm when the laser energy was increased to obtain sufficient ion signals for detection (laser energy of 80.5%). In the present work, a spot size as small as ~3.4 μm was obtained with sufficient ion signals (laser energy of 80%), while achieving the laser spot size close to the theoretical minimum (Figure 2). The laser spot size remained low, ~4 μm, even at the laser energy of 84% as shown later in the application to a maize root cross-section, suggesting we have an improvement of a factor of two in the laser spot size compared to our previous setup.

It needs to be mentioned that the MALDI sample plate is not completely level, and the position within the plate holder affects the laser spot size. Hence, we optimized laser focusing for the top portion of the left slide (our plate holder can load two microscope glass slides side by side) with an adhesive tape and a 10 μm thick tissue, and all the measurements were made at this position. The spot size is very reproducible at the same position even with multiple plate insertions and ejections. The laser spot size is significantly affected when another position is used for the 10x beam expander, but the spot size change is minimal with 5x beam expander with less than 10 μm spot sizes regardless of the position. The laser spot size is also greatly influenced by the tissue thickness for the 10x beam expander (Supplemental Figure S1), in much greater extent than we expected. This is partially attributed to the aberration halos, which are minimal when the laser is fully focused or a smaller beam size (e.g., 5x beam expander) is used.

As will be further discussed in the next section, when a resolution of 5 μm is not necessary, a slightly more moderate resolution imaging run with 10 μm resolution using a 5x beam expander will be more convenient for routine imaging experiments. When the same experiment varying gelatin thickness was performed with the 5x beam expander (Figure S1), the laser spot size was ~7 μm with 10 μm thick gelatin and still only ~8 μm with 5 or 15 μm thick gelatin. Even with the glass slide only without gelatin or adhesive tape, the laser spot size is increased only to ~9 μm. Compared to the experiments with the 10x beam expander, these spots laid on multiple sections were much more reproducible, confirming the larger depth of focus with a slightly lower resolution. These results indicate that, if necessary, we could vary the sample thickness on purpose to place the sample at the appropriate focal point when instrumental parameters are altered slightly, such as minute differences in mechanical z-position depending on the MALDI plate.

Multi-resolution MS imaging of a maize root cross-section

For the demonstration of high-resolution 5 μm MS imaging, the new laser optical system was applied to B73 maize roots grown for 10 d. Plant roots are composed of a variety of tissue types (xylem, phloem, cortex, pith) in a small scale [29], of which the visualization of the fine structural features is attractive to demonstrate the current technological development. We have previously applied MS imaging for various plant tissue types including flower [30], leaf [21, 31], seed [32], and root surface [30], but this is our first time analyzing root cross-sections.

Additionally, here we demonstrate an easy interchange between three different resolution setups and compare the differences in their analytical characteristics: 5 μm resolution using a 10x beam expander and ~4 μm spot size, 10 μm resolution using a 5x beam expander and ~7 μm spot size, and 50 μm resolution using no beam expander and ~45 μm spot size. High-resolution imaging can provide detailed cellular and subcellular features of chemical distributions, but requires much longer data acquisition time and is expected to have limited sensitivity. In contrast, low resolution MS imaging can be done on a short time scale and with high sensitivity, but does not provide fine localization information. For this optical setup, the desired beam expander can be easily interchanged as the 10x beam expander is held in place by a single locking screw, while the 5x beam expander threads into a holder already incorporated into the optical system. As such, switching between the three setups (10x, 5x, and no beam expander) was done in about 2-3 min in this experiment.

A single maize root cross-section was sublimated with DHB and analyzed in positive ion mode using 3 different resolution setups solely through the interchanging of the beam expander component of the optical system described in Figure 1. Using the 10x beam expander, a spot size of ~4 μm was achieved and an imaging run was performed with a raster step of 5 μm to ensure no oversampling occurred. Replacing the 10x beam expander with the 5x beam expander or using no beam expander generated laser spots on the order of ~7 or ~45 μm, respectively, and imaging runs were performed at raster step sizes of 10 and 50 μm. MS imaging took 4 h to image 1/4 of the root section in 5 μm resolution, 1.2 h to image another 1/4 of the root section in 10 μm resolution, and 0.2 h to image the remaining half of the root section in 50 μm resolution. Optical images of a maize root cross-section, ablation craters for imaging runs performed in this work, and an optical image of the root cross-section after the 3 imaging runs are shown in Figure 3.

MS images for three ions with distinct localization patterns from each of the imaging runs are presented together in Figure 4, with 50 μm images shown in the right half, 10 μm images in the top left quadrant, and the 5 μm images in the bottom left quadrant. The ions at *m/z* 184.072 and 365.102 are confidently identified as protonated phosphocholine and a sodiated disaccharide, respectively, through accurate mass and MS/MS shown in Supplemental Figure S2. The identification of *m/z* 426.077 is tentatively assigned as potassiated 2-hydroxy-4,7-dimethoxy-1,4-benzoxazin-3-one-glucoside (HDMBOA-Glc) based on accurate mass and MS/MS (Supplementary Figure S2), along with the presence of the corresponding deprotonated ion in negative mode with similar localization (not shown). This compound is known to present in maize [33] and previously seen in our MSI of maize leaf in negative mode [21].

In the 50 μm images of Figure 4 (the right half of root section), phosphocholine (*m/z* 184.072) appears to be localized throughout the entire root, while the disaccharide (*m/z* 365.102) appears to be evenly spread within the stele of the root. As the resolution is increased to the 10 and 5 μm images (the left half of root section), we are able to observe fine localization information that the disaccharide is localized mostly to the stele but also partially extended to the cortex, while the phosphocholine is localized throughout the root, but not homogeneously as it appears in 50 μm images. Meanwhile, the HDMBOA-Glc (*m/z* 426.077) appears to be distributed around the outer edges and epidermal cell layer of the root in the 10 and 50 μm images, but is barely seen in the 10x image as will be further discussed later.

A combination image is generated for these ions to further elucidate the fine spatial localization of the three metabolites. Looking at the 50 μm resolution combination image, the disaccharide (green) and phosphocholine (blue) appear to be distributed between the inner stele and cortex of the root with some overlap (cyan color), while phosphocholine and HDMBOA-Glc (red) appear to be overlapping in the outer layers of the root (purple). In the 10 μm resolution image (top-left quadrant of the whole root section), we are able to determine that the disaccharide is localized within the xylem of the root in the inner stele and large porous region in the cortex, whereas phosphocholine is occupying the rest of the space in cortex and stele. Additionally, the image allows us to observe that phosphocholine and HDMBOA-Glc are co-localized in some part of the cortex layers (purple).

Lastly, in the 5 μm resolution image zoomed in and enlarged for better visualization, we can confirm the disaccharide is localized within the xylem tissues and surrounded by phosphocholine, but also find that neither the phosphocholine nor the disaccharide is localized within the small phloem tissues. This was not discernable at 10 μm resolution, and demonstrates the necessity of high-resolution capabilities for the elucidation of fine localization information. Individual cell walls can also be clearly observed within the stele and cortex layers using 5 μm resolution, as they are outlined by phosphocholine. In the case of HDMBOA-Glc, however, both the 50 and 10 μm resolution images show sufficient ion signal to provide localization for this metabolite, while the 5 μm image shows little to no signal and is unable to provide clear localization.

For a better comparison of the spectral quality among the three different datasets, average mass spectra from each 1/4 of the root section were compared as shown in Figure 5a (for the no beam expander run, only half of the imaged root section was averaged to compare almost identical tissue areas). Foremost, it is apparent that the 50 μm resolution spectrum has significantly higher ion signals than either the 5 or 10 μm resolution spectra (8.7 or 4.8 times in total ion count, respectively), with the 10 μm resolution spectrum having higher ion signals than the 5 μm (~1.8 times in total ion count). This observation is not surprising considering a larger spot size results in a larger sampling area and, consequently, more ions shuttled into the mass spectrometer for analysis. It should be noted that the ion signals in the averaged spectra are not summed ion intensities but scaled by the number of spectra.

More precisely, the relation between sampling size and ion signal is more complicated than the simple description above, as it is also affected by laser fluence [34, 35]. As the laser spot size is reduced, higher laser fluence is needed to obtain sufficient ion signals, and ion signal increases as a power function of laser fluence for the same laser spot size [34]. When compared at the optimum laser fluence, the ion yield per unit area is inversely proportional to the laser spot size, increasing with smaller laser spot size [36]. This agrees with our result in that the signal increase at a lower resolution is linearly proportional to the laser spot size, not the area. The optimum laser fluences used in this study are higher than typically reported, ~1,300 J/m^2 for 50 μm MS image and ~18,000 and ~27,000 J/m^2 for 10 and 5 μm MS images, respectively. However, such high laser fluences are often reported when a Gaussian shape laser beam is used [35].

More significant differences are found for low abundance ions such as those in the inset spectra of Figure 5. In this high mass range (>600 Da), six real ion peaks are clearly observed in 50 μm resolution spectrum at *m/z* 629, 737, 758, 780, 796, and 820 (all phosphatidylcholines or their fragments, except *m/z* 629 which is unidentified) with S/N above 2. It should be noted that the noise count displayed in the Qualbrowser software is over-represented. Therefore, the S/N reported here is expected to be about five times higher than the typical definition of S/N. At a higher resolution, the number of real ion peaks above S/N of 2 is decreased to 3 and 0 for 10 and 5 μm resolution setup, respectively, clearly demonstrating the decrease of sensitivity at higher resolution. The images for the six ions display results consistent with this observation (Figure 5b). All ions show clear images in the 50 μm resolution, but the image quality is dramatically deteriorated at higher resolution, with only three ions show reasonable images in 10 μm resolution and none of them showing clear images in 5 μm resolution. These results are in line with recently published work demonstrating the effect of beam size related to total ion count [37].

These results demonstrate the tradeoff that comes with utilizing a small laser spot size for high-resolution mass spectrometry imaging. While the spatial details that are gleaned are significantly increased for the high-resolution imaging, as shown in Figure 4, the ability to detect low abundance ions is reduced as seen in Figure 5. Depending on the analytes of interest, time constraints, and the required spatial resolution, low to moderate resolution imaging runs may be better suited in many cases. High-resolution analysis then can be used for those analytes that are highly abundant to further explore their fine spatial visualization.

Conclusions

This work represents a substantial advancement from our previous effort to reduce the laser spot size, and thus, achieve high-spatial resolution for MALDI-MSI. We have achieved a minimum laser spot size of ~3.4 μm, which is almost the ultimate limit possible in the current instrument without modifying the mass spectrometry ion optics. We have found that this setup has a serious limitation coming from the shallow depth of focus; yet, we could still routinely obtain ~4 μm laser spot size. The biggest advantage of this system from a practical viewpoint is the simplicity with which the spatial resolution can be modified. A simple interconversion between different resolution setups is possible within a few minutes using 10x beam expander for the high-resolution 5 μm imaging, 5x beam expander for the medium-resolution 10 μm imaging, and no beam expander for low-resolution 50 μm imaging. The combination of the three-resolution setup is successfully demonstrated on a single root section, comparing analytical characteristics in terms of image quality and sensitivity.

With this improvement, now we can routinely perform ultra-high resolution MALDI-MSI as well as high-throughput, high-sensitivity, low-resolution MSI and medium-throughput, moderate-resolution MSI experiments. While previously demonstrated instrumental setups have shown smaller ultimately achievable spot sizes on the order of 1 μm [13, 19], actual applications have been mostly performed with 5 or 10 μm spatial resolution due to the limited amounts of analytes available in a small sampling size. Plant samples are particularly challenging to obtain sufficient ion signals at high-resolution, and most applications are made at 5 μm or larger spatial resolution [16]. Considering this limitation, we believe our system is comparable to other top notch systems in most high-resolution imaging applications. Furthermore, the ease of changing the spatial resolution is a strength of our system which most other optics systems do not offer. We expect we should be able to perform various interesting applications in the future with this tunable capability of MALDI-MSI.

Acknowledgments

This work was supported by the US Department of Energy (DOE), Office of Basic Energy Sciences, Division of Chemical Sciences, Geosciences, and Biosciences. A special thanks to Terry Herrman and Alon Klekner of the Ames Laboratory for their assistance in designing and engineering the lens holder optical components. The Ames Laboratory is operated by Iowa State University under DOE contract DE-AC02-07CH11358.

References

1. Murphy, R.C., Hankin, J.A., Barkley, R.M.: Imaging of lipid species by MALDI mass spectrometry. J. Lipid Res. **50**, S317-S322 (2009)
2. Stoeckli, M., Chaurand, P., Hallahan, D.E., Caprioli, R.M.: Imaging mass spectrometry: A new technology for the analysis of protein expression in mammalian tissues. Nat. Med. **7**, 493-496 (2001)
3. Cha, S., Zhang, H., Ilarslan, H.I., Wurtele, E.S., Brachova, L., Nikolau, B.J., et al.: Direct profiling and imaging of plant metabolites in intact tissues by using colloidal graphite ‐ assisted laser desorption ionization mass spectrometry. The Plant Journal. **55**, 348-360 (2008)
4. Li, Y., Shrestha, B., Vertes, A.: Atmospheric pressure infrared MALDI imaging mass spectrometry for plant metabolomics. Anal. Chem. **80**, 407-420 (2008)
5. Sturtevant, D., Lee, Y.-J., Chapman, K.D.: Matrix assisted laser desorption/ionization-mass spectrometry imaging (MALDI-MSI) for direct visualization of plant metabolites in situ. Curr. Opin. Biotechnol. **37**, 53-60 (2016)
6. van Hove, E.R.A., Smith, D.F., Heeren, R.M.: A concise review of mass spectrometry imaging. J. Chromatogr. **1217**, 3946-3954 (2010)
7. Lee, Y.J., Perdian, D.C., Song, Z., Yeung, E.S., Nikolau, B.J.: Use of mass spectrometry for imaging metabolites in plants. Plant J. **70**, 81-95 (2012)
8. Weaver, E.M., Hummon, A.B.: Imaging mass spectrometry: From tissue sections to cell cultures. Adv. Drug Del. Rev. **65**, 1039-1055 (2013)
9. Römpp, A., Spengler, B.: Mass spectrometry imaging with high resolution in mass and space. Histochem. Cell Biol. **139**, 759-783 (2013)
10. Römpp, A., Guenther, S., Schober, Y., Schulz, O., Takats, Z., Kummer, W., et al.: Histology by Mass Spectrometry: Label ‐ Free Tissue Characterization Obtained from High ‐ Accuracy Bioanalytical Imaging. Angew. Chem. Int. Ed. **49**, 3834-3838 (2010)
11. Sumner, L.W., Mendes, P., Dixon, R.A.: Plant metabolomics: large-scale phytochemistry in the functional genomics era. Phytochemistry. **62**, 817-836 (2003)
12. Goodacre, R., Vaidyanathan, S., Dunn, W.B., Harrigan, G.G., Kell, D.B.: Metabolomics by numbers: acquiring and understanding global metabolite data. Trends Biotechnol. **22**, 245-252 (2004)
13. Spengler, B., Hubert, M.: Scanning microprobe matrix-assisted laser desorption ionization (SMALDI) mass spectrometry: Instrumentation for sub-micrometer resolved LDI and MALDI surface analysis. J. Am. Soc. Mass Spectrom. **13**, 735-748 (2002)
14. Chaurand, P., Schriver, K.E., Caprioli, R.M.: Instrument design and characterization for high resolution MALDI-MS imaging of tissue sections. J. Mass Spectrom. **42**, 476-489 (2007)
15. Koestler, M., Kirsch, D., Hester, A., Leisner, A., Guenther, S., Spengler, B.: A high ‐ resolution scanning microprobe matrix ‐ assisted laser desorption/ionization ion source for imaging analysis on an ion trap/Fourier transform ion cyclotron resonance mass spectrometer. Rapid Commun. Mass Spectrom. **22**, 3275-3285 (2008)

16. Bhandari, D.R., Wang, Q., Friedt, W., Spengler, B., Gottwald, S., Rompp, A.: High resolution mass spectrometry imaging of plant tissues: towards a plant metabolite atlas. Analyst. **140**, 7696-7709 (2015)
17. Zavalin, A., Todd, E.M., Rawhouser, P.D., Yang, J., Norris, J.L., Caprioli, R.M.: Direct imaging of single cells and tissue at sub‐cellular spatial resolution using transmission geometry MALDI MS. J. Mass Spectrom. **47**, 1473-1481 (2012)
18. Thiery-Lavenant, G., Zavalin, A.I., Caprioli, R.M.: Targeted Multiplex Imaging Mass Spectrometry in Transmission Geometry for Subcellular Spatial Resolution. J. Am. Soc. Mass Spectrom. **24**, 609-614 (2013)
19. Zavalin, A., Yang, J., Hayden, K., Vestal, M., Caprioli, R.M.: Tissue protein imaging at 1 μm laser spot diameter for high spatial resolution and high imaging speed using transmission geometry MALDI TOF MS. Anal. Bioanal. Chem. **407**, 2337-2342 (2015)
20. Zavalin, A., Yang, J.H., Caprioli, R.: Laser Beam Filtration for High Spatial Resolution MALDI Imaging Mass Spectrometry. J. Am. Soc. Mass Spectrom. **24**, 1153-1156 (2013)
21. Korte, A.R., Yandeau-Nelson, M.D., Nikolau, B.J., Lee, Y.J.: Subcellular-level resolution MALDI-MS imaging of maize leaf metabolites by MALDI-linear ion trap-Orbitrap mass spectrometer. Anal. Bioanal. Chem. **407**, 2301-2309 (2015)
22. Jurchen, J.C., Rubakhin, S.S., Sweedler, J.V.: MALDI-MS imaging of features smaller than the size of the laser beam. J. Am. Soc. Mass Spectrom. **16**, 1654-1659 (2005)
23. Senoner, M., Wirth, T., Unger, W., Osterle, W., Kaiander, I., Sellin, R.L., et al.: BAM-L002 - a new type of certified reference material for length calibration and testing of lateral resolution in the nanometre range. Surf. Interface Anal. **36**, 1423-U1429 (2004)
24. Zubair, F., Prentice, B.M., Norris, J.L., Laibinis, P.E., Caprioli, R.M.: Standard Reticle Slide To Objectively Evaluate Spatial Resolution and Instrument Performance in Imaging Mass Spectrometry. Anal. Chem. **88**, 7302-7311 (2016)
25. Hetz, W., Hochholdinger, F., Schwall, M., Feix, G.: Isolation and characterization of rtcs, a maize mutant deficient in the formation of nodal roots. The Plant Journal. **10**, 845-857 (1996)
26. Korte, A.R.Y., Gargey B.Feenstra, Adam D.Lee, Young Jin: Multiplex MALDI-MS Imaging of Plant Metabolites Using a Hybrid MS System. In: He L (ed.). Springer, (2015)
27. Perdian, D.C., Lee, Y.J.: Imaging MS Methodology for More Chemical Information in Less Data Acquisition Time Utilizing a Hybrid Linear Ion Trap-Orbitrap Mass Spectrometer. Anal. Chem. **82**, 9393-9400 (2010)
28. Strupat, K., Kovtoun, V., Bui, H., Viner, R., Stafford, G., Horning, S.: MALDI Produced Ions Inspected with a Linear Ion Trap-Orbitrap Hybrid Mass Analyzer. J. Am. Soc. Mass Spectrom. **20**, 1451-1463 (2009)
29. Hochholdinger, F.: The maize root system: morphology, anatomy, and genetics. Springer, (2009)
30. Jun, J.H., Song, Z., Liu, Z., Nikolau, B.J., Yeung, E.S., Lee, Y.J.: High-Spatial and High-Mass Resolution Imaging of Surface Metabolites of Arabidopsis thaliana by Laser

Desorption-Ionization Mass Spectrometry Using Colloidal Silver. Anal. Chem. **82**, 3255-3265 (2010)

31. Klein, A.T., Yagnik, G.B., Hohenstein, J.D., Ji, Z., Zi, J., Reichert, M.D., et al.: Investigation of the chemical interface in the soybean–aphid and rice–bacteria interactions using MALDI-mass spectrometry imaging. Anal. Chem. **87**, 5294-5301 (2015)
32. Feenstra, A.D., Hansen, R.L., Lee, Y.J.: Multi-matrix, dual polarity, tandem mass spectrometry imaging strategy applied to a germinated maize seed: toward mass spectrometry imaging of an untargeted metabolome. Analyst. **140**, 7293-7304 (2015)
33. Niemeyer, H.M.: Hydroxamic acids (4-hydroxy-1, 4-benzoxazin-3-ones), defence chemicals in the Gramineae. Phytochemistry. **27**, 3349-3358 (1988)
34. Dreisewerd, K., Schürenberg, M., Karas, M., Hillenkamp, F.: Influence of the laser intensity and spot size on the desorption of molecules and ions in matrix-assisted laser desorption/ionization with a uniform beam profile. Int. J. Mass Spectrom. Ion Processes. **141**, 127-148 (1995)
35. Guenther, S., Koestler, M., Schulz, O., Spengler, B.: Laser spot size and laser power dependence of ion formation in high resolution MALDI imaging. Int. J. Mass spectrom. **294**, 7-15 (2010)
36. Qiao, H., Spicer, V., Ens, W.: The effect of laser profile, fluence, and spot size on sensitivity in orthogonal-injection matrix-assisted laser desorption/ionization time-of-flight mass spectrometry. Rapid Commun. Mass Spectrom. **22**, 2779-2790 (2008)
37. Wiegelmann, M., Dreisewerd, K., Soltwisch, J.: Influence of the Laser Spot Size, Focal Beam Profile, and Tissue Type on the Lipid Signals Obtained by MALDI-MS Imaging in Oversampling Mode. J. Am. Soc. Mass Spectrom., 1-13 (2016)

Figures

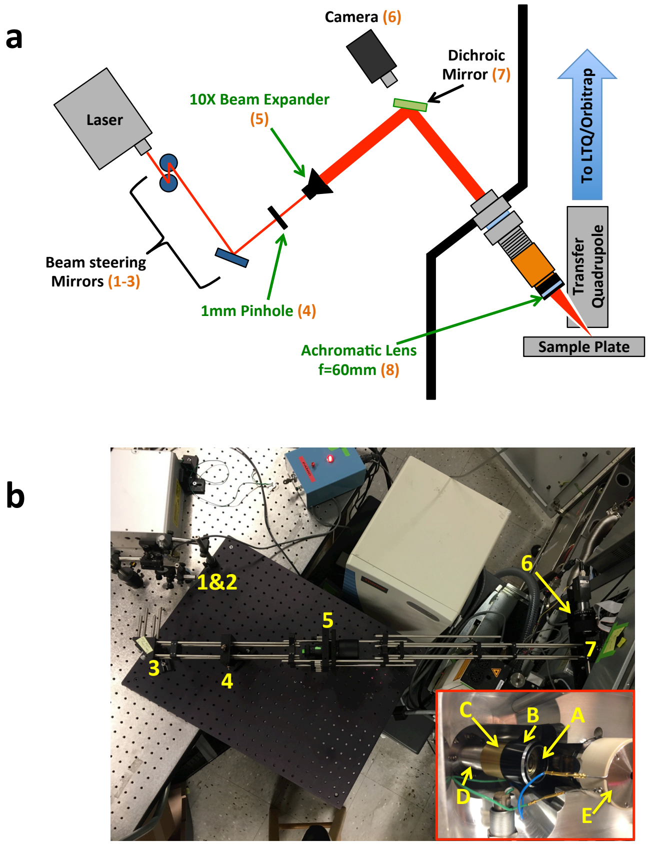

Figure 1. (a) Schematic of laser optic setup for high-resolution MS imaging. The laser is first passed through beam steering mirrors (1-3) before being filtered and expanded (4-5). The laser is then passed into the instrument through the new focusing lens (7-8). **(b)** Photograph of optical components with parts numbered as in 1a. The inset is a photograph of the source interior with modified optics. The focus lens (A) is placed into a compatible lens holder (B). The lens holder is threaded onto a custom-made male-female bronze intermediate (C), which is threaded onto a custom-made male rod attached to the flange (D). The beam passes through these optical components before passing through quadrupole and MALDI extraction plate (E), where it is then incident upon the MALDI sample plate (not shown).

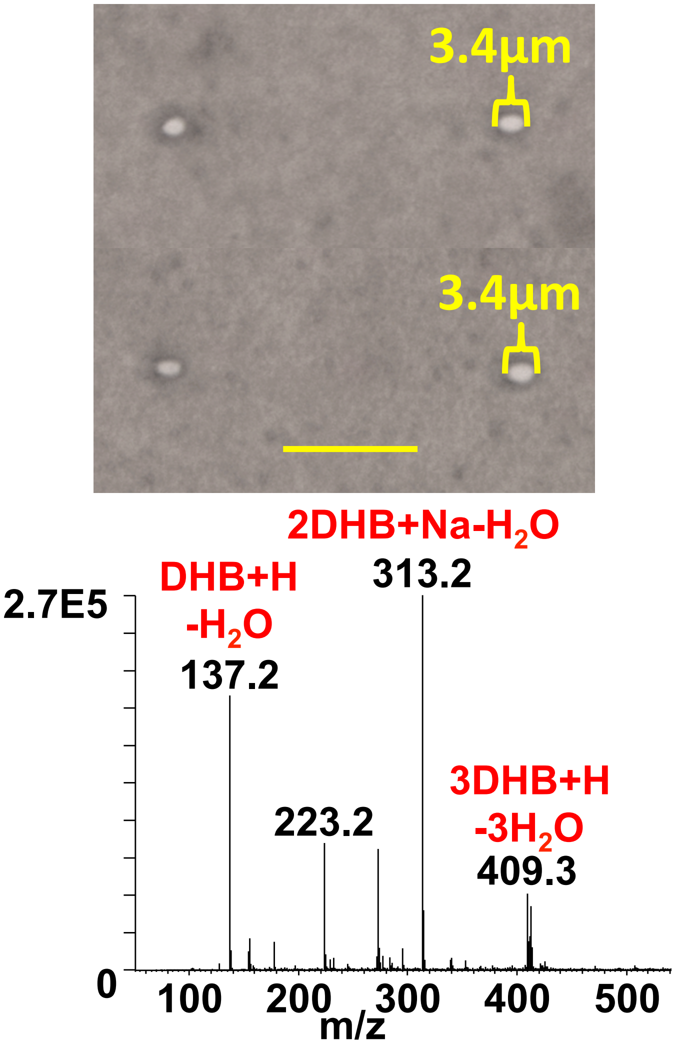

Figure 2. (Top) Microscope images of smallest laser spot size obtained on a thin layer of DHB. Laser spots here were generated using 10 laser shots at an energy of 80%. (Bottom) Ion trap mass spectrum obtained at the same time with the above laser spot size measurement, averaged from 47 spectra. Scale bar: 20 µm.

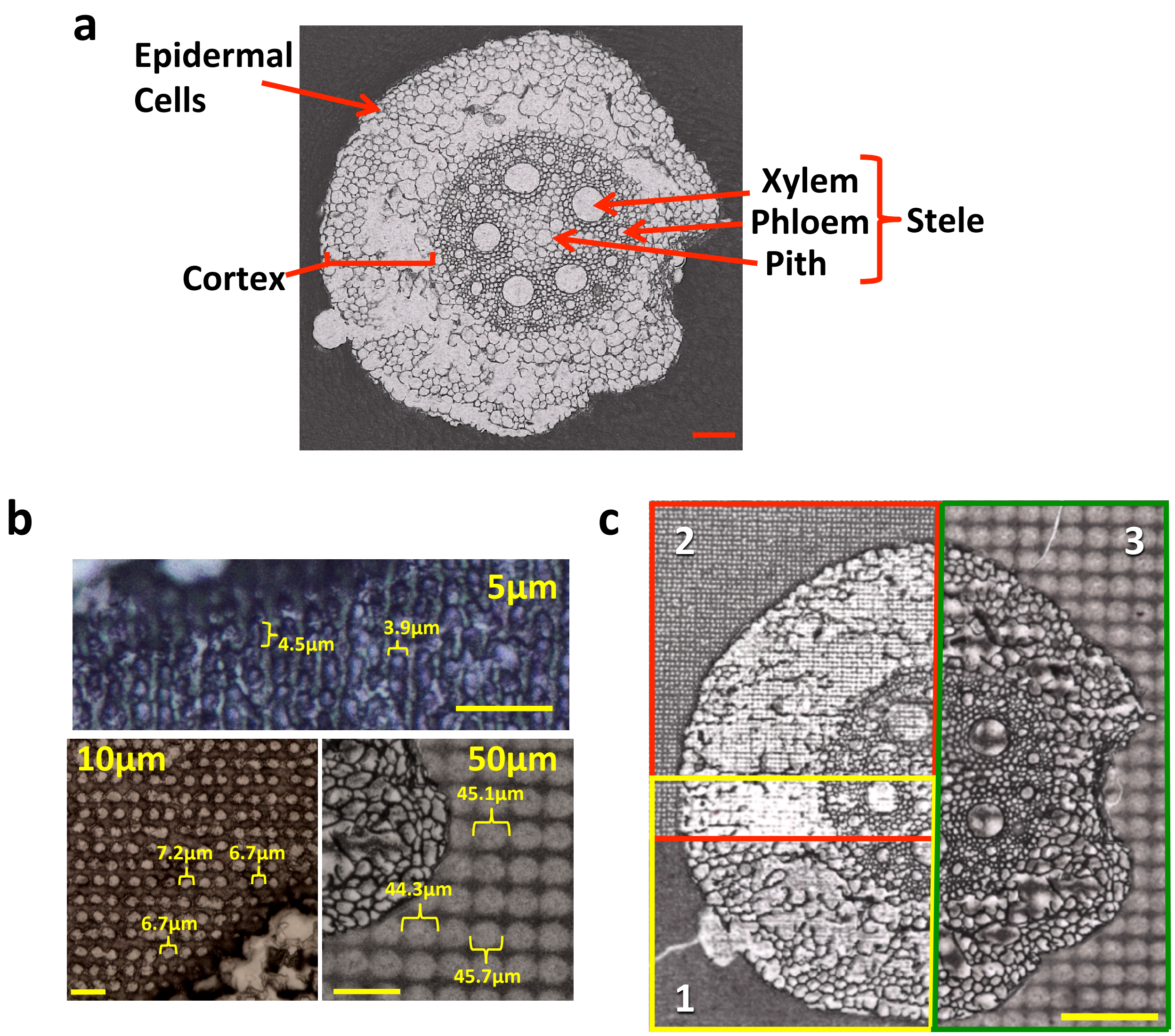

Figure 3. (a) Optical image of maize root cross-section with morphological features labeled. Scale bar: 100 µm. **(b)** Ablation craters in gelatin areas for the 5, 10, and 50 µm imaging runs obtained from the imaging runs. Scale bar: 20 µm for the 5 and 10 µm runs. 100 µm for the 50 µm run. **(c)** Optical image of maize root cross section after all three imaging runs. The 10x beam expander run (yellow) was performed first, followed by the 5x (red) and no beam expander (green) runs. The 5x run slightly overlapped the area covered by the 10x run to ensure complete tissue coverage, but the overlapping area for the 5x run is not used for MS image generation. Scale bar: 200 µm.

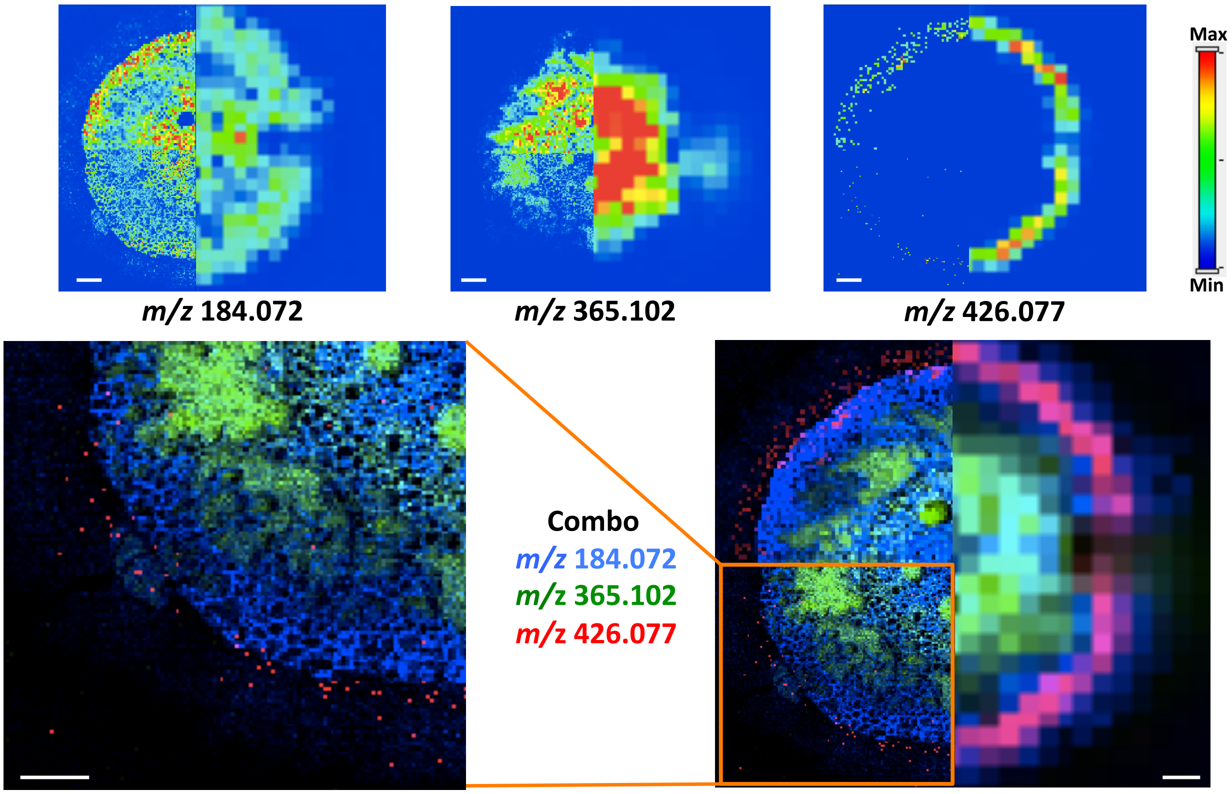

Figure 4. (Top) MS images for three selected ions of interest from maize root combined from each of the 5, 10, and 50 µm resolution imaging runs. **(Bottom)** Combination images of three MS images with different false colors. The 5 µm resolution image is enlarged to show the fine localization information. The max values used in generating the 5 and 10 µm resolution images are 1×10^6, 5×10^5, and 6×10^4 for m/z 184.072, 365.102, and 426.077, respectively, whereas ten times higher max values are used for 50 µm resolution images. The scale bar is 100 µm.

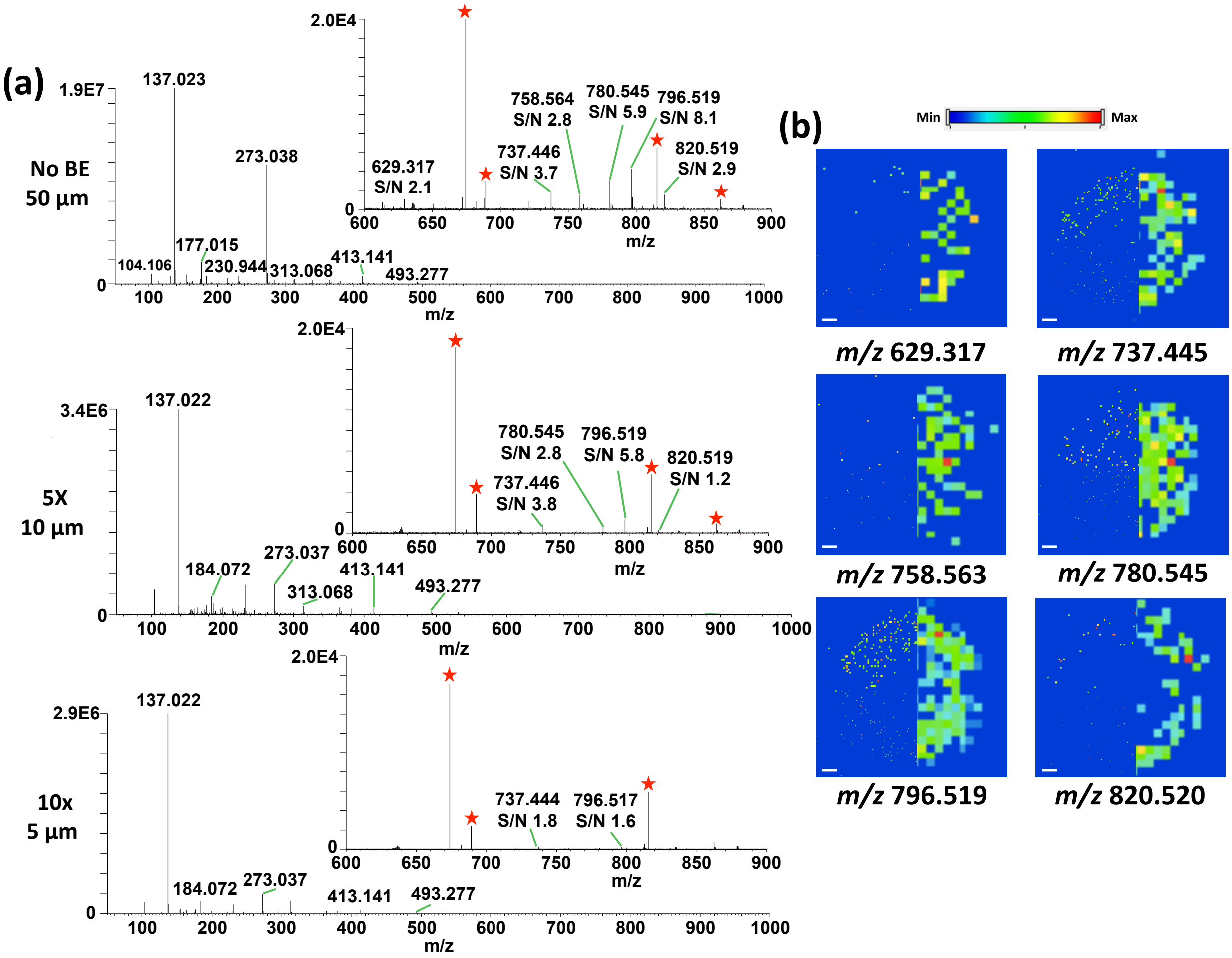

Figure 5. (a) The mass spectra obtained by 50 µm (top), 10 µm (middle), and 5 µm (bottom) resolution setup averaged over the 1/4 of the maize root region. The mass range for *m/z* 600-900 is expanded as shown as inset spectra. Red stars denote background peaks. All real peaks with S/N values higher than 1 are labeled in the inset spectra. **(b)** MS images for the six ions labeled in the inset spectra of 5a. The scale bar is 100 µm.

Supplemental Figures

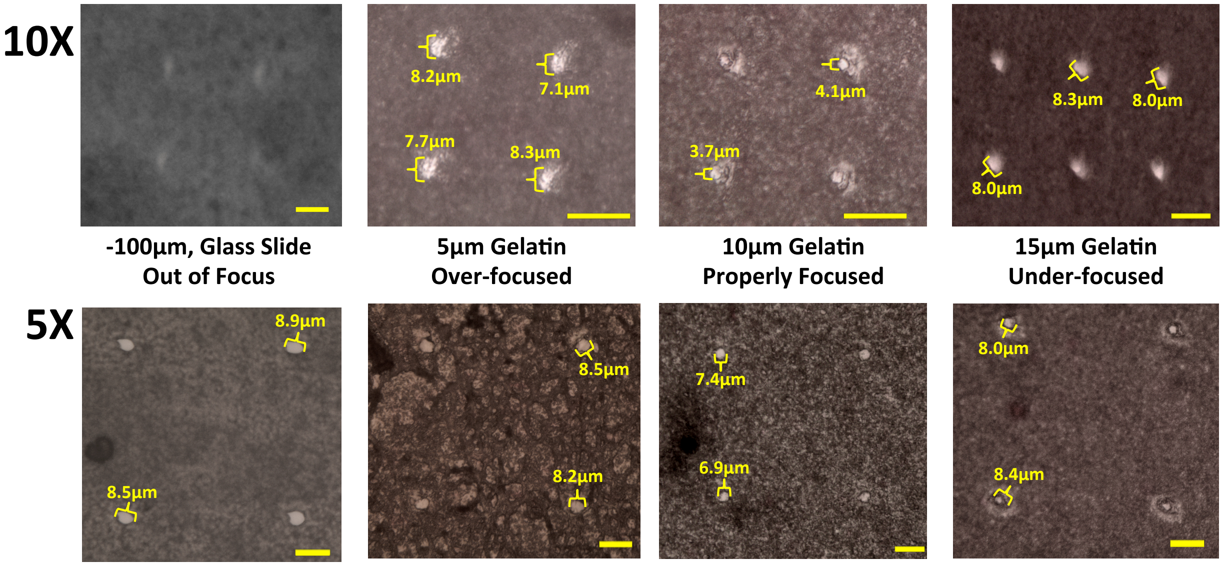

Supplemental Figure S1. The effect of sample thickness on spot size. **Top**: When using the 10x beam expander, changing the sample thickness by 5 µm alters the spot size from ~4 µm to ~8 µm, and the spots are barely observed on DHB directly deposited on a glass slide. All spots are made with 84% laser power and 10 shots. **Bottom:** For the 5x beam expander, the spot size varies minimally from ~7 µm to ~8 µm when altering the sample thickness by 5 µm, and is on the order of ~9 µm on glass only. All spots were made with 86% laser power and 10 shots. Scale bar: 20 µm for all.

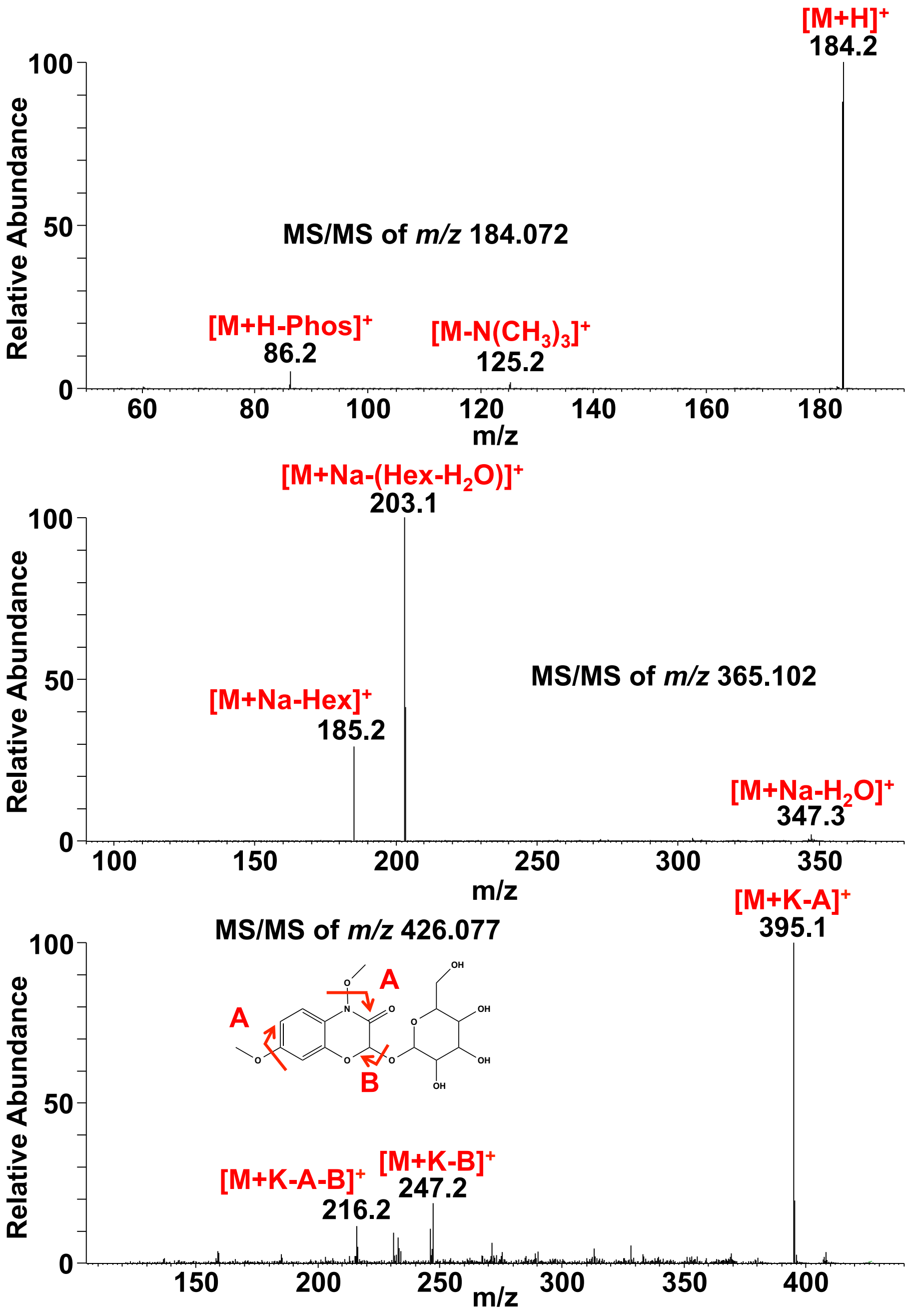

Supplemental Figure S2. MS/MS for the three ions imaged in Figure 5. The ions are identified as phosphocholine, a disaccharide, and HDMBOA-Glc, respectively, from top to bottom. The mass range from *m/z* 120-380 is amplified 10x in the bottom MS/MS spectrum.

CHAPTER 6

SUMMARY AND FUTURE DIRECTIONS

Summary

This thesis presents developments of technologies for MALDI-MSI that will allow for studies on metabolic biology, as well as a biological application of MALDI-MSI. MALDI-MSI was used in combination with traditional GC and LC analysis to track metabolite localizations between two inbreds of maize during germination and revealed unique localization patterns for various classes of molecules. A previously developed multiplex instrumental method was expanded upon by analyzing serial tissue sections with multiple matrices in both ion modes along with MS/MS filtering, demonstrating that metabolomic-scale MALDI-MSI with confident identification of metabolites from tissue is possible. A binary matrix of DHB and Fe_3O_4 nanoparticles was shown to help alleviate the issue of TG suppression by PC, while also increasing the number of medium-sized metabolites seen and high-quality MS/MS obtained from a single experiment. Lastly, laser optics modifications were made to allow for 5 μm imaging of maize root without oversampling as part of a multi-resolution optics system, representing an improvement from our group's previous optics setup which was only able to achieve ~9 μm spatial resolution.

Future Directions

In recent years, MSI has seen rapid growth in popularity as its full potential is beginning to be realized. Studies are ongoing investigating advancements such as new sampling/ionization methods,[1] multimodal imaging approaches,[2, 3] and new software packages for data analysis,[4] along with other improvements to continue to develop this field into its full maturation.[5] This progress along with the work presented in this thesis should continue to render MSI an effective technology for biological analyses, especially in plants.

The work here represents a good foundation upon which future experiments and improvements can be based. Work like that in Chapter 2 demonstrates that MALDI-MSI can be used to track metabolite flux and localization over time. This offers up a wide range of applications, as tracking of metabolites allows for the understanding and localization of metabolic processes that utilize these metabolites. Tracking of metabolite localization over time can also allow for the elucidation of cell and physiological structure function in different organisms throughout various processes.

More improvements can be made to the work performed in Chapter 3, which would allow for collection of more high-quality MS/MS and remove many of the uninformative spectra. For example, when performing a data-dependent multiplex-MSI experiment, multiple parameters can be adjusted for the data-dependent selection of ions to fragment, such as exclusion time, exclusion duration, number of ions on the exclusion list, collision energy, and more. Modifying and optimizing these parameters will allow for structural MS/MS analysis of more ions, thereby increasing the overall information gained from a sample. Additionally, the generation of an MS/MS database specific to our instrument would allow for easier, faster, more confident metabolite identification. Current group work is also investigating the possibility of employing multiplex imaging to acquire MS/MS from the same spatial location as the HRMS scan, thereby reducing the spatial resolution loss caused by using multiple spiral steps. These works will allow for more information from a single experiment, potentially at high spatial resolution.

Chapter 4 demonstrates the advantages of combining multiple matrices together, and that organic matrices can be combined with nanoparticle matrices. As such, more combinations can be generated to fulfill specific needs and ionize various compound classes in less data acquisition time. Additionally, this work shows that combinations can be used to overcome inherent limitations of samples, such as ion suppression, to allow for more complete metabolite visualization and detection in a single analysis.

High-resolution MALDI-MSI allows for extremely detailed information about metabolite distributions, and allows for the in-depth understanding of metabolic processes, potentially down to the cellular level. While the ultimate achievable laser spot size shown in Chapter 5 is significantly limited due to depth of focus issues, plenty of advancements can still be made to make the system more robust and reproducible. Additional work on motorizing the final lens position, optimizing sample preparation conditions to eliminate the use of the adhesive pink tape, as well as adjusting the sample thickness to compensate for depth of focus issues should allow for high-resolution MALDI-MSI to be more reproducibly applicable to biological studies.

This work aimed to develop, improve, and apply MALDI-MSI technologies for the biological analysis of plants. The work contained herein shows that while MALDI-MSI is a wide-ranging and versatile technique, there are plenty of limitations to be overcome and improvements that are yet to be made. Regardless, the technological advancements herein lay a solid foundation for the continuing applications of MALDI-MSI to the study of biological samples that will prove effective for future analysis.

References

1. J. Soltwisch, H. Kettling, S. Vens-Cappell, M. Wiegelmann, J. Müthing and K. Dreisewerd, *Science*, 2015, **348**, 211-215.
2. S. Chughtai, K. Chughtai, B. Cillero-Pastor, A. Kiss, P. Agrawal, L. MacAleese and R. M. Heeren, *International Journal of Mass Spectrometry*, 2012, **325**, 150-160.
3. V. W. Petit, M. Réfrégiers, C. Guettier, F. d. r. Jamme, K. Sebanayakam, A. Brunelle, O. Laprévote, P. Dumas and F. o. Le Naour, *Analytical chemistry*, 2010, **82**, 3963-3968.
4. G. Robichaud, K. P. Garrard, J. A. Barry and D. C. Muddiman, *Journal of the American Society for Mass Spectrometry*, 2013, **24**, 718-721.
5. J. H. Jungmann and R. M. Heeren, *Journal of proteomics*, 2012, **75**, 5077-5092.